The role of high-latitude oceans in transient climate change

by

Yavor Kostov

B.A., Pomona College (2010)

Submitted to the Department of Earth, Atmospheric, and Planetary Sciences
in partial fulfillment of the requirements for the degree of

Doctor of Philosophy in Climate Physics and Chemistry

at the

MASSACHUSETTS INSTITUTE OF TECHNOLOGY

June 2016

MASSACHUSETTS INSTITUTE OF TECHNOLOGY
JUN 13 2016
LIBRARIES
ARCHIVES

© Massachusetts Institute of Technology 2016. All rights reserved.

Author ... Signature redacted ....
Department of Earth, Atmospheric, and Planetary Sciences
April 6, 2016

Certified by........... Signature redacted ....
John Marshall
Cecil and Ida Green Professor of Oceanography
Thesis Supervisor

Accepted by.... Signature redacted ....
Robert van der Hilst
Schlumberger Professor of Earth Sciences, Department Head

The role of high-latitude oceans in transient climate change

by

Yavor Kostov

Submitted to the Department of Earth, Atmospheric, and Planetary Sciences
on April 5, 2016, in partial fulfillment of the
requirements for the degree of
Doctor of Philosophy in Climate Physics and Chemistry

Abstract

In this thesis we explore the role of the large-scale ocean circulation in the North Atlantic and the Southern Ocean (SO) in setting the regional and globally averaged sea surface temperature (SST) response to atmospheric forcing. We focus on the impact of anthropogenic greenhouse gases (AGHGs) and the Antarctic ozone hole and use output from general circulation models (GCMs) to estimate the corresponding climate response functions (CRFs). We show that the strength and the vertical extent of the time-mean Atlantic Meridional Overturning Circulation (AMOC) set the effective heat capacity of the World Ocean and affect the global CRF to greenhouse gas (GHG) forcing. A large fraction of the anomalous surface heat uptake induced by GHGs takes place over the North Atlantic.

However, the SO also plays a significant role in removing excess heat from the atmosphere. Compared to the rest of the World Ocean, the SO warms at a much slower rate under GHG forcing. In this region the background Meridional Overturning Circulation (MOC) upwells unmodified deep water masses to the surface where they take up atmospheric heat. The modified water masses are then advected northward and subducted in the mid-latitudes. This geographical imprint of the MOC is reflected in the regional CRFs to GHGs, as seen in idealized numerical experiments with GCMs.

However, GHGs are not the only major source of anthropogenic forcing on the SO. Stratospheric ozone depletion around Antarctica gives rise to an atmospheric pattern similar to the positive phase of the Southern Annular Mode (SAM): a strengthening and a southward shift of the westerlies. This poleward intensification of the winds changes the ocean circulation and gives rise to an SST response. We examine the SO CRF to a SAM pattern that arises either in the form of natural variability in unforced control experiments or as a result of imposed ozone perturbations. We analyze the SO SST response to SAM on multiple timescales and across an ensemble of GCMs from the Climate Modeling Intercomparison Project phase 5 (CMIP5). We show that the corresponding SO CRF is governed by the anomalous wind-driven MOC redistributing the background heat reservoir. The intermodel diversity in the fast and slow SST responses to SAM is partly explained by differences in the climatological thermal stratification across the ensemble of GCMs. Furthermore, we demonstrate that the sea ice response to SAM in models is very well correlated with the geographic pattern of the SST anomalies.

Finally, we convolve our estimated CRFs with timeseries of historical forcing to recover the SO SST trends in numerical simulations and in observations. We contrast the multidecadal SO cooling trends against the SST warming rate in the Northern Hemisphere high latitudes. Our results imply that the recent cooling in the SO may be explained by the Antarctic ozone hole projecting on a positive SAM trend. We furthermore attempt to understand why CMIP5 models have been unable to reproduce the observed negative SST trends in the SO and instead predict regional warming. Many GCM simulations underestimate the historical SAM evolution. Another subset of CMIP5 models have biases in their climatological SO stratification, which affects their SO CRFs to SAM.

The successful application of the CRF framework in the context of observed and simulated SST trends validates the results of our analysis. We are thus able to interpret the CRFs as inherent characteristics of the climate system and elucidate the importance of the high latitude oceans in transient climate change.

Thesis Supervisor: John Marshall
Title: Cecil and Ida Green Professor of Oceanography

Acknowledgments

Reflecting on almost six years at MIT, I appreciate the guidance and mentorship that my adviser John Marshall has provided me. John has given me both motivation and opportunity to pursue my research interests. It has been a pleasure working in his group.

I would also like to thank Kyle Armour, Ute Hausmann, and David Ferreira for their role as mentors and collaborators. I am very grateful that I have had the chance to work on a joint FESD Ozone and Climate project with Susan Solomon, Marika Holland, and Laura Landrum. Their experienced advice and feedback has influenced my research very positively.

I have further benefited from my interactions with all current and former members and affiliates of the John Marshall group: David Ferreira, Kyle Armour, Ute Hausmann, Jeff Scott, Jean-Michel Campin, Chris Hill, Ryan Abernathey, Brian Rose, Ross Tulloch, Rebecca Jackson, Michael Bates, Aaron Donohoe, and Hajoon Song.

I extend my sincere gratitude to the thesis committee members Susan Solomon, David McGee, Paul O'Gorman, and John Marshall. They have provided me with constructive feedback and have helped me improve the quality of my dissertation,

The administrators of our computational clusters Jean-Michel Campin, Jeff Scott, and Greg have assisted me with various technical issues. I would like to thank Jean-Michel Campin and David Ferreira for giving me files of code that served as useful examples for my computations and for helping me debug my scripts.

I thank Roberta Allard, Vicki McKenna, Jen Sell, Jen Fentress, Beth MacEachran, Allison Provaire, Christine Maglio, and Darius Collazo for helping me deal with the administrative and accounting procedures. It was always great to see the friendly smiles of Helen Hill, Melissa Fox, and Karen Fosher.

The program in Climate Physics and Chemistry places a top priority on education, and I have always appreciated the opportunity to attend well-taught and interesting lectures. I extend my deep gratitude to my teaching instructors, Ed Boyle, Kerry Emanuel, Carl Wunsch, Claudia Cenedese, Larry Pratt, Lodovica Illari, Ruben Ros-

ales, Alan Plumb, John Marshall, Ron Prinn, Glenn Flierl, and Mike Spall. I would also like to thank my teaching assistants Nick Woods, Daniela Domeisen, Diane Ivy, and Morgan O'Neill, who helped me a lot with my coursework, but also provided me with important guidance when I first entered the field of climate physics. My study buddies Mariana Rodriguez, Xan Miltenberger, Andy Miller, and Veronique Dansereau made working on course assignments so much fun! I enjoyed every moment doing lab work with Dan Amrhein and Deepak Cherian.

My office mates throughout the years: Aditi Sheshadri, Sophia Merrifield, Elise Olson, Brian Green, Emily Zakem, Keisuke Inomura, Deepa Rao, Mukund Gupta, and Margaret Duffy have also helped me enjoy my time at EAPS! I cannot imagine my six years here without all my friends around the department, both in the Green Building and in the E25 labs! I would not do justice to them if I attempted to list all names individually.

My time at MIT would not have been the same without the friendly and supportive community at my graduate residence building, the Warehouse. I am particularly grateful to our Housemasters John Ochsendorf and Anne Carney, as well as their smart children, William and Lucia. I would also like to thank all other Warehouse officers and Advisory Board members, who have worked side by side with me. I am very grateful that I have had a chance to meet so many friendly neighbors throughout the years in the dorm.

I also wish to thank many people outside of my department and my campus residence hall, friends at MIT and beyond. The Bulgarian community in Boston has given me the chance to remain close to my roots and feel at home. Many people have offered their support at different times and have helped me keep a work-life balance: my friends who have lived in the Boston area or visited the city, my undergraduate classmates from Pomona College who have stayed in touch with me, my peers at Harvard's EPS Department, my old high school friends.

I should acknowledge that even before coming to MIT, faculty at ACS (the American high school in Sofia, Bulgaria) and at Pomona College instilled an early interest in the exact and natural sciences. This eventually motivated me to pursue a Ph.D.

in Climate Physics.

Last, but not least, I express my deepest gratitude to my mother, my father, my aunt, and all family members who have supported me continuously throughout my education. Their interest in my work has given me strength and courage. Without my family I would not be able to make it as far!

I would like to gratefully acknowledge the financial support from the NASA MAP program and the NSF FESD Ozone and Climate project.

Chapter 2 is joint research with Kyle Armour and John Marshall. This work has been peer reviewed by Isaac Held, GRL editor Noah Diffenbaugh, and an anonymous reviewer. Chapters 3 and 4 are joint work with John Marshall, Ute Hausmann, Kyle Armour, David Ferreira, and Marika Holland with helpful feedback from Susan Solomon, Paul O'Gorman, David McGee, Jan Zika, Climate Dynamics editor Jean-Claude Duplessy, and an anonymous reviewer.

Contents

1 Introduction **25**

1.1 The role of high latitude oceans for the climate response to greenhouse gas forcing . . . 25

1.2 Response of the Southern Ocean to the Southern Annular Mode . . . 27

2 Impact of the Atlantic Meridional Overturning Circulation on Ocean Heat Storage and Transient Climate Change **31**

2.1 AMOC and ocean heat storage . . . 34

2.2 Ocean heat storage and SST response . . . 37

2.2.1 Representing ocean heat storage in a simple energy balance model 37

2.2.2 Calibrating the Two-Layer EBM to Results from CMIP5 AOGCMs 44

2.2.3 Results with Alternative Definitions of the Temperature and AMOC Metrics. . . . 51

2.3 Time Evolution of the AMOC: Weakening and Shoaling of the Circulation in the Abrupt 4×CO_2 Experiment . . . 53

2.4 Discussion and Interpretation of the Results. . . . 55

3 Fast and slow responses of Southern Ocean sea surface temperature to SAM in coupled climate models **57**

3.1 Data and methods . . . 58

3.2 Verification of the Methodology . . . 63

3.3 Results . . . 63

3.4 Connecting Our Model-Based Results to the Real Southern Ocean . . 69

3.5 Discussion and Interpretation of the Results 70

4 Southern Ocean cooling and sea ice expansion in a warming world 77

4.1 The Southern Ocean response to multidecadal SAM trends 78

4.2 Regional CRFs to greenhouse gas forcing 82

4.3 Understanding the Southern Ocean SST trends in CMIP5 historical simulations 83

4.4 Interpreting the observed Southern Ocean SST trends using SAM and GHG CRFs 87

4.5 Interpreting the observed Southern Ocean SST trends using ozone and GHG CRFs 89

5 Conclusion 107

5.1 Summary 107

5.2 Unresolved Questions and Outlook 111

List of Figures

1-1 Shown in black is the 1982-2014 timeseries of SST [°C] averaged between 55°S and 70°S based on the NOAA Reynolds Optimum Interpolation (*Reynolds et al.*, 2002). The 1980-2014 timeseries of the annual-mean SAM index based on the ERA Interim reanalysis (*Dee et al.*, 2011) is superimposed in gray. The index is defined as the first principal component of SLP variability south of 20°S and is normalized by its standard deviation. Solid lines indicate linear trends fitted to each timeseries. Note the reversed scale for the SAM timeseries shown on the right. 28

2-1 a) Area-averaged SST anomaly in CMIP5 4×CO_2; b) Vertical distribution of the ocean heat anomaly in CMIP5 models, averaged over the World Ocean, 100 years after the CO_2 quadrupling; c) SST response under model-specific feedback and forcing (λ_o, $\mathcal{F}_o$), but ensemble-mean ocean properties (q, h_2, ε), as simulated by the 2-layer ocean EBM (see Section 2.2); d) SST response under model-specific ocean properties (q, h_2, ε) but ensemble-mean feedback and forcing (λ_o, $\mathcal{F}_o$), as simulated by the 2-layer ocean EBM (see Section 2.2). The eight CMIP5 models included here are those for which sufficient output was accessible at the time of our analysis (ocean temperature, sea-surface heat flux and AMOC data). 33

2-2 Zonal mean potential temperature anomaly in the World Ocean; 30-year average centered 100 years after 4×CO_2. The magenta dash-dotted line marks the average depth above which 80% of the heat anomaly is contained. Overlaid contours mark the upper overturning cell of the AMOC [Sv] between 35S and the Arctic Circle (temporal average over the 150 year 4×CO_2 simulation; contour lines are 5 Sv apart, with an outermost contour at 0 Sv.) The green dashed line denotes the uniform metric for the downward extent, D_{AMOC}, of the upper overturning cell. CMIP5 models: a) ACCESS1-0; b) CCSM4; c) CNRM-CM5; d) GFDL-ESM2M; e) GFDL-CM3; f) MPI-ESM-LR; g) MRI-CGCM3; h) NorESM1-M. 36

2-3 a) Correlation between $D_{80\%}$ and D_{AMOC} (R=0.93, p-value p<0.01); b) Correlation between D_{AMOC} and M_{AMOC} (R=0.92, p-value p<0.01). 37

2-4 a) CMIP5 4×CO_2 ensemble mean of: a) Net heat flux anomaly at the ocean surface (30-year average centered on year 100); b) Potential temperature anomaly at depth 1,000 m (30-year average centered on year 15); b) Potential temperature anomaly at depth 1,000 m (30-year average centered on year 100). 38

2-5 Linear relationship between the SST anomaly, T_1, and the temperature anomaly of near-surface air above land, $T_{LandAir}$, in the abrupt quadrupling experiment. Comparison across CMIP5 models: a) ACCESS1-0; b) CCSM4; c) CNRM-CM5; d) GFDL-ESM2M; e) GFDL-CM3; f) MPI-ESM-LR; g) MRI-CGCM3; h) NorESM1-M. 42

2-6 Comparison between the annual average global SST response in the original CMIP5 abrupt 4×CO_2 simulations and the SST responses reproduced by the calibrated 2-layer model. 46

2-7 Correlations among GCM variables and calibrated EBM parameters with correlation coefficients R and p-values p: a) $D_{80\%}$ and H, (R=0.79, p<0.03); b) H and D_{AMOC} (R=0.87, p<0.01); c) q and M_{AMOC} (R=0.84, p<0.01); d) H and q (R=0.89, p<0.01); e) T_{eq} and λ_o (R=-0.94, p<0.01); f) ε and q (R=0.81, p<0.01). 48

2-8 Evolution of the annual average AMOC maximum in the abrupt 4×CO_2 runs of CMIP5 GCMs. 53

3-1 Timeseries from the control simulation of model CCSM4: the SAM index in gray and the Southern Ocean (SO) SST anomaly averaged between 55°S to 70°S in black. Each index is detrended and rescaled by its standard deviation. The SST scale is shown on the left vertical axis, and the reversed scale for the SAM index is shown on the right. The SO SST is negatively correlated to the SAM index with $R = -0.37$ at a lag of 1 year. 60

3-2 Application of the regression algorithm to systems with a known prescribed step response function. On the top row we show a test case where we assume long memory in our SAM and SST signals. The SST signal is diluted such that 60% of the variance is noise. In panel a) on the left, we show the lagged autocorrelations of SAM and SST in CCSM4 (gray dashed curves) and our synthetic artificially generated signals (solid black curves). In panel b) we show applications of the regression algorithm. The thick black curve is the true prescribed step response function. The thin gray curves and the vertical bars denote the estimated step response function $SST_{Step}(t)$ and the uncertainties $\sigma_{SSTstep}(t)$ produced by applying our regression algorithm. The two gray curves in panel b) result from analyzing separate realizations in which we use the same prescribed step response and AR timeseries with the same statistical properties (illustrated in a)) but different random values. On the bottom row we show a test case where we assume shorter memory in the SAM and SST signals, but the SST signal is diluted with more noise, such that the forced response contributes only 20% of the total variance. Panels c) and d) are analogous to panels a) and b). 64

3-3 Annual-mean response of the Southern Ocean SST anomaly [°C] to: a) a positive impulse perturbation in the SAM index of magnitude equal to $\overline{\sigma_{SAM}}^{Ens}$; b) a positive step increase in the SAM index of magnitude equal to $\overline{\sigma_{SAM}}^{Ens}$. Different colors are used to distinguish the response functions in the three CMIP5 models shown: CCSM4, MPI-ESM-MR, and CNRM-CM5. For each model we show 100 fits that outline an envelope of uncertainty. Vertical error bars denote the margin of error for each fit. 65

3-4 Annual-mean responses of the Southern Ocean SST [°C] to a step increase in the SAM index of magnitude $\overline{\sigma_{SAM}}^{Ens}$ – comparison across the CMIP5 ensemble. For each model we have shown only the mean estimate $SST_{Step}(t)$. 66

3-5 a) Relationship between the models' climatological meridional SST gradients $\partial_y\overline{[SST]}$ [°C / 100 km] in the Southern Ocean (55°-70°S) and the Year 1 SST response $SST_{Step}(t = 1)$ [°C] to a step perturbation in the SAM index. The vertical error bars correspond to $\sigma_{SSTstep}(t = 1)$. b) Relationship between the climatological temperature inversion $\Delta_z\overline{[\theta]}$ [°C] in the Southern Ocean (depth levels 65 m to 550 m) and the SST warming rate Λ [°C / year] which characterizes the slow response to a step increase in the SAM index. Legend: both a) and b) use the same color code and alphabetical order as in Figure 3-4 to distinguish the CMIP5 models analyzed. Straight lines indicate linear fits to the scatter where each data point in the regression analysis is weighted by the inverse of the SE squared. The yellow stars denote estimates for the response of the real Southern Ocean based on observed climatological meridional SST gradients between 55°S and 70°S (NOAA Reynolds Optimum Interpolation *Reynolds et al.* (2002)) and the climatological $\Delta_z\overline{[\theta]}$ inversion (Hadley Centre EN4 dataset, *Good et al.* (2013)). . . . 74

3-6 a) Scatter: estimated fast responses [°C] after correcting for the model bias in the climatological meridional SST gradients relative to observations (same color code as in Figure 3-5). Vertical error bars denote 2 SE. The horizontal black line is the weighted mean of the model estimates. The solid (dashed) gray lines denote one (two) weighted standard deviations (SD) of the spread. b) Same as in a) but for the slow response rates [°C/year] after correcting for the bias in $\Delta_z\overline{[\theta]}$. c) Solid black lines: a schematic for the estimated response of the real SO SST [°C] based on a) and b). We show the ensemble mean bias-corrected fast response ± 1 SD. This is extended until Year 7 with lines matching the ensemble mean bias-corrected slow response ± 1 SD. Dashed lines show a linear extrapolation at a constant rate or a constant temperature. Gray lines replicate the Fig. 3-4 SO SST step responses [°C]. 75

4-1 a) Observed SST trends [°C/decade] for the 1982-2014 period based on the NOAA Reynolds Optimum Interpolation Dataset [Reynolds et al., 2002], which begins in 1982; b) Numerical simulations of the SST trends [°C/decade] for the 1979-2014 period: an ensemble mean of CMIP5 historical experiments extended under the rcp8.5 scenario; c) Same as a) but for 1982-2014 trends in sea ice concentration [%/decade] from Reynolds et al. [2002]; d) Same as b) but showing sea ice trends [%/decade]; e) Observed trends in the sea surface salinity (SSS) [psu/decade] for the 1979-2013 period based on the HadEN4 Dataset [Good et al., 2013]; f) Same as b) and d) but showing sea surface salinity (SSS) trends [psu/decade]. 93

4-2 Example timeseries and trends in the westerly winds and SAM indices from the control run of model ACCESS1-0: a) Timeseries for the Southern Hemisphere maximum of the annually averaged zonal mean zonal wind near the surface [m/s]. The red lines show examples of thirty-year linear trends in the wind speed over two different periods. For comparison, the inset green line shows the slope of the last historical thirty-year trend from the ERA Interim reanalysis; b) Comparison of the thirty-year trends in the wind index from [a)] (timeseries II) and two SAM indices: index I is defined as the first principal component of sea level pressure south of 20°S, and index III is defined as the contrast in sea level pressure between 45°S and 60°S. Each index is normalized by its standard deviation; c) Timeseries for the annually averaged SST anomaly between 55° and 70°S. The red lines show the linear trends in SST over the same thirty-year periods as the ones highlighted with red lines in panel a) above; d) Distribution of all thirty-year westerly wind trends [m/s/year] based on the timeseries shown in [a)]. 94

4-3 Composited 30-year trends in zonally-averaged zonal wind at the surface [m/s/decade] from periods of 2σ SAM trends in the CMIP5 control runs. The result for each ensemble member is rescaled by a ratio between the amplitude of the zonally averaged 1980-2010 westerly wind trend from ERA-Interim and the amplitude of the westerly wind trend in each CMIP5 model composite. 95

4-4 Ensemble mean of 23 models. The results for each ensemble member are rescaled by a ratio between the amplitude of the zonally averaged 1980-2010 westerly wind trend from ERA-Interim and the amplitude of the westerly wind trend in each CMIP5 model composite. a) Composited 30-year SST trends [°C/decade] from periods of 2σ SAM trends in the CMIP5 control runs; b) Same as in a) but for sea ice concentration trends [%/decade]; c) Same as in a) and b) but for surface salinity trends [psu/decade]. 96

4-5 Composited 30-year SST trends [°C/decade] from periods of 2σ SAM trends in the CMIP5 control runs of models: a) ACCESS1-0; b) ACCESS1-3; c) BCC-CSM1; d) CanESM2; e) CCSM4; f) CESM-CAM5; g) CMCC-CM; h) CNRM-CM5; i) GFDL CM3; j) GFDL-ESM2G; k) GFDL-ESM2M; l) GISS-E2-H; m) GISS-E2-R; n) IPSL-CM5A-LR; o) IPSL-CM5A-MR; p) IPSL-CM5B-LR; q) MIROC5; r) MIROC-ESM; s) MPI-ESM-LR; t) MPI-ESM-MR; u) MRI-CGCM3; v) NorESM1-M; w) NorESM1-ME. The result for each ensemble member is rescaled by a ratio between the amplitude of the zonally averaged 1980-2010 westerly wind trend from ERA-Interim and the amplitude of the westerly wind trend in each CMIP5 model composite. We have shown only trends that are significant at the 95% confidence level. 97

4-6 Composited 30-year trends in sea ice concentration [%/decade] from periods of 2σ SAM trends in the CMIP5 control runs of models: a) ACCESS1-0; b) ACCESS1-3; c) BCC-CSM1; d) CanESM2; e) CCSM4; f) CESM-CAM5; g) CMCC-CM; h) CNRM-CM5; i) GFDL CM3; j) GFDL-ESM2G; k) GFDL-ESM2M; l) GISS-E2-H; m) GISS-E2-R; n) IPSL-CM5A-LR; o) IPSL-CM5A-MR; p) IPSL-CM5B-LR; q) MIROC5; r) MIROC-ESM; s) MPI-ESM-LR; t) MPI-ESM-MR; u) MRI-CGCM3; v) NorESM1-M; w) NorESM1-ME. The result for each ensemble member is rescaled by a ratio between the amplitude of the zonally averaged 1980-2010 westerly wind trend from ERA-Interim and the amplitude of the westerly wind trend in each CMIP5 model composite. We have shown only trends that are significant at the 95% confidence level. For each model we have listed the correlation between the composited sea ice trends and the composited SST trends from Figure 4-5. 98

4-7 a) Ensemble-mean composites from periods of 2σ SAM trends in the CMIP5 control runs. Bottom panel: Composited 30-year trends in zonally-averaged ocean potential temperature at depth [°C/decade] from periods of 2σ SAM trends in the CMIP5 control runs. Ensemble mean of 23 models. The result for each ensemble member is rescaled by a ratio between the composited trends and the reanalyzed ERA-Interim trends in the zonally averaged surface westerlies. Green contours spaced 0.5°C apart indicate zonally averaged time-mean potential temperature in the ensemble mean. Schematic arrows and dashed lines mark the latitude ranges where we expect anomalous horizontal and vertical Ekman transport according to the sign of the wind trends and wind curl trends shown in red and blue in the top panel; b) Observed 30-year trends in zonally averaged ocean potential temperature [°C/decade] for the 1979-2013 period based on the HadEN4 Dataset [Good et al., 2013]. 99

4-8 Composited SST trends 55-70°S from Figure 5, compared with the SST trends predicted using response functions from Kostov et al. (2015). We have convolved the step response functions with the observed wind trend and then fitted 30-year linear trends using least square's regression and weighing by the inverse of the standard error squared. 100

4-9 Regional CRFs [°C] to abrupt CO_2 quadrupling from Marshall et al. [2014]. Red curves show the SST response in the Northern Hemisphere north of 50°N, and the green curves show the response in the Southern Ocean south of 50°S. The thick line indicates the ensemble mean of CMIP5 models, and the shaded envelopes mark one standard deviation of the ensemble spread. Layout to be modified. 100

4-10 A sample of SST response functions [°C] for the Southern Ocean south of 55°S in 4 CMIP5 models forced with abrupt CO_2 quadrupling. . . 101

4-11 SO SST response functions [°C] based on the analysis in Chapter 3 but rescaled to represent the response to a 1 mbar step increase in the SLP_{index} SAM index. Different colors denote CMIP5 models. 101

4-12 Comparison of the simulated 1979-2014 SO SST trends [°C/decade] in CMIP5 and our reconstructions using a) convolutions of the SAM CRFs from Figure 4-11, b) convolutions of GHG CRFs such as the examples in Figure 4-9, c) the combination of SAM CRF convolutions and GHG CRF convolutions minus impact of the estimated SAM trend due to GHG forcing. (The effect of GHGs on SAM is shown in Figure 4-13.) A red cross denotes the ensemble mean of the simulations and reconstructions. 102

4-13 A sample of response functions of the SAM index (SLP_{index}) in 4 CMIP5 models forced with abrupt CO_2 quadrupling. The indices are smoothed with a 25-year running mean and are normalized by the index standard deviations estimated from the preindustrial control simulation of each model. 103

4-14 CMIP5 SO warming bias in the CMIP5 simulations: Circular markers denote the 1979-2014 SO SST trends [°C/decade] in CMIP5 historical simulations extended under the RCP8.5 scenario. Vertical lines indicate two standard deviations of the models' natural variability in the SO SST trends of the preindustrial control experiments. The green horizontal line shows the observed 1982-2014 SO SST trend [°C/decade] according to the NOAA Reynolds Optimum Interpolation dataset. . . 103

4-15 Understanding the CMIP5 SO warming bias: The green horizontal lines in each subfigure show the observed 1982-2014 SO SST trend [°C/decade] according to the NOAA Reynolds Optimum Interpolation dataset. a) Vertical bars denote the 1979-2014 SO SST trends [°C/decade] in CMIP5 historical simulations extended under the RCP8.5 scenario; b) Vertical bars denote the 1979-2014 SO SST trends [°C/decade] in our reconstructions of each CMIP5 simulation; c) Vertical bars denote the 1979-2014 SO SST trends [°C/decade] we obtain after we convolve the GHG and SAM CRFs with observationally-based forcing trends. The SAM forcing trend used for this reconstruction is based on the HadSLP2r dataset. 104

4-16 Regional CRFs to ozone from Marshall et al. [2014]. The green curve is the ensemble mean SO SST response (50S to 70S) from abrupt ozone depletion experiments with the coupled MITgcm. The red curve is the ensemble-mean evolution of the SO SST cooling forced by abrupt ozone depletion in the CCSM3.5 NCAR model. The yellow curve is the SO SST response (50S to 70S) from an abrupt SAM perturbation experiment with an ocean-only version of the MITgcm. We have considered a range of plausible idealized CRFs which span the model-based curves. The thick blue curve indicates the ensemble mean of our idealized CRFs. The shaded blue envelope indicates two standard deviations in the spread of our idealized CRFs, and the vertical hashed lines indicate one standard deviation in the spread. Layout to be modified. 105

4-17 a) Historical net TOA radiative forcing [W/m^2] from Hansen et al. projected into the future assuming that the forcing increases smoothly to 4.5 [W/m^2] in 2100, consistent with the CMIP5 RCP4.5 scenario; b) Observed ozone concentration [DU] over the Antarctic region. The timeseries is extended using projections from the WACCM model; c) Individual convolutions of the GHG and the ozone-hole forcing shown in the top panels with the respective GHG and ozone-hole CRFs from Figure 4-16, yielding timeseries of the SST anomalies in the Arctic north of 50°N (red) and the Southern Ocean 50°S to 70°S (green due to GHGs and blue due to stratospheric ozone). Shaded envelopes span 1 standard deviation of the convolution ensemble; d) Combined SST responses to GHG and ozone forcing. The Arctic north of 50°N is shown in red. The Southern Ocean 50°S to 70°S is shown in blue. The SO SST evolution is the sum of the green and blue curves in c). From Marshall et al. [2014], layout to be modified. 106

List of Tables

2.1 Parameter values for each calibration of the EBM to a CMIP5 model: projected SST equilibrium T_{eq} [units: K], forcing at the time of CO_2 quadrupling $\mathcal{F}_o(t)$ [units: W m^{-2}], climate feedback parameter λ_o [units: W m^{-2} K^{-1}], efficacy of ocean heat uptake ε (nondimensional), rate of heat exchange between the ocean layers q [units: W m^{-2} K^{-1}], thickness of the lower EBM layer h_2 [units: m], total thickness of the two EBM layers [units: m]. The table lists parameter values from the best fits ± the corresponding standard errors calculated from iterative linear regression. The calibrations were done using an iterative least-squares algorithm. The rows correspond to different models: a) ACCESS1-0; b) CCSM4; c) CNRM-CM5; d) GFDL-ESM2M; e) GFDL-CM3; f) MPI-ESM-LR; g) MRI-CGCM3; h) NorESM1-M; μ is the ensemble mean of the models; σ is the intermodel standard deviation. The ensemble mean and the intermodel standard deviation were computed with respect to the results from the best fits. 47

2.2 Correlations among the calibrated EBM parameters: projected SST equilibrium T_{eq} in °C, forcing at the time of CO_2 quadrupling $\mathcal{F}_o(t)$ [units: W m^{-2}], climate feedback parameter λ_o [units: W m^{-2} K^{-1}], efficacy of ocean heat uptake ε (nondimensional), rate of heat exchange between the ocean layers q [units: W m^{-2} K^{-1}], thickness of the lower EBM layer h_2 [units: m]. The **highlighted** correlations are significant at the 95% confidence level. 47

2.3 Alternative metrics for the depth of heat penetration 51

2.4 Alternative metrics for the vertical extent and strength of the AMOC 52

2.5 Alternative definitions of the time-mean AMOC in the abrupt 4×CO_2 experiment 52

2.6 Correlations between heat storage metrics $D_{80\%}$ and H and properties of the control AMOC, the AMOC anomaly, and the 4×CO_2 AMOC. The **highlighted** correlations are significant at the 95% confidence level. 55

3.1 List of CMIP5 Control Simulations 59

3.2 Fitting Parameters. We vary the maximum cutoff lag τ_{max} [Years]. Note that we use only $\tau_{max} = 50$ years and $\tau_{max} = 75$ years for models whose control simulation is shorter than 350 years. We use four different values of $\tau_{max} = 50$ where longer simulations are available. We also select shorter SST timeseries from the full control simulations by removing a certain percent of time steps from the beginning and the end of each model run. 62

Chapter 1

Introduction

The ocean, with its slow circulation and large thermal inertia, plays an essential role in setting the pace of climate response to external forcing and at the same time constitutes a major source of low frequency natural variability. The high latitude oceans provide an important conduit connecting the sea surface to intermediate, deep, and bottom waters. This thesis studies the particular role of the North Atlantic and the Southern Ocean for the uptake, transport, and storage of heat. The accumulation and redistribution of thermal energy affect surface climate on multiple timescales.

1.1 The role of high latitude oceans for the climate response to greenhouse gas forcing

[1]

Forced with greenhouse gases (GHGs), the climate system adjusts towards a new equilibrium on various timescales: ultrafast responses in the stratosphere and troposphere (days and weeks), fast responses of the land-surface and the ocean's mixed layer (months and years), and a long-term adjustment of the deeper ocean (decades to millennia) (*Gregory*, 2000, *Stouffer*, 2004, *Gregory and Webb*, 2008, *Held et al.*, 2010, *Andrews et al.*, 2012). Continental ice sheets and terrestrial ecosystems respond on even slower multi-millennial timescales (*Pagani et al.*, 2010, *Previdi et al.*, 2013). The mechanisms of ocean heat storage are particularly important in the context of historical anthropogenic global warming. Ocean warming accounts for roughly 93% of the anomalous energy accumulation in the climate system between 1971 and 2010 (*Rhein et al., 2013*, 2013).

---

[1] This section has borrowed extensively from an article originally published in Geophysical Research Letters (*Kostov et al.*, 2014).

The ocean response timescales depend not only on the rate at which energy is absorbed at the sea surface (the net ocean heat uptake), but also on the efficiency with which that energy is transported away from the surface and into the ocean interior (*Hansen et al.*, 1985). While early ocean models represented the downward propagation of the warming signal as a diffusive (*Hansen et al.*, 1985) or an upwelling-diffusive process (*Hoffert et al.*, 1980, *Wigley and Raper*, 1987, *Raper and Cubasch*, 1996), modern general circulation models (GCMs) reveal a variety of important vertical heat transport processes at work, such as stirring along sloped isopycnals and advection by the mean ocean circulation (*Gregory*, 2000). Moreover, analyses suggest that differences in ocean heat uptake may play an important role for the large inter-model spread in simulated warming (*Raper et al.*, 2002, *Boé et al.*, 2009, *Hansen et al.*, 2011, *Kuhlbrodt and Gregory*, 2012, *Geoffroy et al.*, 2013a,b). *Xie and Vallis* (2011), *Winton et al.* (2013), *Rugenstein et al.* (2013), and *Winton et al.* (2014) have found that the AMOC impacts the depth of heat penetration under transient climate change. They emphasize that the forced weakening of the overturning circulation affects the rate of surface warming through the redistribution of the background heat content. On the other hand, *Marshall et al.* (2014) and *Marshall et al.* (2015) suggest that the AMOC regulates the climate response to GHG forcing by advecting the anthropogenic heat anomaly in the ocean similarly to a passive tracer.

Thus, key questions are, what physical processes regulate the depth of ocean heat storage, and to what extent do they influence the surface climate response to GHG forcing? We focus on the high latitude regions, the North Atlantic and the Southern Ocean, where the rate of anomalous ocean heat uptake is greatest (*Marshall et al.*, 2015). Chapter 2 explores the importance of the Atlantic Meridional Overturning Circulation for setting the pace of the global climate response to top-of-the-atmosphere radiative forcing. Chapter 4 considers regional responses to greenhouse gas forcing and the Southern Ocean response to ozone forcing. The latter induces a pattern of atmospheric anomalies similar to the Southern Annular Mode of natural variability.

1.2 Response of the Southern Ocean to the Southern Annular Mode

[2]

In contrast to the strong historical global warming trend induced by greenhouse gas forcing, the Southern Ocean (SO) has exhibited a gradual decrease in sea surface temperatures (SSTs) over recent decades (Figure 1-1, (*Fan et al.*, 2014, *Armour et al.*, 2015)). The large-scale geographic patterns of delayed and accelerated warming are related to the climatological background ocean circulation (*Marshall et al.*, 2014, 2015, *Armour et al.*, 2015, *Hutchinson et al.*, 2013, 2015). The high latitudes of the SO constitute an open zonal channel, where the lack of geostrophic meridional flow acts to thermally isolate the Antarctic region and limit poleward heat transport into the SO (*Hutchinson et al.*, 2013, 2015). Moreover, in this region deep waters, unmodified by greenhouse gas forcing, are upwelled at the surface where they take up heat as the mean wind-driven circulation – partially opposed (compensated) by the eddy circulation – transports them northward (*Marshall et al.*, 2015, *Armour et al.*, 2015). The background circulation can therefore slow down the rate of surface warming in the SO relative to the rest of the World Ocean. However, this mechanism of passive heat transport can only dampen the positive surface temperature anomalies and is not sufficient to explain the persistent cooling trends around Antarctica.

Some studies interpret the pattern of observed Southern Hemisphere SST trends as a response to a poleward shift and strengthening of the westerlies. These recent tendencies in the atmospheric circulation resemble the positive phase of the Southern Annular Mode (SAM) of natural variability, but they may in fact be a forced response

---

[2] This section has borrowed extensively from an article submitted for publication and under review in Climate Dynamics (*Kostov et al.*, 2016).

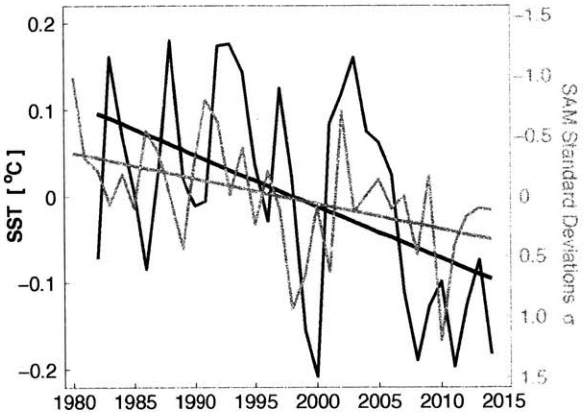

Figure 1-1: Shown in black is the 1982-2014 timeseries of SST [°C] averaged between 55°S and 70°S based on the NOAA Reynolds Optimum Interpolation (*Reynolds et al.*, 2002). The 1980-2014 timeseries of the annual-mean SAM index based on the ERA Interim reanalysis (*Dee et al.*, 2011) is superimposed in gray. The index is defined as the first principal component of SLP variability south of 20°S and is normalized by its standard deviation. Solid lines indicate linear trends fitted to each timeseries. Note the reversed scale for the SAM timeseries shown on the right.

(*Thomas et al.*, 2015), the result of ozone depletion (*Thompson and Solomon*, 2002, *Gillett and Thompson*, 2003, *Sigmond et al.*, 2011, *Thompson et al.*, 2011, *Wang et al.*, 2014). Figure 1-1 illustrates the synchronous evolution of observed SST and SAM anomalies over the SO. The SST averaged between 55°S to 70°S is negatively correlated to the SAM index with $R = -0.65$ at a lag of 1 year. Multiple mechanisms have been proposed to explain the relationship between SST trends around Antarctica and poleward intensification of the westerlies.

Many studies conclude that a poleward intensification of the westerlies impacts SO SSTs by changing the ocean circulation (*Hall and Visbeck*, 2002, *Oke and England*, 2004, *Russell et al.*, 2006, *Fyfe et al.*, 2007, *Ciasto and Thompson*, 2008, *Bitz and Polvani*, 2012, *Marshall et al.*, 2014, *Purich et al.*, 2016). The recent circulation changes have been confirmed by measurements of dissolved passive tracers (*Waugh et al.*, 2013, *Waugh*, 2014). A positive SAM induces anomalous northward Ekman transport in the high latitude region of the Southern Hemisphere (*Hall and Visbeck*, 2002). This gives rise to surface cooling poleward of 50°S. *Ciasto and Thompson*

(2008) and *Sen Gupta and England* (2006) propose that the aforementioned oceanic mechanism complements SAM induced changes in the surface heat fluxes, and that both processes act in concert to set the spatial distribution of temperature anomalies around Antarctica.

Unlike *Ciasto and Thompson* (2008), *Bitz and Polvani* (2012) demonstrate that in the coupled CCSM3.5 GCM, an ozone-driven poleward intensification of the westerlies leads to an increase in SSTs throughout the SO. This result implies that changes in the winds cannot account for the observed cooling around Antarctica and may even have the opposite effect. *Bitz and Polvani* (2012) explain that poleward intensification by itself can lead to a positive SST response via anomalous Ekman upwelling of warmer water in the salinity-stratified circumpolar region. This highlights an apparent divergence in literature about the sign of the SO SST anomalies associated with a SAM-like pattern. A similar lack of consensus also carries over to studies which explore the connection between the westerly winds and SO sea ice. *Hall and Visbeck* (2002) suggest that a positive SAM causes sea ice expansion, while *Sigmond and Fyfe* (2014) demonstrate that poleward intensification (forced by ozone depletion) is associated with a decrease in marine ice extent.

Ferreira et al. (2015) propose a theoretical framework that can resolve this ostensible disagreement about the sign of the SST anomaly associated with a poleward intensification of the westerlies. They use two different coupled GCMs to demonstrate that the SO response to winds in forced ozone depletion simulations is timescale-dependent. An atmospheric pattern similar to a positive SAM triggers short-term cooling followed by slow warming around Antarctica. The fast response is dominated by horizontal Ekman drift advecting colder water northward, while the slow response is sustained by Ekman upwelling of warmer water. *Ferreira et al.* (2015) show that the transition between the cooling and warming regime differs between two coupled GCMs and therefore can be highly model-dependent.

In Chapter 3 we analyze the SO climate response functions (CRFs) to SAM in a large set of state-of-the-art CMIP5 models. We explore mechanisms which affect the SST response on fast and slow timescales. In Chapter 4 we contrast these CRFs to

SAM with the SO SST step-response to GHG forcing. Finally, we use these model-based CRFs to understand the contribution of GHG forcing and SAM anomalies to the historical SST trends in CMIP5 simulations and in observations.

Chapter 2

Impact of the Atlantic Meridional Overturning Circulation on Ocean Heat Storage and Transient Climate Change

[3]

In this chapter we investigate how ocean heat uptake affects the climate response to greenhouse gases within the suite of state-of-the-art GCMs participating in the Coupled Model Intercomparison Project phase 5 (CMIP5) (*Taylor et al.*, 2012). In particular, we analyze standardized simulations in which the atmospheric concentration of CO_2 is instantaneously quadrupled ($4\times CO_2$) from its initial preindustrial value and then held fixed, providing a source of constant forcing for the climate system. In response to this idealized GHG perturbation, heat is taken up by the World Ocean. Part of the excess thermal energy remains in the topmost ($\sim$100 m deep) mixed layer of the ocean, and sea-surface temperatures (SSTs) rise (Figure 2-1a). A substantial amount of heat also penetrates well below the mixed layer, but the vertical distribution of warming differs considerably across models (Figure 2-1b).

---

[3] This chapter is an adapted version of an article originally published in Geophysical Research Letters (*Kostov et al.*, 2014).

Here we focus on the role of the upper cell of the Atlantic Meridional Overturning Circulation (AMOC) for heat transport under GHG forcing. This interhemispheric cell is associated with warm upper ocean waters that flow northward within the top 1 kilometer of the Atlantic basin. They sink at mid-depth in the North Atlantic contributing to the formation of North Atlantic Deep Water (NADW), which then returns southward at approximately 1.5-4.5 kilometers below the surface (*Marshall and Speer*, 2012). We propose that the upper AMOC cell is central to transporting and redistributing thermal energy to depth, thus regulating the effective heat capacity of the ocean under global warming. Moreover, we show that CMIP5 models differ substantially in their representation of the strength and depth of the AMOC, and that this diversity largely accounts for the variability in the vertical distribution of ocean heat storage shown in Figure 2-1b.

To assess the influence of the effective ocean heat capacity on the surface climate response to forcing, we introduce a two-layer energy balance model (EBM), similar in form to that developed in *Gregory* (2000) and *Held et al.* (2010). In our framework the first EBM layer corresponds to the ocean's shallow mixed layer and the second represents the deep ocean interior. Such models have successfully reproduced the global temperature response in a wide range of GCMs (e.g., *Gregory*, 2000, *Held et al.*, 2010, *Li et al.*, 2012, *Geoffroy et al.*, 2012, 2013a,b). We similarly fit our two-layer model to global SSTs from $4\times CO_2$ simulations, but we extend our analysis to interpret the model parameters in terms of physical processes. In particular, we find that the calibrated ocean heat capacity and rate of heat sequestration into the ocean interior are strongly correlated with the depth of heat penetration within the coupled GCMs, which, in turn, appears to be regulated by the vertical extent and strength of the AMOC cell. Finally, we use the two-layer ocean model to quantify the relative contributions of effective ocean heat capacity and climate feedbacks to the inter-model spread in SST response to forcing. Our results suggest that the inter-model spread in SSTs due to variations in the ocean's effective heat capacity is significant, but smaller than the spread due to climate feedbacks.

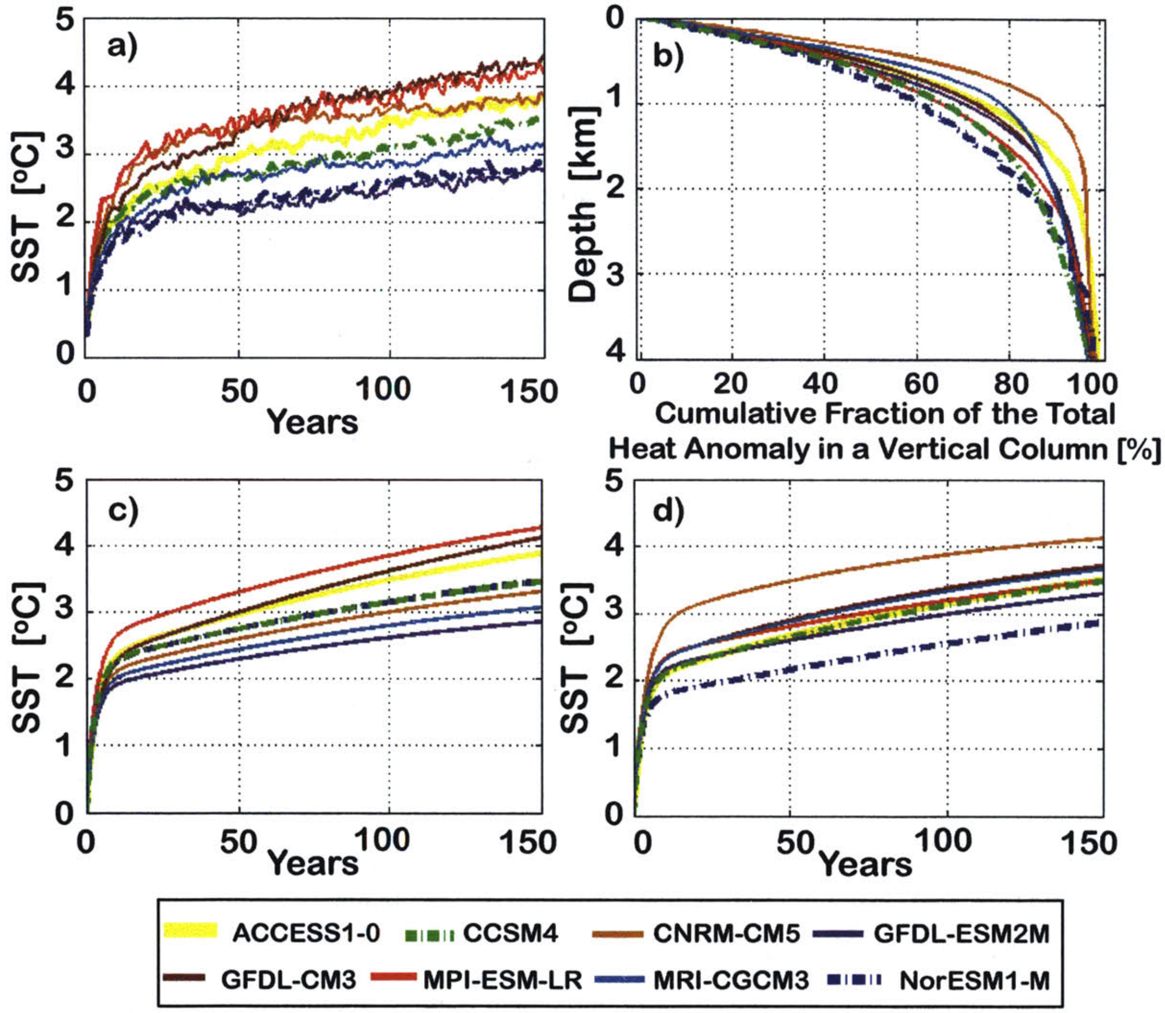

Figure 2-1: a) Area-averaged SST anomaly in CMIP5 4×CO_2; b) Vertical distribution of the ocean heat anomaly in CMIP5 models, averaged over the World Ocean, 100 years after the CO_2 quadrupling; c) SST response under model-specific feedback and forcing (λ_o, $\mathcal{F}_o$), but ensemble-mean ocean properties (q, h_2, ε), as simulated by the 2-layer ocean EBM (see Section 2.2); d) SST response under model-specific ocean properties (q, h_2, ε) but ensemble-mean feedback and forcing (λ_o, $\mathcal{F}_o$), as simulated by the 2-layer ocean EBM (see Section 2.2). The eight CMIP5 models included here are those for which sufficient output was accessible at the time of our analysis (ocean temperature, sea-surface heat flux and AMOC data).

2.1 AMOC and ocean heat storage

In order to evaluate the ocean's role in transient climate change, we analyze the relationship between warming at the sea surface and the distribution of stored heat with depth. We compute the area-averaged SST ($\equiv T_1$) and sea-surface heat flux ($\equiv N_o$) anomalies over the global ocean by subtracting the linear trend of the preindustrial control from each corresponding $4\times CO_2$ simulation. This eliminates unforced drift without adding noise (*Andrews et al.*, 2012). Figure 2-1a shows the notable spread in transient SST responses across the ensemble of GCMs.

The rate of net ocean heat uptake N_o is defined as positive into the ocean and includes net shortwave and longwave radiation, as well as latent and sensible heat fluxes at the air-sea interface. Following CO_2 quadrupling, N_o is initially on the order of 10 Wm^{-2} (Table 2.1) and decreases as the climate evolves toward a new equilibrium. The heat anomaly is initially concentrated in the ocean mixed layer but, over time, penetrates to ever increasing depth. A century after CO_2 quadrupling, warming can be seen at depths of several kilometers (Figure 2-2), but there exists a substantial inter-model spread. Indeed, Figure 2-1b shows that a large fraction of global ocean warming occurs below 1 km in some models (e.g., about 40% for NorESM1-M) while relatively little warming occurs below this depth in others (e.g., about 10% for CNRM-CM5). We define a metric for heat penetration, $D_{80\%}$, as the depth above which 80% of the total global heat content anomaly is contained after one century. $D_{80\%}$ varies considerably across models (horizontal magenta lines in Figure 2-2), with NorESM1-M ($D_{80\%} = 1.8$ km) and CNRM-CM5 ($D_{80\%} = 0.8$ km) as end members.

Various heat transport processes contribute to the distribution of heat storage with depth (e.g., *Gregory*, 2000). Here we propose that the inter-model spread can be largely understood in terms of the different representations of AMOC among the GCMs. The overturning circulation affects vertical heat storage via two main mechanisms: ventilation of the ocean to depth of several km; and redistribution of the background heat content as the AMOC itself changes in response to surface wind and buoyancy forcing (*Xie and Vallis*, 2011, *Winton et al.*, 2013, *Rugenstein et al.*, 2013, e.g.,).

To assess the overall impact of the AMOC, we consider its temporal average over the course of the 4×CO_2 simulations. The volume overturning streamfunctions in the Atlantic-Arctic basin of each model are shown in Figure 2-2. We define a metric for the vertical extent of the upper AMOC cell ($\equiv D_{AMOC}$) as the average depth of the 5 and 10 Sv streamlines in the Atlantic Ocean north of the 35^{o}S parallel (horizontal green lines in Figure 2-2). D_{AMOC} varies from 0.5 km (CNRM-CM5) to 1.8 km (NorESM1-M) and is highly correlated (R=0.93) with the depth of heat penetration $D_{80\%}$ across the models (Figures 2-2 and 2-3a). D_{AMOC} also scales with the maximum of the streamfunction ($\equiv M_{AMOC}$; Figure 2-3b). This result suggests that the propagation of the heat anomaly at depth are linked both to the vertical extent and to the rate of overturning of the upper AMOC cell. The correlation between D_{AMOC} and M_{AMOC} themselves implies that stronger cells also tend to ventilate greater depths, but we acknowledge that this relationship may be intrinsic to our definition of D_{AMOC}. Note that these results are robust with respect to different definitions of D_{AMOC} and $D_{80\%}$.

The important role of AMOC in setting the depth of ocean heat storage becomes clear when we consider the model-mean pattern of the net surface heat flux anomaly (Figure 2-4a). Surface heat uptake between 35N and 70N in the North Atlantic accounts for almost half of the net uptake by the World Ocean. Moreover, the horizontal pattern of anomalous heat distribution at intermediate depths suggests advection of heat along the AMOC cell. We see that 100 years after the step perturbation in GHG forcing, the temperature anomaly at a depth of 1 km is particularly large along the Western Boundary of the Atlantic Ocean and appears to propagate from north to south over time along the lower limb of the upper AMOC cell (Figure 2-4b and c). In contrast, the Pacific and Indian oceans do not show large mid-depth heat anomalies on the same multi-decadal timescales.

These results suggest that the AMOC plays a large role in setting the transient vertical distribution of the global ocean heat anomaly. We next assess the extent to which AMOC accounts for inter-model variability in the ocean's effective heat

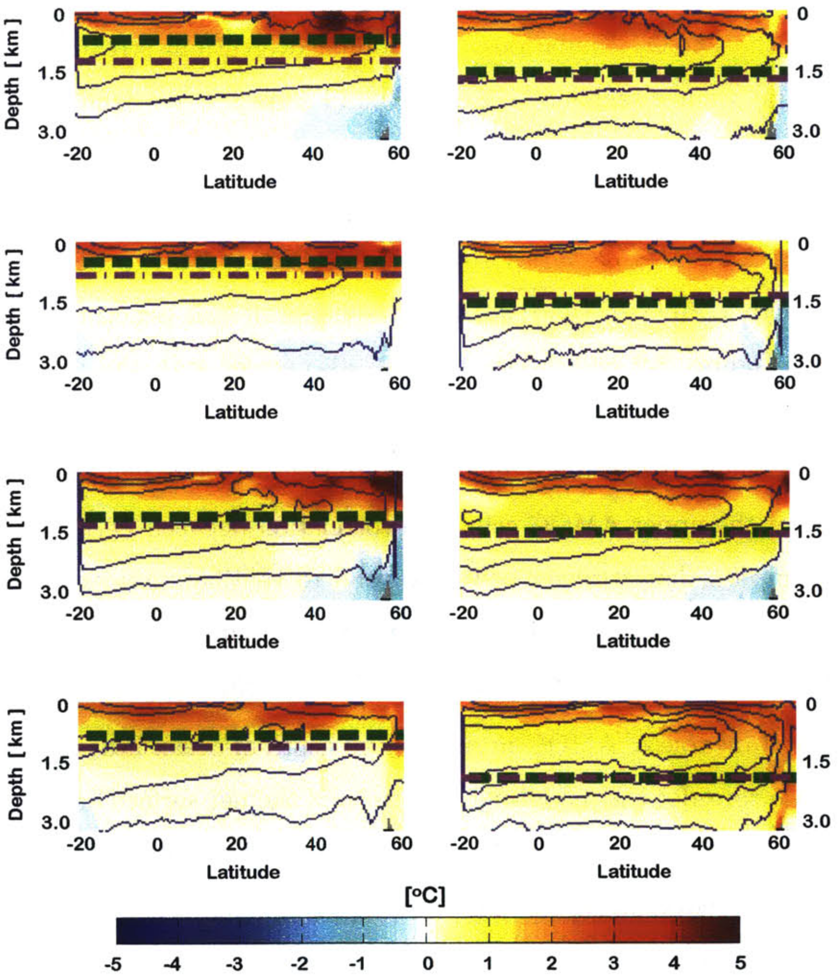

Figure 2-2: Zonal mean potential temperature anomaly in the World Ocean; 30-year average centered 100 years after 4×CO_2. The magenta dash-dotted line marks the average depth above which 80% of the heat anomaly is contained. Overlaid contours mark the upper overturning cell of the AMOC [Sv] between 35S and the Arctic Circle (temporal average over the 150 year 4×CO_2 simulation; contour lines are 5 Sv apart, with an outermost contour at 0 Sv.) The green dashed line denotes the uniform metric for the downward extent, D_{AMOC}, of the upper overturning cell. CMIP5 models: a) ACCESS1-0; b) CCSM4; c) CNRM-CM5; d) GFDL-ESM2M; e) GFDL-CM3; f) MPI-ESM-LR; g) MRI-CGCM3; h) NorESM1-M.

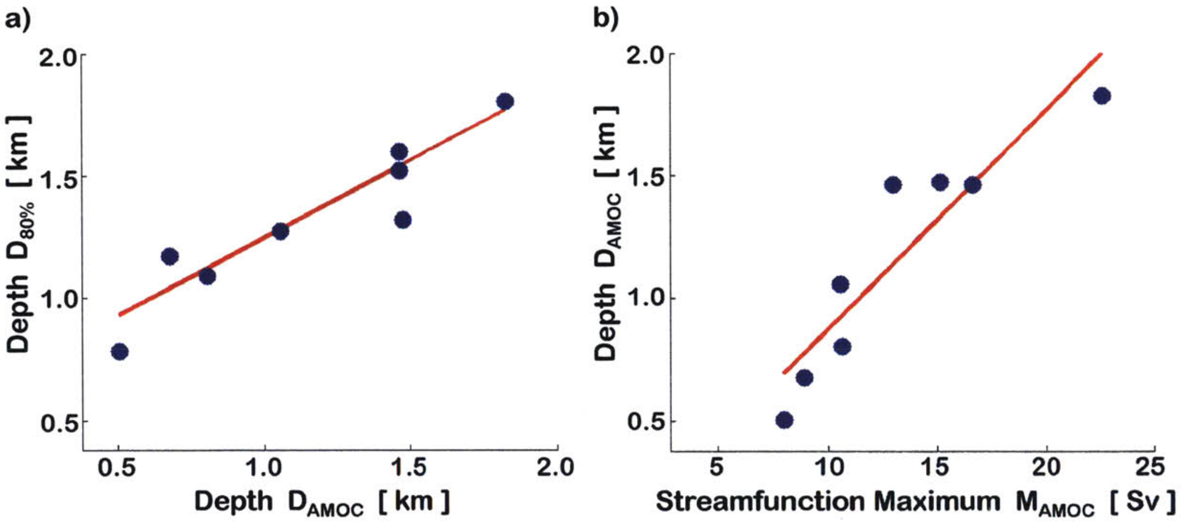

Figure 2-3: a) Correlation between $D_{80\%}$ and D_{AMOC} (R=0.93, p-value p<0.01); b) Correlation between D_{AMOC} and M_{AMOC} (R=0.92, p-value p<0.01).

capacity as diagnosed from the transient SST response to forcing.

2.2 Ocean heat storage and SST response

2.2.1 Representing ocean heat storage in a simple energy balance model

We fit an idealized two-layer ocean energy balance model (EBM) to the SST and the sea-surface heat flux anomalies from each CMIP5 GCM. The two layers in the EBM broadly represent the mixed layer and deeper ocean, with respective temperature anomalies T_1 and T_2. Similar two-layer models have been studied extensively and shown to successfully capture the response of coupled GCMs (e.g., *Gregory*, 2000, *Held et al.*, 2010, *Geoffroy et al.*, 2012, 2013a,b). However, unlike previous applications of this EBM, we attempt to understand the idealized model in terms of key oceanic processes and mechanisms that affect the transient climate response. We thus treat land and the atmosphere as external to our system, and formulate the model as follows.

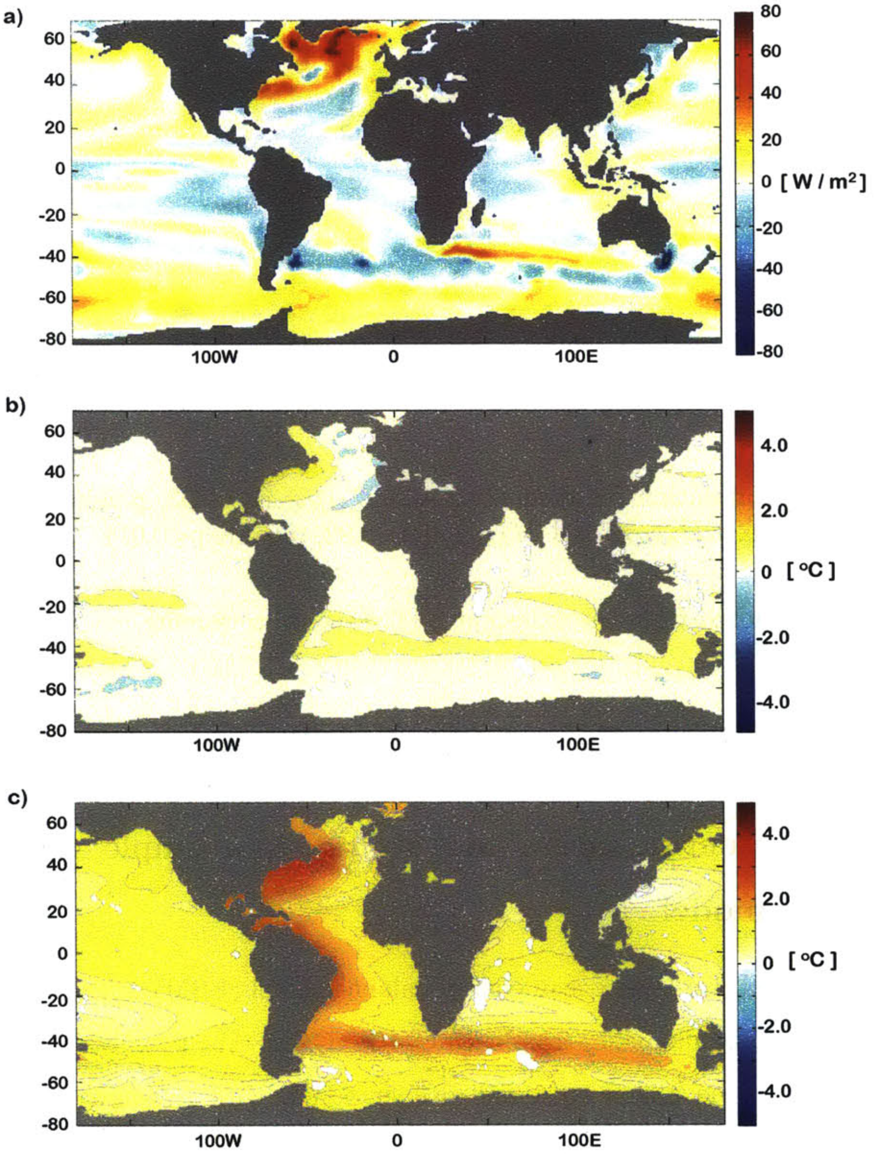
a)
60
40
20
0
-20
-40
-60
-80
100W
0
100E
80
60
40
20
0 [W / m²]
-20
-40
-60
-80
b)
60
40
20
0
-20
-40
-60
-80
100W
0
100E
4.0
2.0
0 [°C]
-2.0
-4.0
c)
60
40
20
0
-20
-40
-60
-80
100W
0
100E
4.0
2.0
0 [°C]
-2.0
-4.0

Figure 2-4: a) CMIP5 4×CO_2 ensemble mean of: a) Net heat flux anomaly at the ocean surface (30-year average centered on year 100); b) Potential temperature anomaly at depth 1,000 m (30-year average centered on year 15); b) Potential temperature anomaly at depth 1,000 m (30-year average centered on year 100).

We are interested in the net heat flux at the ocean surface N_o, which is a combined result of the top-of-the-atmosphere radiative flux anomaly N_{TOA} and the anomalous horizontal exchange of heat with the land domain $H_{L \to O}$ [Watts/m^2]:

$$N_o = N_{TOA} + H_{L \to O}. \tag{2.1}$$

In contrast, previous calibrations of the two-layer EBM to the output of complex models (e.g., *Held et al.*, 2010, *Geoffroy et al.*, 2012, 2013a,b) have not isolated the ocean domain, and have therefore considered only N_{TOA} of the form:

$$N_{TOA} = F_{TOA} - \lambda_{TOA} T_{GlobalAir} - (\varepsilon - 1) H_O, \tag{2.2}$$

where F_{TOA} is a globally uniform top-of-the-atmosphere (TOA) CO_2 forcing, $T_{GlobalAir}$ is the globally averaged anomaly in the near-surface air temperature, and λ_{TOA} is a globally representative linear feedback parameter. To a good approximation, the forcing F_{TOA} in abrupt quadrupling experiments can be represented as a step function.

The last term in (2.2), $(\varepsilon - 1)H_O$, denotes a contribution to the global energy budget that arises from the so-called "efficacy" ε of ocean heat uptake (*Winton et al.*, 2010, 2013, *Held et al.*, 2010, *Geoffroy et al.*, 2013b). This concept is analogous to the efficacy of climate forcings discussed by *Hansen et al.* (2005), who point out that different greenhouse gases and aerosols can give rise to the same globally averaged TOA forcing but different globally averaged temperature responses. In our case we also assume that the efficacy factor ε is constant, but H_O is not. The product $(\varepsilon - 1)H_O$ represents the change in the globally averaged climate feedbacks over time as the correlation between the geographical pattern of ocean heat uptake and the geographical pattern of local surface feedbacks evolves (*Winton et al.*, 2010, 2013, *Armour et al.*, 2013, *Rose et al.*, 2014). Within the GCMs sea-surface heat uptake is not spatially uniform (e.g., Figure 2-4a) and evolves in time as the ocean warms. Moreover, the climate feedbacks, which set the SST damping rate, are sensitive to the pattern of ocean heat uptake, and thus a different set of regional feedbacks are in operation at various stages of the climate response to forcing (*Winton et al.*, 2010, *Armour et al.*, 2013, *Rose et al.*, 2014). The nondimensional "efficacy" factor $\varepsilon \sim \mathcal{O}(1)$ in equation (2.2) accounts for this effect within our idealized, global ocean model. When $\varepsilon > 1$ ($\varepsilon < 1$), we have a time decrease (increase) in the rate at which the globally averaged climate feedbacks dampen surface warming. If $\varepsilon = 1$, the net globally averaged feedbacks do not evolve temporally as the rate of ocean heat uptake changes. In our two-layer EBM framework, the horizontal pattern of heat uptake is not resolved and is assumed to evolve similarly to the vertical ocean heat transport. The latter is in turn proportional to the temperature difference between the layers:

$$H_O = q(T_1 - T_2), \tag{2.3}$$

where q is our constant exchange rate [Watts/K]. Therefore, we can rewrite (2.2) as

$$N_{TOA} = F_{TOA} - \lambda_{TOA} T_{GlobalAir} - (\varepsilon - 1)q(T_1 - T_2). \tag{2.4}$$

We consider the anomalous heat transport from the land to the ocean domain as a function of the SST anomaly T_1 and the anomaly in the near-surface air temperature above land $T_{LandAir}$. Neglecting any nonlinearities, we express $H_{L\to O}$ as:

$$H_{L\to O} = aT_{LandAir} - bT_1, \tag{2.5}$$

where a and b are positive constants (see also *Dommenget* (2009)).

We can simplify (2.5) because we find a strong linear relationship between $T_{LandAir}$ and T_1 across all AOGCMs in the ensemble, as illustrated in Figure 2-5. This linearity allows us to express $T_{LandAir}$ in terms of T_1 as:

$$T_{LandAir} = c_1 T_1 + c_2, \tag{2.6}$$

where $c_1 > 1$, $c_2 > 0$ are constants in each model. By analogy to (2.6), we can extend the same approach to the globally averaged near-surface air temperature, $T_{GlobalAir}$, and describe the latter as a function of SST alone:

$$T_{GlobalAir} = c_3 T_1 + c_4, \tag{2.7}$$

Combining (2.4) through (2.7) gives us the net heat flux at the ocean surface:

$$N_o = F_o - \lambda_o T_1 - (\varepsilon - 1)q(T_1 - T_2), \tag{2.8}$$

with $F_o = F_{TOA} - \lambda_{TOA} c_4 + a c_2$ as an effective step forcing at the ocean surface and the constant $\lambda_o = \lambda_{TOA} c_3 - a c_1 + b$ as an effective SST damping rate.

The temperature anomalies in the two ocean layers, T_1 and T_2, evolve according to:

$$\begin{aligned} c_w \rho_0 h_1 \frac{dT_1}{dt} &= \mathcal{F}_o - \lambda_o T_1 - \varepsilon q(T_1 - T_2), && (2.9) \\ c_w \rho_0 h_2 \frac{dT_2}{dt} &= q(T_1 - T_2), && (2.10) \end{aligned}$$

where c_w and ρ_0 are the specific heat and the reference density of sea water, respectively; h_1 and h_2 are the thicknesses of the two ocean layers; λ_o [units: W m^{-2} K^{-1}] is a climate feedback parameter relating the surface heat flux to the SST; and the term $q(T_1 - T_2)$ [units: W m^{-2}] represents the rate of heat exchange between the mixed layer and deep ocean; parameter ε represents the efficacy of heat uptake as in (2.2). When atmospheric CO_2 is abruptly quadrupled, the upper ocean layer is forced with an energy flux $\mathcal{F}_o(t)$ approximated as a step-function [units: W m^{-2}]. $\mathcal{F}_o$ includes a contribution from heat exchange between the land and the ocean domain and therefore should be interpreted as an effective forcing on the ocean surface. A time-invariant ε is able to capture much of the nonlinear relationship between the surface heat flux and the SST found in the GCMs. Hence, we interpret λ_o as a time-invariant feedback that represents the relationship between equilibrium warming and forcing: $T_{eq} = \mathcal{F}_o/\lambda_o$.

The net sea-surface heat flux N_o is equal to the total heat content change in the

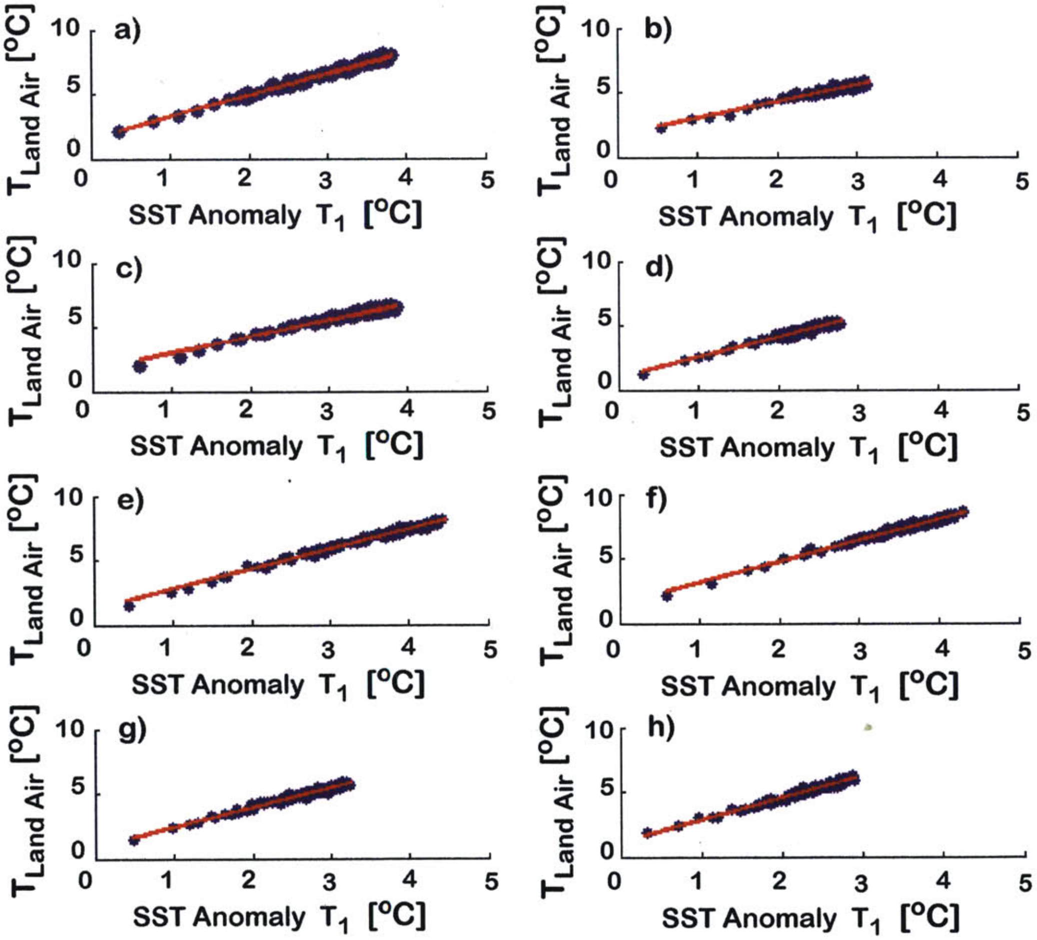

Figure 2-5: Linear relationship between the SST anomaly, T_1, and the temperature anomaly of near-surface air above land, $T_{LandAir}$, in the abrupt quadrupling experiment. Comparison across CMIP5 models: a) ACCESS1-0; b) CCSM4; c) CNRM-CM5; d) GFDL-ESM2M; e) GFDL-CM3; f) MPI-ESM-LR; g) MRI-CGCM3; h) NorESM1-M.

two ocean layers (the sum of equations (2.9) and (2.10)):

$$N_o = \mathcal{F}_o - \lambda_o T_1 - (\varepsilon - 1)q(T_1 - T_2) \tag{2.11}$$

This budget provides a constraint for calibrating the idealized two-layer system to the GCMs. For simplicity, we prescribe a mixed layer depth of $h_1 = 100$m. We thus have five free model parameters to fit: $\mathcal{F}_o$, λ_o, ε, q, and h_2. Finally, the total EBM depth scale is the sum of the two layer thicknesses: $H = h_1 + h_2$.

We then define the rescaled variables $q' = \varepsilon q$ and $h_2' = \varepsilon h_2$ to simplify equations (2.9) and (2.10) as follows:

$$\begin{aligned} c_w \rho_0 h_1 \frac{dT_1}{dt} &= \mathcal{F}_o - \lambda_o T_1 - q'(T_1 - T_2) && (2.12) \\ c_w \rho_0 h_2' \frac{dT_2}{dt} &= q'(T_1 - T_2). && (2.13) \end{aligned}$$

This new system of equations has an analytical solution for the evolution of the SST anomaly T_1 in response to step forcing:

$$T_1(t) = T_{eq} - T_F e^{-\sigma_1 t} - (T_{eq} - T_F)e^{-\sigma_2 t}. \tag{2.14}$$

The SST anomaly approaches the equilibrium value $T_{eq} = \mathcal{F}_o/\lambda_o$ on two exponential timescales: a fast $(1/\sigma_1)$ and a slow $(1/\sigma_2)$ timescale of response (*Held et al.*, 2010). We can expand the rates σ_1 and σ_2 in terms of a nondimensional ratio of layer thicknesses, $r = h_1/h_2' = h_1/(\varepsilon h_2) \ll 1$ to express:

$$\begin{aligned} \sigma_1 &= \frac{\lambda_o}{c_1}\left[1 + \frac{q'}{\lambda_o} + \frac{q'^2}{\lambda_o(\lambda_o + q')} r + \mathcal{O}(r^2)\right] \\ &\approx \frac{\lambda_o + q'}{c_1} && (2.15) \\ \sigma_2 &= \frac{\lambda_o}{c_1}\left[\frac{q'}{(\lambda_o + q')} r + \mathcal{O}(r^2)\right] \approx \frac{1}{c_1}\left(\frac{\lambda_o q' r}{\lambda_o + q'}\right), && (2.16) \end{aligned}$$

where $c_1 = c_w \rho_0 h_1$ is the constant heat capacity of the upper ocean layer. The fast SST response T_F is the fraction of the temperature anomaly that the ocean surface reaches on a timescale $1/\sigma_1$ and can be expressed as

$$T_F \; = \; \frac{\mathcal{F}_o}{\lambda_o}\left[\frac{\lambda_o}{\lambda_o+q'} - \frac{2\lambda_o q'^2}{(q'+\lambda_o)^3}r + \mathcal{O}(r^2)\right] \approx \frac{\mathcal{F}_o}{\lambda_o+q'}. \tag{2.17}$$

Beyond the fast response, the equilibrium warming T_{eq} is approached much more slowly because h_2 is typically an order of magnitude larger than h_1.

2.2.2 Calibrating the Two-Layer EBM to Results from CMIP5 AOGCMs

We calibrate the EBM parameters iteratively in a manner similar to the tuning procedure outlined by *Geoffroy et al.* (2013b). We fit the analytical solution for the upper layer temperature (2.19) to the area-averaged SST anomaly T_1 in each GCM, and we constrain equation (2.18) with the sea-surface heat flux anomaly N_o. This allows us to calibrate our five free parameters. Convergence is achieved after a small number of iterations, and we are able to accurately reproduce the response of each GCM with the EBM.

In the first iteration we impose $\varepsilon = 1$ and regress the surface heat flux anomaly N_o against the SST anomaly T_1 to obtain an initial estimate for λ_o and $\mathcal{F}_o$:

$$N_o = \mathcal{F}_o - \lambda_o T_1. \tag{2.18}$$

We then fit the full analytical solution for the upper layer temperature

$$T_1(t) = T_{eq} - T_F e^{-\sigma_1 t} - (T_{eq} - T_F)e^{-\sigma_2 t}. \tag{2.19}$$

to the SST anomaly T_1 to calculate parameters q and h_2. For subsequent iterations, we proceed as follows. In iteration number i, we use the value of $q^{(i-1)}$ from the previous iteration $(i-1)$ to perform a nonlinear regression of N_o against the surface temperature anomaly T_1 and obtain $\mathcal{F}^{(i)}$, $\lambda_o^{(i)}$, and $\varepsilon^{(i)}$,

$$N_o = \mathcal{F}_o{}^{(i)} - \lambda_o^{(i)} T_1 - (\varepsilon^{(i-1)} - 1) \cdot q^{(i-1)} (T_1 - T_2), \tag{2.20}$$

At the end of the i^{th} iteration, we update the values $q^{(i)}$ and $h_2{}^{(i)}$ by fitting the analytical solution (2.19) to the SST anomaly T_1 using the estimated, $\mathcal{F}_o^{(i)}$, $\lambda_o^{(i)}$, and $\varepsilon^{(i)}$. The EBM parameters converge after a small number of iterations, and we reproduce very well the results of the original CMIP5 models (Figure 2-6). The results of calibrating the two-layer model to each AOGCM are listed in Table 2.1, and the correlations among the parameters are available in Table 2.2.

Our estimate for the depth scale H across the calibrated two-layer EBMs is of the correct magnitude and correlates strongly (R=0.79) with the depth of heat penetration $D_{80\%}$ as diagnosed within the CMIP5 models (Figure 2-7a). As could be anticipated from the close relationship between $D_{80\%}$ and the AMOC depth metric D_{AMOC} identified previously (Figure 2-3a), H is also strongly correlated (R=0.87) with D_{AMOC} (Figure 2-7b). We previously pointed out (Figure 2-3b) a strong connection between D_{AMOC} and the AMOC streamfunction maximum, M_{AMOC}, which regulates the rate of heat transport from the mixed layer into the ocean interior. Likewise, the analogous parameter in the two-layer EBM, q, is found to be strongly correlated with both H (R= 0.89) and M_{AMOC} (R= 0.84); see Figures 2-7c,d and Table 2.2. Our parameter correlations are not sensitive to the choice of $h_1 = 100$m, and are reproduced if we allow h_1 to vary across models. Remarkably, this simple two-layer ocean model, constrained only by SST and surface heat fluxes, captures essential features of the inter-model spread in ocean circulation and heat storage found within the ensemble of coupled GCMs.

In agreement with *Geoffroy et al.* (2013b), who perform a similar EBM calibration, we see that most of the spread in the equilibrium temperature T_{eq} comes from inter-model

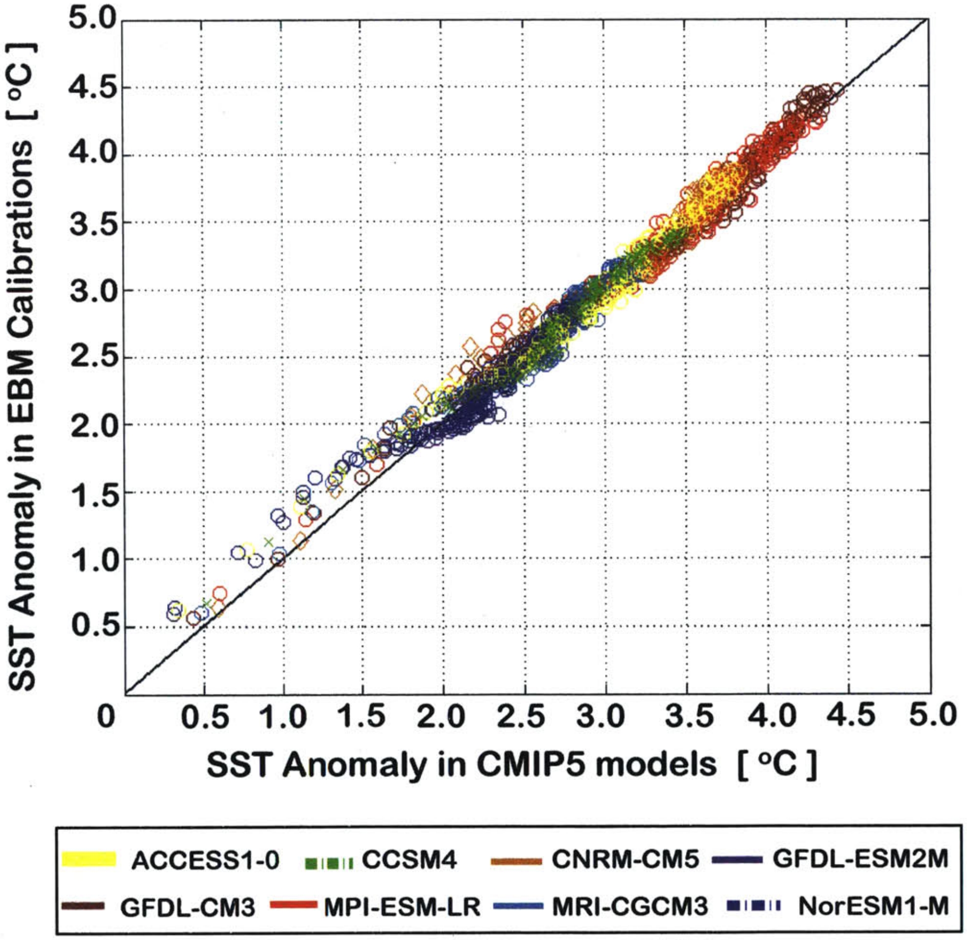

Figure 2-6: Comparison between the annual average global SST response in the original CMIP5 abrupt 4×CO_2 simulations and the SST responses reproduced by the calibrated 2-layer model.

Table 2.1: Parameter values for each calibration of the EBM to a CMIP5 model: projected SST equilibrium T_{eq} [units: K], forcing at the time of CO_2 quadrupling $\mathcal{F}_o(t)$ [units: W m^{-2}], climate feedback parameter λ_o [units: W m^{-2} K^{-1}], efficacy of ocean heat uptake ε (nondimensional), rate of heat exchange between the ocean layers q [units: W m^{-2} K^{-1}], thickness of the lower EBM layer h_2 [units: m], total thickness of the two EBM layers [units: m]. The table lists parameter values from the best fits ± the corresponding standard errors calculated from iterative linear regression. The calibrations were done using an iterative least-squares algorithm. The rows correspond to different models: a) ACCESS1-0; b) CCSM4; c) CNRM-CM5; d) GFDL-ESM2M; e) GFDL-CM3; f) MPI-ESM-LR; g) MRI-CGCM3; h) NorESM1-M; μ is the ensemble mean of the models; σ is the intermodel standard deviation. The ensemble mean and the intermodel standard deviation were computed with respect to the results from the best fits.

Model	T_{eq} [K]	$\mathcal{F}_o \equiv N_o(t \approx 0)$ [W/m^2]	λ_o [W/m^2/K]	ε	q [W/m^2/K]	h_2 [m]	H [m]
a)	5.31	9.99 ±0.40	1.88 ±0.07	1.59 ±0.08	1.68 ±0.05	923 ±20	1023 ±20
b)	4.34	10.99 ±0.43	2.53 ±0.10	1.49 ±0.08	1.79 ±0.05	1007 ±22	1107 ±22
c)	4.24	9.88 ±0.34	2.33 ±0.08	1.02 ±0.06	1.17 ±0.03	592 ±14	692 ±14
d)	3.51	9.69 ±0.52	2.76 ±0.15	1.29 ±0.10	1.91 ±0.06	1474 ±49	1574 ±49
e)	6.26	8.77 ±0.33	1.40 ±0.05	1.34 ±0.07	1.61 ±0.03	862 ±14	962 ±14
f)	5.65	11.80 ±0.47	2.09 ±0.08	1.32 ±0.08	1.56 ±0.03	1167 ±28	1267 ±28
g)	3.85	9.78 ±0.35	2.54 ±0.09	1.34 ±0.07	1.60 ±0.06	916 ±28	1016 ±28
h)	4.38	10.85 ±0.47	2.48 ±0.11	1.71 ±0.09	2.10 ±0.07	1661 ±64	1761 ±64
μ	4.69	10.22	2.25	1.39	1.68	1075	1175
σ	0.95	0.94	0.44	0.21	0.28	347	347

Table 2.2: Correlations among the calibrated EBM parameters: projected SST equilibrium T_{eq} in °C, forcing at the time of CO_2 quadrupling $\mathcal{F}_o(t)$ [units: W m^{-2}], climate feedback parameter λ_o [units: W m^{-2} K^{-1}], efficacy of ocean heat uptake ε (nondimensional), rate of heat exchange between the ocean layers q [units: W m^{-2} K^{-1}], thickness of the lower EBM layer h_2 [units: m]. The **highlighted** correlations are significant at the 95% confidence level.

	T_{eq}	$\mathcal{F}_o$	λ_o	ε	q	h_2
T_{eq}	1	-0.04	**-0.94**	0.12	-0.20	-0.27
F_o		1	0.34	0.28	0.19	0.36
λ_o			1	-0.02	0.30	0.43
ε				1	**0.81**	0.59
q					1	**0.89**
h_2						1

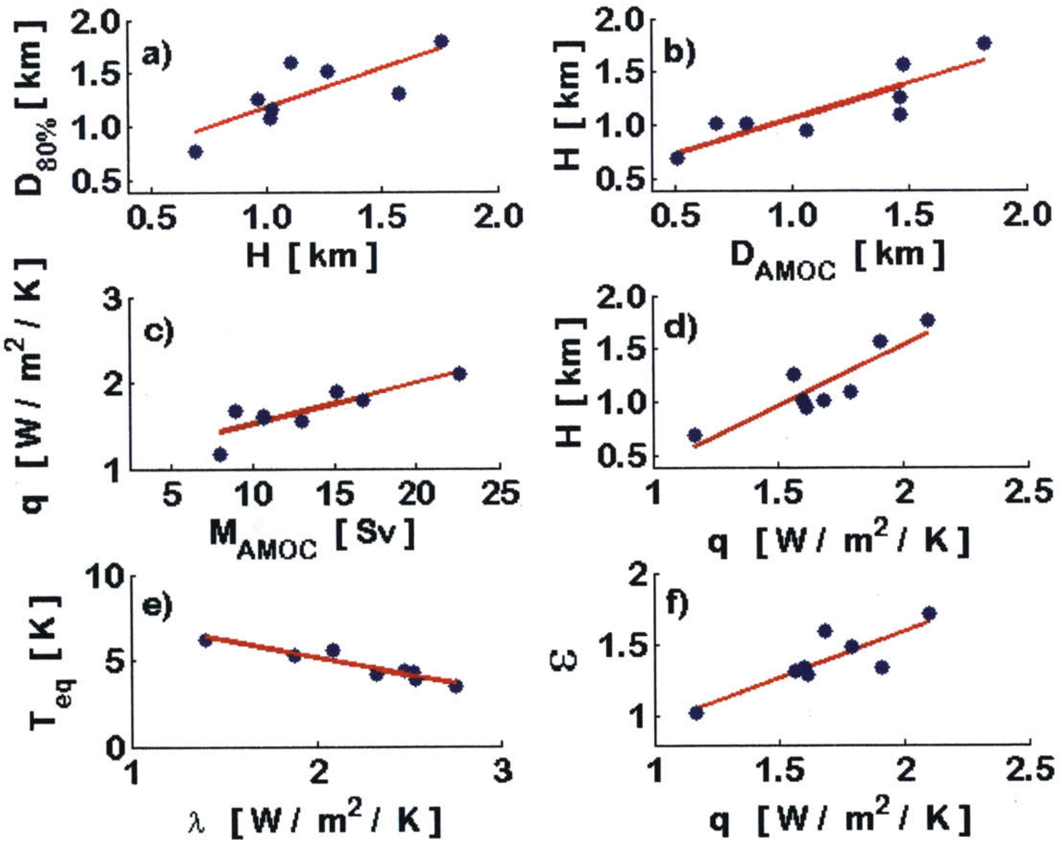

Figure 2-7: Correlations among GCM variables and calibrated EBM parameters with correlation coefficients R and p-values p: a) $D_{80\%}$ and H, (R=0.79, p<0.03); b) H and D_{AMOC} (R=0.87, p<0.01); c) q and M_{AMOC} (R=0.84, p<0.01); d) H and q (R=0.89, p<0.01); e) T_{eq} and λ_o (R=-0.94, p<0.01); f) ε and q (R=0.81, p<0.01).

variability in the feedbacks λ_o, as opposed to $\mathcal{F}_o$ (Figure 2-7e). However, in contrast to our results, *Geoffroy et al.* (2013b) find a small negative correlation between H and q. We suggest that this is due to methodological differences. In particular, *Geoffroy et al.* (2013b) include the ocean mixed layer, the atmosphere, and the land domain in the upper layer of the EBM, while here we have focused on the ocean domain. We also note that we find a significant correlation (R= 0.81) between ε and q (Figure 2-7f), which may reflect the complex relationship between efficacy and the ocean circulation that sets the evolving pattern of surface heat uptake.

We take the remarkable consistencies between coupled GCMs and calibrated EBMs as evidence that the two-layer parameters can be understood in terms of ocean properties (i.e., strength and depth of the AMOC). This further implies that the two-layer calibration produces results that are physically meaningful. We can thus use the EBM to gain insight into the role of AMOC in transient climate change on multi-decadal timescales. For example, a deep and strong AMOC results in a deep penetration of the temperature signal. Within the two-layer EBM, this is represented by a thick layer h_2 and a high rate of heat exchange between the mixed layer and the deep ocean, setting a large effective ocean heat capacity and delaying the SST response to forcing. Such is the case for NorESM1-M, which has the thickest h_2 and the largest q (Table 2.1) and exhibits very slow warming following CO_2 quadrupling (Figure 2-1a).

We can also apply the two-layer EBM to quantify the relative roles of ocean processes and climate feedbacks in setting the inter-model spread in climate response. We separate the parameters into two groups: those related to the ocean circulation (q, h_2, and ε) and those related only to the equilibrium warming (λ_o and $\mathcal{F}_o$). We point out that ε cannot be described simply as an ocean parameter because it depends on the interaction between regional ocean circulations and atmospheric feedbacks (*Armour et al.*, 2013, *Winton et al.*, 2010, *Rose et al.*, 2014). However, q, h_2, and ε are strongly correlated with each other but not significantly correlated with λ_o and $\mathcal{F}_o$ (Table 2.2). Hence, in the context of inter-model spread, we treat ε as a parameter linked to the ocean circulation. We run the two-layer EBM once again, with $\mathcal{F}_o$ and

λ_o specified to the values we diagnosed from each individual GCM calibration, but with q, h_2, and ε, fixed to ensemble-mean values (Figure 2-1c). Together, variations in λ_o and $\mathcal{F}_o$ appear to account for a substantial portion of the inter-model spread in SST response seen in Figure 2-1a, consistent with the findings of *Geoffroy et al.* (2012).

Nevertheless, variations in q, h_2, and ε must be taken into account to obtain the full spread of climate responses in CMIP5. The role of the ocean is particularly important within models that exhibit notably shallow or deep penetration of heat. For example, comparing Figures 2-1a and 2-1c, we see that the SST responses of CNRM-CM5 (weakest AMOC and shallowest heat storage) and NorESM1-M (strongest AMOC and deepest heat storage) are not well reproduced by the EBM under variations in feedbacks alone: SST is underestimated for CNRM-CM5 and overestimated for NorESM1-M. Running the two-layer EBM with GCM-specific q, h_2 and ε, but with ensemble-mean λ_o and $\mathcal{F}_o$, shows that ocean processes are indeed essential to understanding the behavior of individual models (Figure 2-1d) and that variations can yield an SST range of order $\sim 1°$C after several decades. However, this spread is smaller than the spread due to feedbacks and forcing (Figure 2-1c), and also smaller than the inter-model differences in the CMIP5 responses (Figure 2-1a).

These results suggest that although feedbacks λ_o set much of the inter-model variability in the SST response, the ocean circulation plays an important role as well. That is, even if each GCM was governed by the same climate feedback, differences in ocean processes would still yield a notable range of SST responses. Within the two-layer EMB framework, these ocean differences can be understood in terms of an effective ocean heat capacity (set by h_2 and q) and an efficacy of heat uptake ε. Within the ensemble of GCMs, differences in the effective heat capacity can be understood in terms of variations in the depth of heat storage, which in turn reflects the depth and strength of the AMOC.

Table 2.3: Alternative metrics for the depth of heat penetration

Metric	Metric	R	p
$D_{80\%}(110)$	D_{AMOC}	0.94	<0.001
$D_{80\%}(120)$	D_{AMOC}	0.94	<0.001
$D_{80\%}(130)$	D_{AMOC}	0.93	<0.001
$D_{65\%}(100)$	D_{AMOC}	0.89	<0.003
$D_{50\%}(100)$	D_{AMOC}	0.95	<0.001
$D_{80\%}(110)$	H	0.82	<0.02
$D_{80\%}(120)$	H	0.84	<0.001
$D_{80\%}(130)$	H	0.86	<0.006
$D_{65\%}(100)$	H	0.73	<0.05
$D_{50\%}(100)$	H	0.85	<0.01

2.2.3 Results with Alternative Definitions of the Temperature and AMOC Metrics.

We have presented analysis where we define the depth of heat penetration in the GCMs as the level $D_{80\%}$ above which 80% of the total heat anomaly is stored. We use a 30-year time mean centered on the year 100 of the abrupt 4×CO_2 experiment to calculate temperature anomalies relative to the preindustrial control run. Here we show similar correlations where we calculate 30-year time means $D_{80\%}(110)$, $D_{80\%}(120)$, $D_{80\%}(130)$ centered on the years 110, 120, and 130, respectively. We also reproduce our analysis using similarly defined depths of heat penetration $D_{50\%}(100)$ and $D_{65\%}(100)$ taken as 30-year time means centered on the year 100. The correlation coefficients R and p-values are listed in Table 2.3. Other metrics in the table (D_{AMOC} and H) are defined as in the previous section.

In the previous subsection we define the vertical extent of the AMOC cell D_{AMOC} as the average depth of the 5 and 10Sv AMOC streamlines. We use a 150-year time mean AMOC over the course of the abrupt 4×CO_2 experiment. Here we show results using alternative ways to define the AMOC depth. We define $D_{AMOC}(4, 9)$ as the average depth of the 4 and 9Sv streamlines, once again taking a 150-year time mean. Similarly, we introduce $D_{AMOC}(6, 11)$ for the average depth of the 6 and 10Sv

Table 2.4: Alternative metrics for the vertical extent and strength of the AMOC

Metric	Metric	R	p
$D_{AMOC}(4,9)$	$D_{80\%}$	0.92	<0.002
$D_{AMOC}(6,11)$	$D_{80\%}$	0.93	<0.001
$D_{AMOC}(4,9)$	H	0.86	<0.007
$D_{AMOC}(6,11)$	H	0.90	<0.003

Table 2.5: Alternative definitions of the time-mean AMOC in the abrupt 4×CO_2 experiment

Metric	Metric	R	p
$D_{AMOC(100)}$	$D_{80\%}$	0.92	<0.002
$D_{AMOC(100)}$	H	0.85	<0.01
$M_{AMOC(100)}$	q	0.83	<0.02

streamlines. We reproduce correlations similar to the ones found with the AMOC depth metric used in the previous section with correlation coefficients R and p-values listed in Table 2.4.

We also consider a different time-mean to define a new metric for the AMOC vertical extent. We denote the time average depth of the 5 and 10Sv AMOC streamlines between the years 1 and 100 of the abrupt 4×CO_2 experiment $D_{AMOC(100)}$. We define $M_{AMOC(100)}$ as the maximum of the 100-year time mean AMOC in the abrupt quadrupling run. We find that $D_{AMOC(100)}$ is strongly correlated with the depth of heat penetration $D_{80\%}$ and with the layer thickness H of the calibrated EBM (See Table 2.2.3). The AMOC strength $M_{AMOC(100)}$ is in turn correlated with q, the calibrated coefficient of vertical heat transport in the EBM.

The correlations we found using $D_{80\%}(110)$, $D_{80\%}(120)$, $D_{80\%}(130)$, $D_{65\%}(100)$, $D_{50\%}(100)$, $D_{AMOC}(4,9)$, $D_{AMOC}(6,11)$, $D_{AMOC(100)}$, and $M_{AMOC(100)}$ demonstrate that the results of our EBM calibration are robust with respect to our choice of temperature and AMOC metrics.

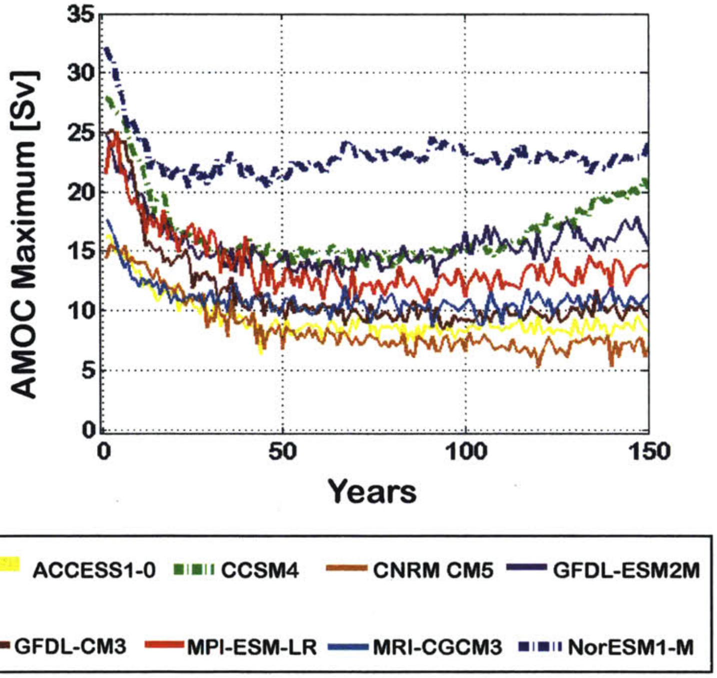

Figure 2-8: Evolution of the annual average AMOC maximum in the abrupt 4×CO_2 runs of CMIP5 GCMs.

2.3 Time Evolution of the AMOC: Weakening and Shoaling of the Circulation in the Abrupt 4×CO_2 Experiment

AMOC in the abrupt quadrupling experiment weakens, and its vertical extent decreases substantially across all GCMs included in our ensemble. The time evolution of the AMOC is shown in Figure 2-8. We have explored the relationship between the control state of the overturning circulation and the circulation in the 4×CO_2 run. We have also considered the impact of the AMOC adjustment on the intermodel spread in ocean heat storage. We define an AMOC anomaly cell as the difference between the 150-year mean 4×CO_2 streamfunction and the preindustrial control streamfunction.

In our ensemble we find a positive but not significant correlation between the control AMOC strength and the 150 year time-average magnitude of the weakening

($p=0.20$). Note that, as shown in Figure 2-8, the AMOC in some models partially recovers after a large transient decrease. Thus, the minimum AMOC strength (i.e., the maximum weakening) is reached before the end of the 150-year abrupt quadrupling run. Thus, we also examine the relationship between the preindustrial control AMOC strength and the value of the maximum weakening, but we do not find a significant correlation ($p=0.20$) between the two metrics. We find a small correlation ($R<0.21$) between the vertical extent of the control AMOC and the vertical extent of the anomaly cell.

In contrast, the correlation between the control AMOC strength $M_{AMOC,Control}$ and the AMOC strength in the $4\times CO_2$ experiment is large ($R=0.86$) and significant ($p<0.01$). Similarly, the correlation between the vertical extent of the AMOC in the quadrupling run, D_{AMOC}, and the vertical extent in the control run, $D_{AMOC,Control}$ is strong ($R=0.88$) and significant ($p<0.004$). Thus, we infer that the depth and strength of the AMOC in the perturbed experiment depend largely on the properties of the control circulation.

Table 2.6 compares the correlations of heat storage metrics q, H, and $D_{80\%}$ with the properties of the control AMOC, the $4\times CO_2$ AMOC, and the AMOC anomaly. The results summarized in Table 2.6 suggest that the AMOC weakening does not contribute significantly to the intermodel spread in ocean heat storage. The correlations of q, H, and $D_{80\%}$ with the control properties of the circulation are strong but weaker than the corresponding correlations with the $4\times CO_2$ AMOC. Thus we propose that the control AMOC contributes to the intermodel spread in heat storage by affecting the properties of the $4\times CO_2$ overturning cell. The ventilation rate set by the $4\times CO_2$ AMOC appears to be the largest source of intermodel variability in the ocean's effective heat capacity and the rate of vertical heat transport.

Table 2.6: Correlations between heat storage metrics $D_{80\%}$ and H and properties of the control AMOC, the AMOC anomaly, and the $4\times CO_2$ AMOC. The **highlighted** correlations are significant at the 95% confidence level.

Heat Storage Metric	Control AMOC Depth	Depth of the AMOC Anomaly Cell	$4\times CO_2$ AMOC Depth
$D_{80\%}$	**0.83**	0.46	**0.93**
H	**0.73**	0.42	**0.87**

Heat Storage Metric	Control AMOC Strength	Strength of the Anomaly Cell	$4\times CO_2$ AMOC Strength
q	**0.81**	0.05	**0.84**

2.4 Discussion and Interpretation of the Results.

We have identified an important role of the upper AMOC cell for regulating heat storage in the World Ocean as represented in an ensemble of state-of-the-art models. Our analysis of CMIP5 GCMs reveals that the AMOC is a major source of inter-model variability in the ocean's effective heat capacity and in the rate at which the heat anomaly is exported from the mixed layer downward (see *Medhaug et al.* (2011) for AMOC variability across CMIP3 models). Models with a deeper and stronger overturning circulation store more heat at intermediate depths, which delays the surface temperature response on multi-decadal timescales.

We note the possibility that other vertical heat transport processes could be correlated with the strength and depth of the AMOC and thus would be neglected in our analysis. However, we have found that a substantial portion of the global ocean heat uptake occurs within a relatively small region in the North Atlantic and that anomalous heat is advected to depth along the upper AMOC cell 2-4. The AMOC can thus be expected to strongly influence the depth of global heat penetration. Several studies [e.g., Xie and Vallis, 2011; Winton et al., 2013; Rugenstein et al., 2013] have found that weakening of the AMOC can also substantially affect the depth of heat penetration through the redistribution of the background heat content. While changes in AMOC do occur within the CMIP5 GCMs under $4\times CO_2$ forcing, we find no significant correlations between the magnitudes of the AMOC weakening or shoaling and the depth of heat storage across the ensemble. Thus, the diversity of AMOC strengths and depths across models appears to be the larger source of inter-model spread in the depth of heat penetration.

To quantify the relative influence of ocean processes versus climate feedbacks in setting the spread of CMIP5 temperature responses, we have employed a simple two-layer ocean model calibrated to each GCM. While much of the inter-model spread is attributed to feedback variations, ocean parameters are found to be important as well, and critical to the response of those models with very deep (or shallow) AMOC cells.

Our results have implications for understanding the climate response to greenhouse forcing and for improving the long-term prognostic power of models. Our findings suggest that a good representation of the AMOC is essential for accurately simulating ocean heat storage and transient warming. These conclusions point to the value of measuring and studying AMOC properties as the circulation evolves under global warming conditions.

This analysis emphasizes the significance of the North Atlantic for setting the pace of transient climate response under greenhouse gas forcing. In the following chapters we consider another high latitude region which plays an important role in ocean heat uptake on a global scale: the Southern Ocean (*Marshall et al.*, 2015). In Chapter 3 we examine the Southern Ocean response to a poleward intensification of the westerly winds, and in Chapter 4 we consider the combined effects of winds and greenhouse gas forcing on the ocean.

Chapter 3

Fast and slow responses of Southern Ocean sea surface temperature to SAM in coupled climate models

[4]

In this chapter we focus on the Southern Ocean (SO) and examine how sea surface temperatures (SSTs) around Antarctica respond to the Southern Annular Mode (SAM) on multiple timescales. To that end we examine the relationship between SAM and SST within unforced preindustrial control simulations of coupled general circulation models (GCMs) included in the Climate Modeling Intercomparison Project phase 5 (CMIP5) (*Taylor et al.*, 2012). We develop a technique to extract the response of the Southern Ocean (55°S–70°S) SST to a hypothetical step increase in the SAM index. By analyzing the GCMs' control simulations, we are able to study the relationship between SAM and SO SST anomalies even in models which have not performed wind override experiments or targeted ozone depletion simulations. We demonstrate that in many GCMs, the expected SST step response function is nonmonotonic in time. Following a shift to a positive SAM anomaly, an initial cooling regime can transition into surface warming around Antarctica. However, there are large differences across the CMIP5 ensemble. In some models the step response function never changes sign and cooling persists, while in other GCMs the SST anomaly crosses over from negative to positive values only three years after a step increase in the SAM. In agreement with *Ferreira et al.* (2015), our findings suggest that anomalous Ekman transport may affect the SO response to SAM on interannual and decadal timescales. Furthermore, we interpret the diversity in the fast and slow responses across the CMIP5 ensemble in terms of the models' time-mean SO stratification. Finally, we use observational data for the ocean temperature climatology to constrain the real SO response to SAM on fast and slow timescales.

---

[4] This chapter is an adapted version of an article submitted to Climate Dynamics and returned for minor revisions (*Kostov et al.*, 2016).

3.1 Data and methods

The GCMs used in this study have made their experimental results publicly available through the CMIP5 initiative (*Taylor et al.*, 2012). In our ensemble we include 23 models that have archived their output of ocean potential temperature, SST, and sea level pressure (SLP). We examine data from the CMIP5 preindustrial control simulations (piControl), which do not have any sources of external forcing. Thus all climate anomalies that we observe in these experiments can be attributed to internal variability. Moreover, the control simulations are hundreds of years long allowing us to perform statistical analysis with large samples of data. Table 3.1 provides additional information about the length of individual CMIP5 simulations. In order to conduct our analysis consistently across the ensemble, we convert all model output fields to the same regular latitude-longitude grid ($0.5^\circ \times 1^\circ$).

We define an annual-mean index for the SAM in each model as the first principal component of variability in SLP south of 20°S. Positive values of this index correspond to a poleward intensification of the westerly winds. In order to remove the secular drift, we linearly detrend the SAM timeseries.

We calculate an area-weighted average of the annual-mean SST anomalies between 55°S and 70°S. We have chosen this latitude range because the anomalous westerlies associated with SAM induce northward transport and upwelling in this zonal band.

Table 3.1: List of CMIP5 Control Simulations

Model Name	Control Run Length [Years]
ACCESS1-0	500
ACCESS1-3	500
BCC-CSM1	500
CanESM2	996
CCSM4	1051
CESM-CAM5	319
CMCC-CM	330
CNRM-CM5	850
GFDL CM3	500
GFDL-ESM2G	500
GFDL-ESM2M	500
GISS-E2-H	540
GISS-E2-R	550
IPSL-CM5A-LR	1000
IPSL-CM5A-MR	300
IPSL-CM5B-LR	300
MIROC5	670
MIROC-ESM	630
MPI-ESM-LR	1000
MPI-ESM-MR	1000
MRI-CGCM3	500
NorESM1-M	501
NorESM1-ME	252

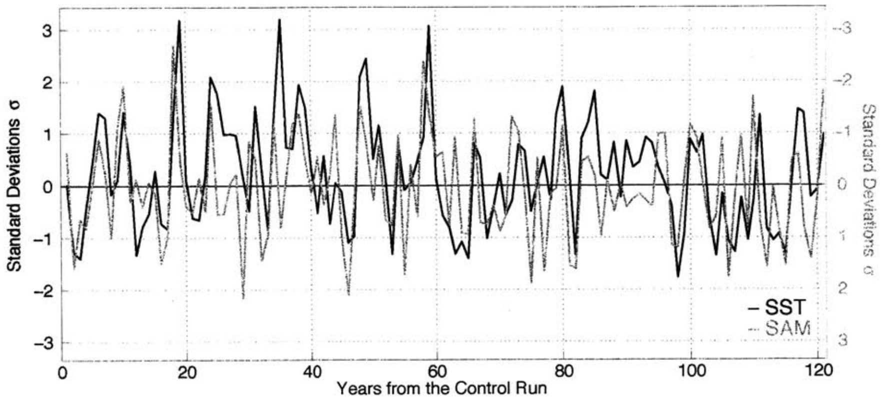

Figure 3-1: Timeseries from the control simulation of model CCSM4: the SAM index in gray and the Southern Ocean (SO) SST anomaly averaged between 55°S to 70°S in black. Each index is detrended and rescaled by its standard deviation. The SST scale is shown on the left vertical axis, and the reversed scale for the SAM index is shown on the right. The SO SST is negatively correlated to the SAM index with $R = -0.37$ at a lag of 1 year.

Further north, the wind anomaly gives rise to downwelling. As with the SAM index, we detrend the SST timeseries to eliminate the long-term drift. A comparison of the SO SST anomalies against the SAM index in CMIP5 models shows negative correlations at short lags (Figure 3-1). This is reminiscent of the synchronous evolution of westerly winds and SO SST seen in observations (Figure 1-1).

For each GCM, we estimate the impulse response function G (a quasi-Green's function) of SO SST (55°S to 70°S) with respect to the SAM index. Following *Hasselmann et al.* (1993), we assume that the temperature timeseries can be represented as a convolution of G with a previous history of the SAM forcing:

$$\begin{aligned} SST(t) &= \int_0^{+\infty} G(\tau) SAM(t-\tau) d\tau + \varepsilon \\ &\approx \int_0^{\tau_{max}} G(\tau) SAM(t-\tau) d\tau + \varepsilon, \end{aligned} \tag{3.1}$$

where $SAM(t)$ is the SAM index normalized by its standard deviation σ_{SAM}, τ is the time lag in steps of years, τ_{max} is an imposed maximum cutoff lag, and ε is residual noise. We discretize equation (3.1) to obtain

$$SST(t) \approx \sum_{i=0}^{I} G(\tau_i) SAM(t-\tau_i)\Delta\tau + \varepsilon, \text{ with } \tau_I = \tau_{max}, \tag{3.2}$$

where coefficients $G(\tau_i)$ represent the response at different time steps after an impulse perturbation of magnitude σ_{SAM}. Each time interval $\Delta\tau$ is equal to 1 year.

We then use a multiple linear least-squares regression of the SO SST signal against the lagged SAM index to estimate $G(\tau_i)$ for $i = 0, .., \tau_{max}$. When performing the regression, we divide the annual SAM timeseries into overlapping segments, each of length τ_{max}.

In our intercomparison we take into account differences in the magnitude of SAM variability across the set of 23 models. We calculate $\overline{\sigma_{SAM}}^{Ens}$, the ensemble mean of the index standard deviations σ_{SAM}. We then rescale the estimated impulse response functions for each GCM, where we multiply $G(i)$ by the corresponding nondimensional ratio $\overline{\sigma_{SAM}}^{Ens}/\sigma_{SAM}$.

By selecting multiple shorter SST and SAM timeseries from the full control simulation and by varying the cutoff lag τ_{max}, we obtain a spread of estimates for the impulse response function $G(\tau)$ in a given model. Table 3.2 lists our fitting parameters and their values. We use the residuals ε to quantify the uncertainty $\sigma_{ImpulseFit}(t)$ on each of these least squares regressions. Figure 3-3a shows examples of impulse response estimates for three CMIP5 models, rescaled by $\overline{\sigma_{SAM}}^{Ens}/\sigma_{SAM}$. Multiple fits span envelopes of uncertainty, while vertical bars denote the error margins $\sigma_{ImpulseFit}(t)$ on each fit. Note that in our analysis we use annual-mean SST. Hence the estimated Year 0 response is not zero, as it represents an average of the SST anomaly over the first months after a positive SAM impulse.

We integrate the impulse response function fits to obtain a spread of estimates for the SO step response function:

$$SST_{Step}(t) = \int_0^t G(\tau)d\tau \approx \sum_{i=0}^{t} G(\tau)\Delta\tau, \tag{3.3}$$

Table 3.2: Fitting Parameters. We vary the maximum cutoff lag τ_{max} [Years]. Note that we use only $\tau_{max} = 50$ years and $\tau_{max} = 75$ years for models whose control simulation is shorter than 350 years. We use four different values of $\tau_{max} = 50$ where longer simulations are available. We also select shorter SST timeseries from the full control simulations by removing a certain percent of time steps from the beginning and the end of each model run.

Fitting Parameter	Parameter Space
τ_{max} [Years]	50, 75, 100, 150
Offset from the beginning of the full timeseries [% of simulation length]	0, 2.5, 5, 7.5, 10, 15, 20, 25, 30, 35, 40
Offset from the end of the full timeseries [% of simulation length]	0, 2.5, 5, 7.5, 10, 15, 20, 25, 30

where $t \leq \tau_{max}$ and $\Delta\tau = 1$ year.

Each of the estimates corresponds to a different combination of start and end times for the timeseries, as well as different choices of τ_{max}. We calculate the mean $SST_{Step}(t)$ and the standard deviation $\sigma_{Spread}(t)$ which characterize our envelope of step response functions for a given model. We furthermore use the $\sigma_{ImpulseFit}(t)$ values to constrain the margin of error $\sigma_{StepFit}(t)$ on each individual estimate in our spread. We then combine $\sigma_{StepFit}(t)$ and $\sigma_{Spread}(t)$ in quadrature in order to quantify the total uncertainty $\sigma_{SSTstep}(t)$ on the mean $SST_{Step}(t)$ for a given GCM.

Figure 3-3b shows example step response functions calculated for the three models presented in Figure 3-3a. For each of the GCMs, we have shown only 100 different estimates, illustrating envelopes of uncertainty. In comparison, in our full analysis we perform more than 350 fits per model by selecting shorter timeseries from the control simulation and by specifying different values for τ_{max}. The vertical bars in Figure 3-3 indicate the error margins $\sigma_{StepFit}(t)$ based on the residuals of each regression.

The step response results are integral quantities, and hence they are smoother than the corresponding impulse response functions. However, a drawback is that the integrated errors grow larger in time. Nevertheless, Figure 3-3b demonstrates that even with generous envelopes of uncertainty and large error bars on the individual fits, we can still distinguish the estimated step response functions of different CMIP5 models.

We use synthetic noisy signals and artificially constructed systems with known step responses in order to test our methodology. The verification procedure is described and illustrated in detail in the following section.

3.2 Verification of the Methodology

We test our methodology from Section 5.1 in order to ascertain its reliability. Our verification procedure involves applying the regression algorithm to systems with a known prescribed step response function. The latter is convolved with a randomly generated order 1 autoregressive timeseries (AR(1)) that is 1000 years long and resembles a SAM forcing. The result of the convolution is our synthetic SST response, which is strongly diluted with a different AR(1) process characterized by longer memory. We choose parameters for the AR(1) models such that their autocorrelations resemble those of SAM and SO SST timeseries in the CMIP5 GCMs (for instance, Figure 3-2a and c). We conduct multiple verification tests with different choices of AR(1) parameters. We also vary the signal to noise ratio in our synthetic SST. Figure 3-2b and d show examples from two different tests.

Within every test we generate an ensemble of multiple synthetic SAM and SST signals with the same statistical properties but different random values. We apply our algorithm separately to each realization in the same fashion as our analysis of CMIP5 control simulations. The verification tests confirm the validity of our method for estimating step response functions.

3.3 Results

Our estimated step response functions suggest notable intermodel differences in the SO SST response to SAM across the CMIP5 ensemble (Figure 3-4). Although all GCMs show initial cooling, many of them transition into a regime of gradual warm-

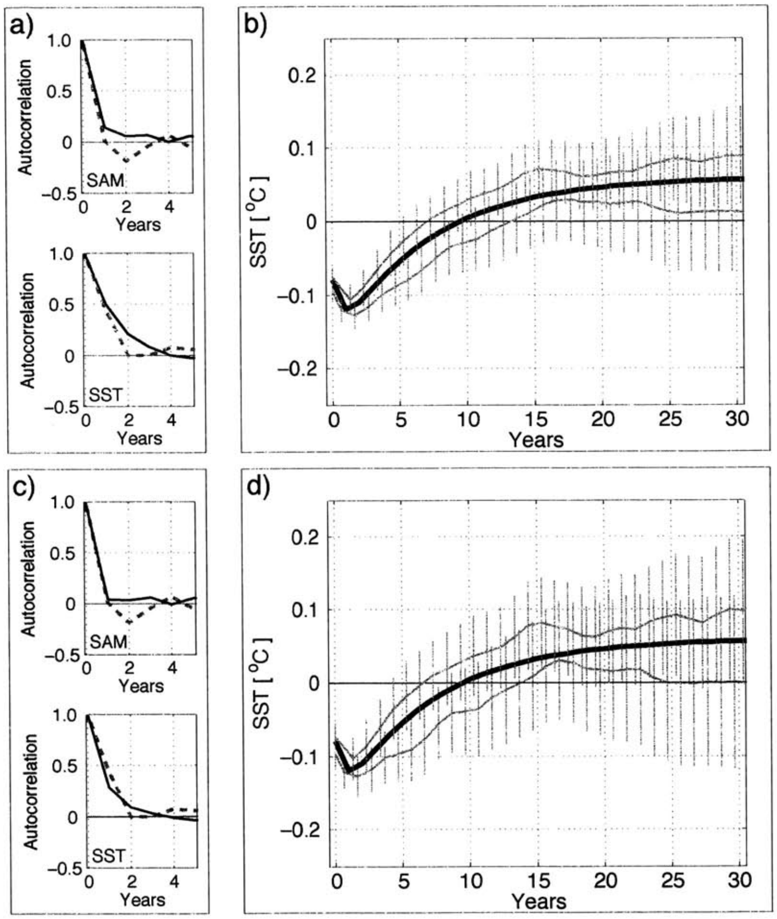

Figure 3-2: Application of the regression algorithm to systems with a known prescribed step response function. On the top row we show a test case where we assume long memory in our SAM and SST signals. The SST signal is diluted such that 60% of the variance is noise. In panel a) on the left, we show the lagged autocorrelations of SAM and SST in CCSM4 (gray dashed curves) and our synthetic artificially generated signals (solid black curves). In panel b) we show applications of the regression algorithm. The thick black curve is the true prescribed step response function. The thin gray curves and the vertical bars denote the estimated step response function $SST_{Step}(t)$ and the uncertainties $\sigma_{SSTstep}(t)$ produced by applying our regression algorithm. The two gray curves in panel b) result from analyzing separate realizations in which we use the same prescribed step response and AR timeseries with the same statistical properties (illustrated in a)) but different random values. On the bottom row we show a test case where we assume shorter memory in the SAM and SST signals, but the SST signal is diluted with more noise, such that the forced response contributes only 20% of the total variance. Panels c) and d) are analogous to panels a) and b).

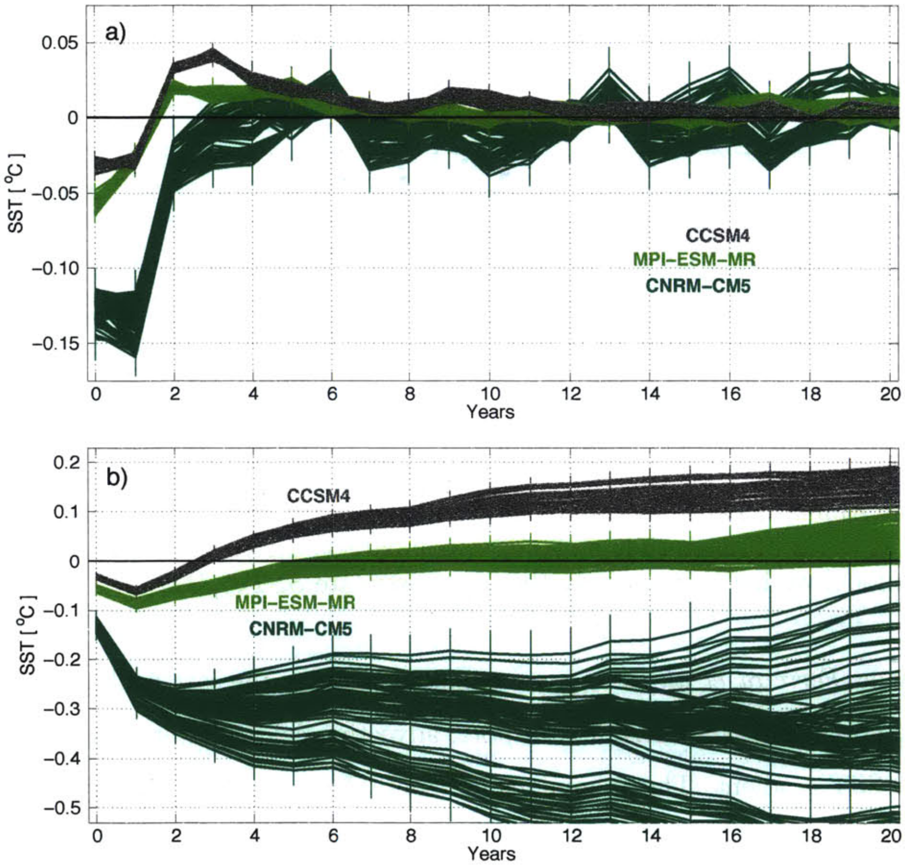

Figure 3-3: Annual-mean response of the Southern Ocean SST anomaly [°C] to: a) a positive impulse perturbation in the SAM index of magnitude equal to $\overline{\sigma_{SAM}}^{Ens}$; b) a positive step increase in the SAM index of magnitude equal to $\overline{\sigma_{SAM}}^{Ens}$. Different colors are used to distinguish the response functions in the three CMIP5 models shown: CCSM4, MPI-ESM-MR, and CNRM-CM5. For each model we show 100 fits that outline an envelope of uncertainty. Vertical error bars denote the margin of error for each fit.

ing. If forced with a positive step increase in the SAM, a number of CMIP5 models – such as CanESM2, CCSM4, and CESM-CAM5 – are expected to show positive SST anomalies in the SO within a few years. In contrast, other ensemble members, including CNRM-CM5 and GFDL-ESM2M, do not exhibit such nonmonotonic response to a poleward intensification of the westerlies and instead maintain negative temperature anomalies persisting for longer than a decade. What sets this intermodel diversity in the way the SO reacts to SAM on short and long timescales?

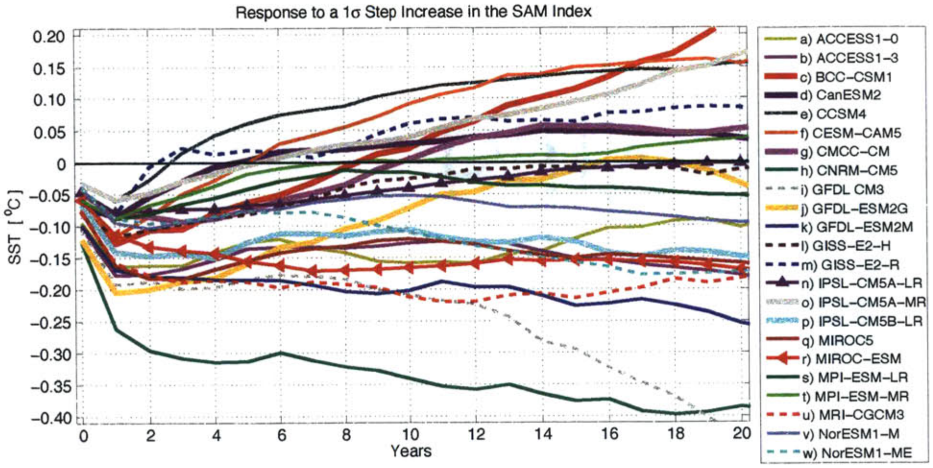

Figure 3-4: Annual-mean responses of the Southern Ocean SST [°C] to a step increase in the SAM index of magnitude $\overline{\sigma_{SAM}}^{Ens}$ – comparison across the CMIP5 ensemble. For each model we have shown only the mean estimate $SST_{Step}(t)$.

Following *Ferreira et al.* (2015), we examine whether the fast cooling regime is related to northward wind-driven transport, advecting colder water up the climatological SO SST gradient. The anomalous horizontal heat flux Q_{hor} $[W/m^2]$ in the SO Ekman layer of depth Z_{Ek} scales as

$$Q_{hor} \;\propto\; C_p \frac{[\tau_x']}{f Z_{Ek}} \partial_y \overline{[SST]}, \tag{3.4}$$

where $C_p \approx 4 \times 10^3$ $J/kg/K$ is the specific heat of water, $[\tau_x']$ is the zonally averaged zonal component of the anomalous surface wind-stress associated with SAM, f is the Coriolis parameter, and $\partial_y \overline{[SST]}$ is the meridional gradient of the zonally averaged climatological SST. As in *Ferreira et al.* (2015), we have assumed that eddy compensation in the thin Ekman layer is much smaller than the anomalous northward wind-driven transport. Since we have rescaled each SST response function by $\overline{\sigma_{SAM}}^{Ens}/\sigma_{SAM}$, we have eliminated some of the intermodel differences due to $[\tau_x']$.

When we perform a weighted least squares linear regression of the estimated Year 1 cooling anomalies from our step responses against $\partial_y \overline{[SST]}$ averaged between 55° and 70°S, we see a strong anticorrelation with a Pearson's $R = -0.72$ (Figure 3-5a). This result is significant at the 5% level with $p < 0.01$ and highlights the importance of horizontal Ekman transport for the fast cooling regime during a positive phase of the SAM.

We also consider the role of Ekman upwelling for influencing the long-term response to a step increase in the SAM index. We assume that the anomalous vertical heat flux Q_{vert} $[W/m^2]$ in a subsurface layer of thickness Z_{sub} can be approximated as

$$Q_{vert} \;\propto\; -\delta\gamma C_p \left(\frac{\partial}{\partial y}\left[\frac{\tau_x'}{f}\right]\right)\frac{\Delta_z\overline{[\theta]}}{Z_{sub}}, \tag{3.5}$$

where $\Delta_z\overline{[\theta]}$ in °C is the inversion (i.e., the maximum vertical contrast) in the time-mean ocean potential temperature within the layer, and γ (unitless) denotes the efficiency with which the subsurface warming signal is communicated into the mixed layer. Parameter δ is a nondimensional factor $0 \leq \delta \leq 1$ that indicates whether we have full ($\delta = 0$), partial ($0 < \delta < 1$), or no ($\delta = 1$) compensation of the anomalous Ekman upwelling by the eddy-induced circulation.

If the slow response is indeed governed by upwelling of warmer water below the mixed layer, the bolus circulation cannot be neglected (*Ferreira et al.*, 2015). As discussed by *Ferreira et al.* (2015), local eddy compensation at depths of hundred meters may be much larger than in the thin Ekman layer. Moreover, the fraction of eddy compensation $(1 - \delta)$ is model dependent. The representation of mixed layer entrainment processes also differs across the CMIP5 ensemble. We therefore expect that both δ and γ may contribute to the intermodel spread in the slow SST response, along with the climatological SO temperature inversion $\Delta_z\overline{[\theta]}$.

Using Equation 3.5 as an Ansatz, we test the importance of the background thermal stratification $\Delta_z\overline{[\theta]}$ for contributing to differences in the slow response among CMIP5 GCMs. We calculate the average slope Λ $[°C/year]$ of the step response functions between Year 1 and Year 7 after a step increase in the SAM and the standard error (SE) for each model estimate. In many models this slope is predicted to be positive, corresponding to a slow warming. We compare Λ against the vertical temperature inversion $\Delta_z\overline{[\theta]}$ for the area-averaged water column between 55° and 70°S and between depths of 67 m and 510 m by performing a weighted least-squares linear regression. We have chosen a vertical range which roughly encompasses the summer minimum and the winter maximum SO mixed layer depths of CMIP5 models (*Salleé et al.*, 2013). We find that the slow response rates Λ across models are positively correlated with $\Delta_z\overline{[\theta]}$, with $R = +0.45$ (Figure 3-5b. This result is statistically significant with $p < 0.05$. It emphasizes that Ekman upwelling acting on the background temperature gradients contributes substantially to the intermodel spread in the slow SST responses to SAM.

The correlation between the rate Λ and the vertical temperature inversion $\Delta_z\overline{[\theta]}$ is not as strong as our result linking the rapid cooling response to the meridional SST gradients. We propose that the slow regime is more complicated than the fast one due in part to air-sea heat exchange (*Ferreira et al.*, 2015) but also due to multiple diverse processes within the ocean domain such as eddy compensation and mixed layer entrainment represented by coefficients δ and γ in Equation 3.5.

We acknowledge that the data points in our intermodel correlation analysis of the fast and slow response (Figures 3-5a and 3-5b) do not necessarily represent independent samples. Some CMIP5 ensemble members are in fact multiple versions of the same GCM with a different horizontal resolution (e.g., MPI-ESM-LR and MPI-ESM-MR). Other ensemble members are developed by the same institution (e.g., GFDL-CM3, GFDL-ESM2G, and GFDL-ESM2M) or belong to the same family of models and hence share common code or parameterizations (*Knutti et al.*, 2013). Thus it is possible that we are inflating our sample size by redundantly including interdependent GCMs. On the other hand, we cannot know a priori which models may exhibit similarities or differences solely on the basis of their common genealogy. For instance, models MIROC-ESM and MIROC5 are related, but their predicted fast SST responses to SAM are statistically different (Figure 3-5a).

3.4 Connecting Our Model-Based Results to the Real Southern Ocean

While acknowledging the limitations of this regression analysis, we attempt to extend our CMIP5 results to the real SO and place an observational constraint on the SST response to SAM. We calculate the climatological meridional SST gradients $\partial_y\overline{[SST]}$ using data from the Reynolds Optimum Interpolation (*Reynolds et al.*, 2002) and compute a metric for time-mean vertical contrast in potential temperature $\Delta_z\overline{[\theta]}$ using the Hadley Centre EN4 product (*Good et al.*, 2013). We use these observationally based climatological SO temperature gradients and the linear relationships found among CMIP5 models (Figure 3-5) to estimate the fast and slow responses in the real SO (denoted with stars in Figures 3-5a and 3-5b). Our results suggest an expected cooling of −0.13°C with a standard error of 0.01°C one year after a step increase in the SAM index. This is likely to be followed by a gradual reduction in the negative SST anomaly at a rate of 0.014°C/year with a standard error of 0.003°C/year.

We then calculate a range of model-based estimates for the real SO response. We quantify the bias that each model exhibits with respect to the observed $\partial_y\overline{[SST]}$ and $\Delta_z\overline{[\theta]}$ in the SO. Then following the bias-correction methodology of *DeAngelis et al.* (2015), we use the relationships from Figure 3-5 to quantify how a deviation from the observed $\partial_y\overline{[SST]}$ or $\Delta_z\overline{[\theta]}$ introduces an expected bias in the models' fast and slow responses, respectively. We then subtract these biases from the estimated fast and slow responses of each ensemble member (Figure 3-6a),b)). We assume that the uncertainty in our initial model-specific estimates is not affected by this linear bias-correction. We calculate weighted means and weighted standard deviations of the bias-corrected model spreads in the fast and slow responses, where we rescale each data point in our sample by the inverse of the SE squared. Note that the weighted bias-corrected ensemble means reproduce the same estimates for the real SO response as the linear relationships in Figure 3-5: a fast cooling of −0.13°C followed by slow warming at a rate of 0.014°C/year. Finally, we use our results to constrain an envelope of uncertainty on the step response of the real SO to SAM (See schematic Figure 3-

6c). Our bias-corrected analysis for the real SO suggest that the expected Year 1 cooling of −0.13°C has an ensemble standard deviation (SD) of ±0.027°C, while the estimated slow response rate of 0.014°C/year has an SD of ±0.013°C/year.

3.5 Discussion and Interpretation of the Results

In this study we have analyzed CMIP5 preindustrial control simulations and examined how SAM forces SO SSTs. In many GCMs the SST exhibits a two-timescale response to SAM: initial cooling followed by slow warming. As in *Ferreira et al.* (2015), we interpret the evolution of these temperature anomalies in terms of the wind-driven circulation redistributing the background heat reservoir. We show evidence that anomalous equatorward transport of colder water is related to the fast cooling response south of 50°S. Our results also suggest that the slow warming regime found in many GCMs is sustained by Ekman upwelling of warmer water in the haline stratified SO.

Across the CMIP5 ensemble, we find a notable intermodel spread in the SO SST response to poleward intensification of the westerlies. We relate part of the diversity of step response functions to differences in the background thermal stratification among the models. GCMs that have small meridional and large vertical temperature gradients in their SO climatology tend to transition faster between the initial cooling and the slow warming regime. Our results imply that a realistic ocean climatology is one of the important prerequisites for successfully simulating the SST response to SAM.

The model-specific results of our analysis have implications for attribution studies which evaluate the effects of greenhouse gas forcing and ozone depletion on the SO. For example, *Sigmond and Fyfe* (2014) analyze CMIP3 and CMIP5 output to determine the impact of the ozone hole on SO sea ice. Similarly, *Solomon et al.* (2015) design and conduct numerical experiments with CESM1(WACCM) to study how ozone depletion affects the circulation and sea water properties of the SO. Such in-depth attribution studies often employ a limited set of GCMs – for instance, only a few CMIP5 modeling groups provide output from ozone-only simulations (*Sigmond and Fyfe*, 2014). However, individual GCMs have various biases in their mean ocean climatology [e.g., *Meijers et al.*, 2014; *Salleé et al.*, 2013]. Thus, we emphasize that the outcome of attribution experiments can be sensitive to the choice of models used. Realistic background temperature gradients are a prerequisite for simulating successfully the response of the SO to a poleward intensification of the westerlies, as the one seen in numerical experiments with ozone depletion.

Our results also identify criteria for constraining and critically assessing future projections of the Southern Hemisphere SST anomalies. Under scenarios with extended greenhouse gas emissions and gradual ozone recovery, CMIP5 models predict a significant and lasting poleward intensification of the westerlies throughout the 21st century (*Wang et al.*, 2014). Based on our analysis, we suggest that those models which have smaller biases in their climatological stratification provide better estimates of future SST anomalies in the SO.

We point out that in our analysis we have neglected seasonal variations in ocean stratification and their impact on the SO SST response to wind changes. *Purich et al.* (2016) emphasize that in the summer a warm surface lens caps the colder subsurface winter water. Therefore, during this season, anomalous Ekman upwelling may complement rather than counteract the cooling effect of northward Ekman transport.

Our study has further limitations in its ability to account for the multiple diverse processes that take place in the SO. For example, *de Lavergne et al.* (2014) show that there are large differences among the CMIP5 models in their representation of deep convection around Antarctica. It is possible that certain GCMs which do not have strong SO convection, such as BCC-CSM1 and CNRM-CM5 (*de Lavergne et al.*, 2014), may not be able to efficiently communicate a subsurface temperature signal into the mixed layer. This in turn may affect the slow warming response to SAM in these models. The recurrence of convective and nonconvective periods in GCMs can also modify the variability of SO stratification about its mean climatology and affect the transition between the fast and slow SST responses (*Seviour et al.*, 2016).

Another potential deficiency in our work pertains to our treatment of atmosphere-ocean coupling. We have not explored any possible intermodel differences in the response of SO surface heat fluxes to SAM. In our linear response function analysis, we have also assumed that the SAM wind pattern forces the SST but not vice versa. However, *Sen Gupta and England* (2007) suggest that SO SST anomalies may feed back on the atmospheric circulation and increase the persistence of SAM. We treat such mechanisms as a source of error contributing to the uncertainty on our estimates of the step response functions.

It is also important to note that the CMIP5 ensemble members used in our analysis do not resolve eddies and rely on parameterizations. Therefore, these GCMs may be missing an important element of the ocean's response to winds. *Böning et al.* (2008) present observational evidence indicating that isopycnal slopes in the SO have not changed over the last few decades despite trends in the SAM. The *Böning et al.* (2008) results are consistent with the eddy-compensation phenomenon and support the possibility that unresolved eddy processes can strongly modulate anomalies in the wind-driven circulation. Despite this shortcoming of our study, we reiterate that it is important to understand how poleward intensifying westerlies impact the SO in the very same models that are widely used to analyze historical climate change and make authoritative future projections.

Finally, our analysis can be used to make a qualitative estimate for the SST response to SAM in the real SO. Our results suggest that during a sustained positive phase of the SAM, SO SSTs can exhibit a non-monotonic evolution. A strong and rapid transient cooling may be followed by a gradual recovery. However, our results do not suggest a high warming rate during the slow response to SAM.

Our results have implications for surface heat uptake in the real SO and for the persistent expansion of the sea ice cover around Antarctica. The positive SAM trend over the last decades may have allowed a cooler SO to absorb more excess heat from the atmosphere in a warming world. Furthermore, SAM-induced negative SST anomalies may have contributed to the observed increase in SO sea ice extent [*Holland et al.*, 2016; *Kostov et al.*, 2016a]. However, if the real SO exhibits a two-timescale response to SAM, the observed SST trends may reverse sign. Hence a sustained poleward intensification of the westerly winds – due to ozone and greenhouse gas forcing – can eventually contribute to a surface warming of the SO, a decreased rate of heat uptake, and a reduction in sea ice concentration. It is therefore important to constrain both the short-term and the long-term SO SST response to SAM. In the following chapter we use the CMIP5 step response functions to SAM in order to understand the historical SO climate change in observations and GCM simulations.

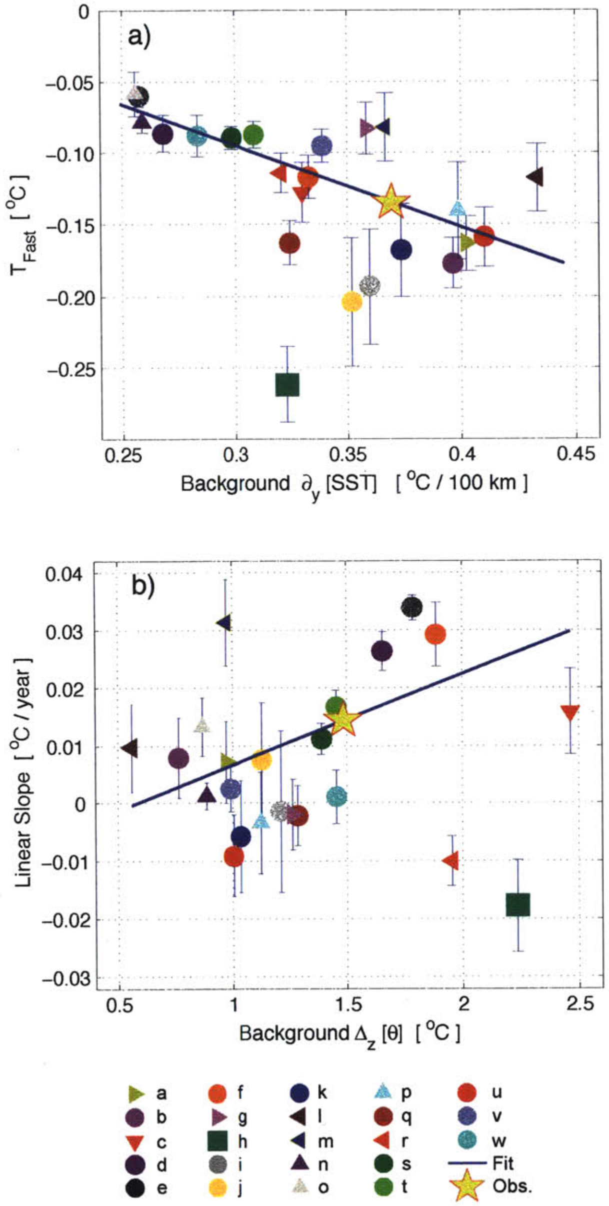

Figure 3-5: a) Relationship between the models' climatological meridional SST gradients $\partial_y\overline{[SST]}$ [°C / 100 km] in the Southern Ocean (55°-70°S) and the Year 1 SST response $SST_{Step}(t=1)$ [°C] to a step perturbation in the SAM index. The vertical error bars correspond to $\sigma_{SSTstep}(t=1)$. b) Relationship between the climatological temperature inversion $\Delta_z\overline{[\theta]}$ [°C] in the Southern Ocean (depth levels 65 m to 550 m) and the SST warming rate Λ [°C / year] which characterizes the slow response to a step increase in the SAM index. Legend: both a) and b) use the same color code and alphabetical order as in Figure 3-4 to distinguish the CMIP5 models analyzed. Straight lines indicate linear fits to the scatter where each data point in the regression analysis is weighted by the inverse of the SE squared. The yellow stars denote estimates for the response of the real Southern Ocean based on observed climatological meridional SST gradients between 55°S and 70°S (NOAA Reynolds Optimum Interpolation *Reynolds et al.* (2002)) and the climatological $\Delta_z\overline{[\theta]}$ inversion (Hadley Centre EN4 dataset, *Good et al.* (2013)).

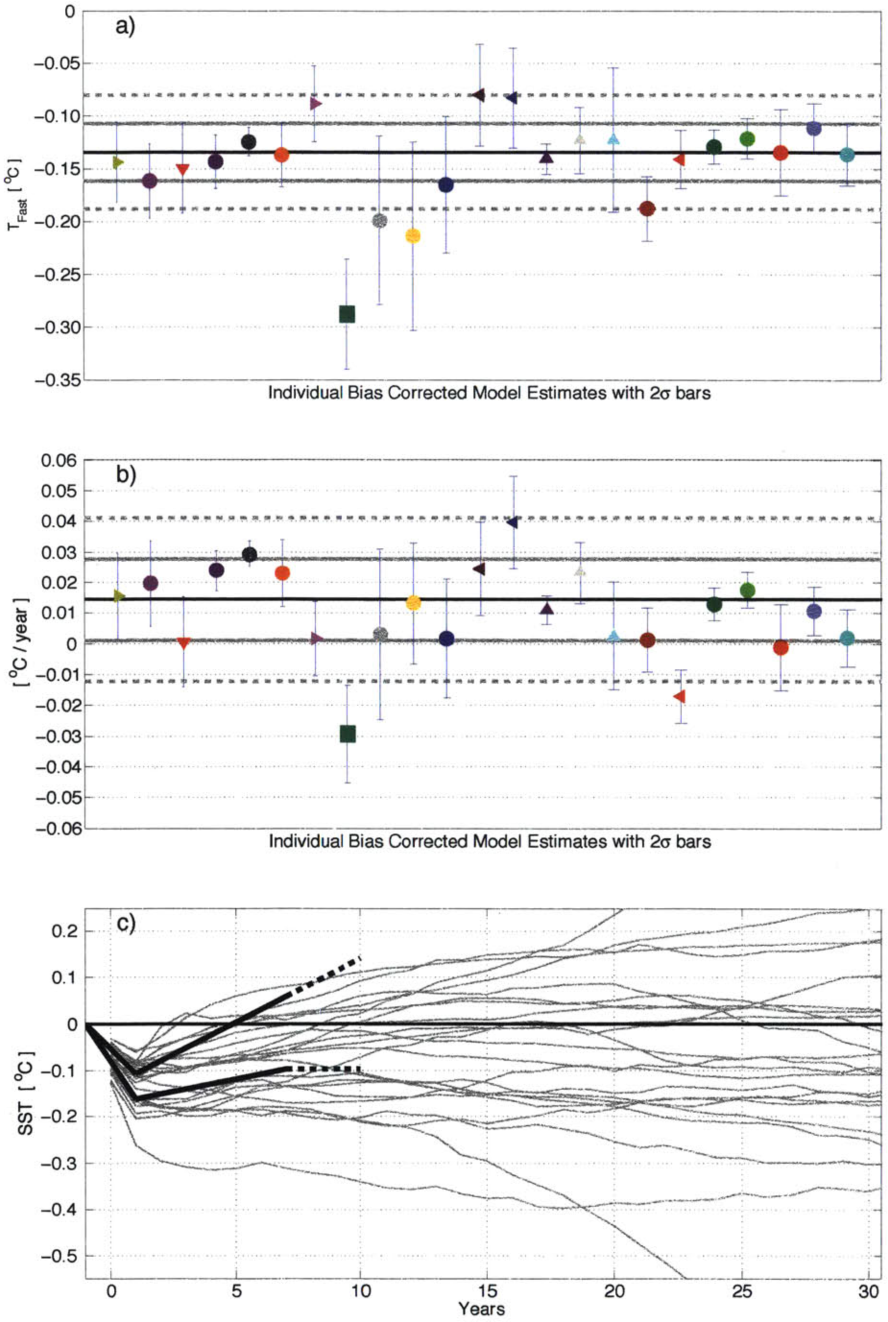

Figure 3-6: a) Scatter: estimated fast responses [°C] after correcting for the model bias in the climatological meridional SST gradients relative to observations (same color code as in Figure 3-5). Vertical error bars denote 2 SE. The horizontal black line is the weighted mean of the model estimates. The solid (dashed) gray lines denote one (two) weighted standard deviations (SD) of the spread. b) Same as in a) but for the slow response rates [°C/year] after correcting for the bias in $\Delta_z\overline{[\theta]}$. c) Solid black lines: a schematic for the estimated response of the real SO SST [°C] based on a) and b). We show the ensemble mean bias-corrected fast response ± 1 SD. This is extended until Year 7 with lines matching the ensemble mean bias-corrected slow response ± 1 SD. Dashed lines show a linear extrapolation at a constant rate or a constant temperature. Gray lines replicate the Fig. 3-4 SO SST step responses [°C].

Chapter 4

Southern Ocean cooling and sea ice expansion in a warming world

[5]

In this chapter we investigate why historical simulations with state-of-the-art CMIP5 global climate models do not reproduce the observed 1979-2014 Southern Ocean cooling trend and, instead, predict slow but steady warming throughout the region and continuous sea ice loss (Figure 4-1). We attempt to explain both the behavior of GCMs and the possible physical mechanisms behind the observed trends around Antarctica. We use the Southern Ocean(SO) response functions to SAM (Southern Annular Mode) from Chapter 3 [Kostov et al., 2016] and we combine them with regional climate response functions (CRFs) to greenhouse gases (GHGs) based on the same suite of CMIP5 models. We convolve the two sets of CRFs with the respective SAM and GHG forcing trends simulated in the CMIP5 historical experiments. This allows us to reconstruct the 1979-2014 historical simulations of Southern Ocean SST. The successful application of the CRF framework shows that we can break down the simulated Southern Ocean SST trends into a contribution due to GHGs, a contribution due to the SAM, and natural variability not already accounted for by the SAM index. We also estimate how each of the aforementioned factors affects the intermodel spread of SO trends across the CMIP5 ensemble. We offer additional verification of this methodology by using the SAM CRFs to reproduce the sea surface temperature (SST) trends from selected 30-year periods of the CMIP5 control runs marked by strong SAM tendencies. Moreover, we examine the contemporaneous trends in sea surface salinity (SSS), ocean heat distribution, and sea ice concentration (SIC). We point out that the composited SIC responses reflect very closely the spatial pattern of SAM induced SST anomalies. Finally, we show that if we convolve a plausible combination of CMIP5 GHG and SAM response functions with the respective timeseries of radiative forcing and the SAM index, we obtain Southern Ocean cooling similar to the one seen in observations. We then perform a similar analysis using a combination of GHG and ozone response functions to recover the observed cooling.

---

[5] This chapter forms the basis for two articles, *Kostov et al.* (2016a) and *Kostov et al.* (2016b), that will be submitted for publication.

Section 4.1 analyzes the effect of multidecadal SAM trends on the SO and relates these results to the CRFs from Chapter 3. Section 4.2 discusses the regional CRFs to greenhouse gas forcing estimated from abrupt CO_2 quadrupling experiments with CMIP5 models. Section 4.3 demonstrates that we can use the SO CRFs to SAM and GHGs to reconstruct the Southern Ocean SST trends from CMIP5 historical simulations. We then extend this linear response framework to the real SO in an attempt to understand the observed cooling around Antarctica in Section 4.4. Finally, in Section 4.5 we produce a similar analysis of the historical Southern Ocean trends but using CRFs to GHGs and ozone rather than SAM.

4.1 The Southern Ocean response to multidecadal SAM trends

We consider the preindustrial control experiments of CMIP5 models. As in Chapter 3, we regrid all GCM output to the same regular latitude-longitude grid. For each control run, we calculate an index SLP_{index} [Pa] of the Southern Annular Mode (SAM) as the zonally-averaged contrast in sea-level pressure (SLP) between 45°S and 60°S. Positive values of this index correspond to poleward intensification of the westerly winds. We also consider an alternative definition of the SAM as the first principal component ($PC1$) of sea-level pressure variability south of 20°S as in Chapter 3. The two approaches for calculating the amplitude of the Southern Annular Mode pattern produce very similar timeseries as illustrated with an example in Figure 4-2a).

Moreover, we define an index for the strength of the Southern Hemisphere surface westerlies in the control run of each model included in our ensemble. For this purpose, we compute a timeseries for the maximum of the annually averaged zonal mean zonal wind near the surface in m/s (See an example in Figure 4-2b)). However, several ensemble members (e.g., CCSM4 and CESM-CAM5) have not output the strength of the westerlies evaluated at 10 meters. For these models, we have defined a timeseries of the zonal mean zonal wind at 925 hPa (since the surface pressure in the Southern Hemisphere high latitudes is climatologically smaller than the standard sea-level value of 1013 hPa).

We compute all thirty-year linear trends in the SAM index and in the timeseries for the strength of the Southern Hemisphere westerlies. We have chosen a thirty-year length in order to relate our results to the real world, where tendencies of polar amplification have been observed continuously over the past few decades. In our analysis we consider nonoverlapping and overlapping periods alike, as this provides us with a larger sample.

Figure 4-2d) shows an example timeseries for the magnitudes of all thirty-year trends in the westerlies and a similar timeseries for the SAM index trends in one of our ensemble members, model ACCESS1-0. Across all CMIP5 GCMs we find that the multidecadal tendencies in the Southern Hemisphere near-surface zonal wind track very closely the tendencies in the annular mode. Hence, on these timescales, the strengthening of the surface westerlies in the control runs can be interpreted as a manifestation of the SAM. In all models included in our ensemble, the wind and the SAM tendencies have normal distributions (Figure 4-2c).

In our study we select multidecadal periods characterized by the strongest positive and negative tendencies in the SAM index: the 2σ tails in the distribution of all thirty-year trends within each model. We then perform a high-minus-low composite of the contemporaneous trends in Southern Ocean SST, surface salinity, potential temperature of water, surface heat fluxes, ocean heat content (OHC), and the near-surface zonal mean zonal wind. Figure 4-3 shows the composited zonal mean zonal wind trends from CMIP5 models and the historical 1980-2010 trend based on the ERA Interim reanalysis [Dee et al., 2011]. We compare our SAM-based composites with observational data from the 1979-2014 period, which is marked by a strong positive SAM trend. Drawing parallels between our CMIP5 analysis and the observational record allows us to look for the signature of SAM in the patterns of historical Southern Ocean climate change.

Across all models, the composited SST trends show a distinctive dipole pattern (Figure 4-5) in the Southern Hemisphere with warming at midlatitudes and cooling poleward of 50°S (Figure 4-4). The trends in sea-ice concentration around Antarctica are spatially correlated with the SST trends (Figure 4-6). We find sea ice growth in the regions of surface cooling and sea ice contraction in the regions which warm.

In contrast to the SST trends, the composited near-surface salinity trends (Figure 4-4) show no dipole pattern. We find small but widespread salinification south of 30°S. While the SST dipole in the SAM-based composites is reminiscent of the 1982-2014 Southern Hemisphere trends, the composited salinity trends show disagreement with observations. The last few decades are a period marked by strong Southern Ocean freshening, but our composites exhibit salinification. Thus our results imply that the historical temperature trends around Antarctica are consistent with an ocean response to a positive SAM, but the negative 1982-2014 salinity trends may not be induced by poleward intensification of the westerlies.

We then consider the zonally averaged sections of the composited potential temperature anomalies at depth. The ensemble-mean of the latter demonstrates a close connection between the anomalous wind forcing associated with SAM and the redistribution of the background heat reservoir in the ocean (Figure 4-7) during the composited 30-year periods. The observed 1979-2014 trends in zonally-averaged ocean potential temperature exhibit a similar pattern of cooling of the upper Southern Ocean and buildup of ocean heat in the Southern Hemisphere midlatitudes.

Nevertheless, the composited SST trends indicate notable differences in the Southern Ocean response to SAM across the CMIP5 ensemble even after we rescale each composite by the ensemble mean SAM trend. For example, models CanESM2, CCSM4, and CESM-CAM5 show weak cooling around Antarctica during multidecadal periods of increase in the SAM index. In contrast, models CNRM-CM5 and MRI exhibit a very strong decrease in SO SSTs in the 30-year composites. We attempt to interpret this intermodel diversity in terms of the SO step-response functions to SAM derived in Chapter 3.

Following Marshall et al. [2014], we convolve the SST step response functions to SAM $SST_{StepSAM}$ from Chapter 3 with the mean timeseries of SAM (SAM_{Compos}) from the composited 30-year periods. This convolution recovers an estimated timeseries for the composited SST anomalies $\widehat{SST}_{Compos}$:

$$\widehat{SST}_{Compos}(t) \approx \int_0^t SST_{StepSAM}(t-t') \left. \frac{dSAM_{Compos}}{dt} \right|_{t'} dt' \tag{4.1}$$

Comparing the composited SST trends (SST_{Compos}) with the estimates $\widehat{SST}_{Compos}$ from step-response convolutions allows us to test the validity of Eq. 4.1 in each CMIP5 model. Figure 4-8 shows that this approximation is applicable to modeling the Southern Ocean response to SAM in this set of coupled GCMs. Moreover, we are able to interpret the SST response to a multidecadal SAM trend as an integral quantity which smooths over the inherent fast and slow responses described in Chapter 3.

We can thus place the CRF results in the context of the observed 1979-2014 SAM trend and its impact on the spatial pattern of Southern Ocean climate change. However, in order to fully understand the historical trends in the Southern Ocean, we need to take into account the anthropogenic GHG forcing. The next section discusses a range of possible regional CRFs to greenhouse gas forcing based on experiments with the CMIP5 coupled models. We focus on the response of the Southern Ocean to global changes in the radiative forcing.

4.2 Regional CRFs to greenhouse gas forcing

The Southern Ocean CRFs to GHG forcing play a major role in our reconstruction of CMIP5 historical simulations and our analysis of the intermodel spread across the ensemble. In Marshall et al. [2014], we discuss the different regional responses to greenhouse gas forcing and focus on the asymmetry between the Antarctic and the Arctic. We have considered CMIP5 experiments where CO_2 is abruptly quadrupled relative to preindustrial values. We can think of the output from these idealized experiments as representing a range of plausible climate response functions to a step-increase in GHG forcing.

The accelerated warming in the Northern Hemisphere high latitude oceans induced by the CO_2 perturbation stands in stark contrast to the slow warming rate in the Southern Ocean (Figure 4-9). The observed historical SST trends feature an Antarctic-Arctic asymmetry similar to the one simulated in the abrupt quadrupling experiments [Marshall et al., 2014]. Therefore, these idealized experiments provide useful insights into the processes which set the large scale pattern of climate response to greenhouse gas forcing. In Marshall et al. [2014] we interpret the Antarctic-Arctic warming asymmetry in terms of the time-mean meridional overturning circulation advecting the heat anomaly in the upper ocean northward like a passive tracer. In comparison, the Southern Ocean is a region where the background circulation upwells deep water masses unmodified by greenhouse gas forcing [Marshall et al., 2013; Armour et al., 2016].

In Marshall et al. [2013] we consider the CRFs of 15 CMIP5 models where we select the two regions of the ocean: north of 50°N and south of 50°S (Figure 4-9). Here we extend our analysis to encompass a set of 20 CMIP5 models, the same set of GCMs as in Chapter 3. Note that models CESM-CAM5, CMCC-CM, and NorESM1-ME have not made available any abrupt CO_2 quadrupling simulations.

In order to be consistent with the Southern Ocean CRFs to SAM derived in Chapter 3, we now consider SST response to GHG forcing averaged over the latitude band between 55°S and 70°S denoted by CRF_{GHG} (Figure 4-10). In the following section we use the CRFs to SAM and the CRFs to GHG to recover the Southern Ocean SST trends from CMIP5 historical simulations. The TOA radiative forcing in these experiments is dominated by GHG and the SAM trends are influenced by stratospheric ozone depletion.

4.3 Understanding the Southern Ocean SST trends in CMIP5 historical simulations

In order to understand why CMIP5 GCMs are generally unable to simulate the 1979-2014 Southern Ocean cooling trends, we analyze the forced response mechanisms in the models' historical simulations extended until 2014 under the RCP8.5 scenario. We take into account both the trend in the TOA radiative forcing and the model-specific SAM trends. We consider the separate and combined effects that both sources of forcing exert on the Southern Ocean.

We first analyze the contribution of SAM to the simulated 1979-2014 Southern Ocean SST trends. For each of the CMIP5 historical simulations and preindustrial control experiments, we calculate an annual mean SAM index SLP_{index} defined as the zonally-averaged sea level pressure (SLP) difference [Pa] between 45°S and 60°S. This definition of the SAM allows for an easy comparison between the 1979-2014 SAM trends in simulations and observations or reanalysis. Moreover, across all models in our ensemble, the 45°S-60°S SLP difference SLP_{index} tracks very well the first principal component ($PC1$) of SLP variability south of 20°S (the definition of SAM used in Chapter 3).

In fact, if we compare how SLP_{index} projects onto $PC1$ in the long preindustrial control experiments, we find that the ratios

$$r_{SAM} = \frac{SLP_{index}}{PC1} \tag{4.2}$$

are very similar across CMIP5 models. We rescale the CRFs from Chapter 3, which were computed as the response CRF_{PC1} to the ensemble-mean of the $PC1$ standard deviations $\overline{\sigma_{PC1}}^{Ens}$, to obtain

$$CRF_{SLPindex} = \frac{CRF_{PC1}}{\overline{\sigma_{PC1}}^{Ens} r_{SAM}}, \tag{4.3}$$

where $CRF_{SLPindex}$ [°C/Pa] is now the expected Southern Ocean SST response to a step-increase in the SLP difference SLP_{index} between 45°S and 60°S. Figure 4-11 shows $CRF_{SLPindex}$, the rescaled SO SST CRFs to SAM in each CMIP5 model.

We then convolve the 1979-2014 linear trend in the SLP_{index} from each CMIP5 historical simulation with the corresponding model-specific response function $CRF_{SLPindex}$ similarly to Eq. 4.1 to obtain estimates for the SAM-induced SO SST anomaly $\widehat{SST}_{SAM}(t)$ in each historical simulation. We denote the 1979-2014 trends in $\widehat{SST}_{SAM}(t)$ by $\widehat{SST}_{TrendSAM}$ [°C/decade].

We compare the estimates for the SAM-induced SST trends in the models $\widehat{SST}_{TrendSAM}$ with the actual simulated SO trends for the 1979-2014 period (4-12a)). We see that SAM can explain a large part of the intermodel spread in the SO climate change across the CMIP5 historical experiments. However, the trends in $\widehat{SST}_{SAM}(t)$ consistently underestimate the simulated SO SST anomalies. The ensemble mean $\widehat{SST}_{TrendSAM}$ trend is negatively offset with respect to the ensemble mean SO SST trends between 1979 and 2014. This should not come as a surprise, as the SAM is not the only source of forcing on the SO in the historical simulations. Perturbations in the top-of-the-atmosphere radiative forcing play an important role in driving regional and global climate change as modeled in the CMIP5 GCMs.

Since the industrial revolution, the top-of-the-atmosphere radiative forcing has been overwhelmingly dominated by anthropogenic greenhouse gas emissions. Major volcanic eruptions have exerted only an episodic short-lived cooling effect superimposed on the long-term warming trend. However, anthropogenic aerosols and changes in land use have also contributed to the total globally averaged radiative forcing represented in the models' historical simulations.

The local effect of aerosols and land use is expected to be larger over the Northern Hemisphere, where most of the earth's continental cover, most of the human population, and most sources of industrial pollution are concentrated. The non-local effect of anthropogenic aerosols and land use on Southern Ocean climate is therefore unclear and its representation may be very model dependent. Here we neglect these contributions to the TOA forcing whose effect on the Antarctic region may be more limited. We also neglect the local TOA radiative forcing due to stratospheric ozone depletion (we separately consider the SAM-like effect of the ozone hole on atmospheric and ocean dynamics). We focus instead on the radiative impact of well-mixed greenhouse gases. As a simplification, we assume that the concentration of anthropogenic GHGs in the CMIP5 historical simulations grows exponentially from a 280 ppm to a 480 ppm CO_2-equivalent between 1855 and 2014 (160 years). This corresponds to a linear increase in radiative forcing, as the latter varies logarithmically with the CO_2 concentration. We treat model-specific deviations from this trend as error terms in our analysis.

To obtain an estimate of the SO SST anomalies SST_{RAD} induced by the idealized trend in GHG-induced TOA radiative forcing, we convolve the latter with the Southern Ocean CRFs to GHG from Section 3. These SST step response functions are based on CMIP5 numerical experiments where the preindustrial CO_2 concentration of 280 ppm is abruptly increased to 4x280 ppm. Thus before we perform our convolution analysis, we rescale the historical radiative forcing trend by the forcing which corresponds to abrupt CO_2 quadrupling:

$$\begin{aligned} F_{GHGtrend} &= \left(\frac{ln(480) - ln(280)}{ln(4 \times 280) - ln(280)}\right) \frac{1}{160 years} \\ &= \left(\frac{ln(480/280)}{ln(4)}\right) \frac{1}{160 years} \\ &\approx 2.43 \times 10^{-3} \left[\frac{1}{years}\right], \end{aligned} \tag{4.4}$$

where $F_{GHGtrend}$ [1/years] is the rescaled idealized trend in TOA radiative forcing.

Thus SST_{RAD} [°C] can be approximated as

$$\widehat{SST}_{RAD}(t) \approx F_{GHGtrend} \int_0^t CRF_{GHG}(t-t')dt' \tag{4.5}$$

We compare the 1979-2014 linear trends in $\widehat{SST}_{RAD}(t)$, $\widehat{SST}_{TrendRAD}$ [°C/decade] against the SO SST trends in the actual historical simulations (4-12b)). We see a smaller intermodel spread in the SST_{RAD} than in the SST_{SAM} trends (Figure 4-12a) and b)). Even though GHG forcing alone reproduces the ensemble mean, our SST_{RAD} convolutions by themselves cannot explain well the large differences in the 1979-2014 SO SST trends across the CMIP5 historical simulations.

This motivates us to combine the results of the SAM and GHG convolutions and simultaneously account for both of these major sources of forcing on the Southern Ocean. However, part of the trend in the SAM index is itself driven by GHG forcing [Solomon et al., 2015]. That is why we cannot sum the SAM and GHG convolutions linearly without subtracting an interaction term representing the SST anomaly induced by the component of the SAM trend that is attributable to GHG forcing.

We turn to the CMIP5 abrupt CO_2 quadrupling experiments to estimate the effect of GHG forcing on the SAM. For each quadrupling experiment we calculate $SAM_{4\times CO2}(t)$ [Pa], the anomaly in SLP_{index} relative to the corresponding preindustrial control run (Figure 4-13). The $SAM_{4\times CO2}$ indices constitute CRFs of SAM to GHG forcing. We convolve these CRFs with the idealized trends in GHG TOA radiative forcing to obtain estimates for the GHG-induced anomaly in the SAM index (SAM_{GHG} [Pa]) of each CMIP5 historical simulation:

$$\widehat{SAM}_{GHG}(t) \approx F_{GHGtrend} \int_0^t SAM_{4\times CO2}(t-t')dt' \tag{4.6}$$

and we further estimate the linear trend in $\widehat{SAM}_{GHG}(t)$ over the 1979-2014 period: $\widehat{SAM}_{TrendGHG}$ [Pa/year]. The trend $\widehat{SAM}_{TrendGHG}$ is in turn expected to induce an SO SST anomaly [°C],

$$\widehat{SST}_{Inter}(t) \approx \widehat{SAM}_{TrendGHG} \int_0^t CRF_{SLPindex}(t-t')dt', \tag{4.7}$$

and we denote the corresponding 1979-2014 trend in $\widehat{SST}_{Inter}$ by $\widehat{SST}_{TrendInter}$ [°C/year].

Finally, we combine $\widehat{SST}_{TrendSAM}$ and $\widehat{SST}_{TrendRAD}$, and we subtract the trend in the GHG-SAM interaction term $\widehat{SST}_{TrendInter}$ to obtain estimates for the anomalous 1979-2014 SO SST trend due to the combined effect of SAM and GHG forcing in the historical simulations:

$$\widehat{SST}_{TrendCombined} = \widehat{SST}_{TrendSAM} + \widehat{SST}_{TrendRAD} - \widehat{SST}_{TrendInter}, \tag{4.8}$$

where $\widehat{SST}_{TrendCombined}$ is our estimate in °C/decade. Taking into account both the SAM and GHG forcing allows us to better reproduce the SO climate change in each CMIP5 model (4-12c)). We see that our $\widehat{SST}_{TrendCombined}$ estimates recover very well both the ensemble mean response, the responses of individual GCMs, and the intermodel variability.

Our reconstruction allows us to break down the simulated multidecadal SO SST trends into GHG and SAM contributions (Figure 4-12). As expected, in all models the TOA radiative forcing contributes to warming around Antarctica. On the other hand, the sign of the SAM contribution to the SST trends differs across models. In most GCMs positive 1979-2014 SAM tendencies induce SO cooling anomalies.

However, the CMIP5 models also differ among each other in the simulated historical evolution of the SAM itself. In the following section we emphasize that reproducing the historical SAM anomalies is an essential prerequisite for the successful simulation of the 1979-2011 SO SST trends.

4.4 Interpreting the observed Southern Ocean SST trends using SAM and GHG CRFs

So far we have focused our analysis on understanding the SO SST trends in the historical simulations and explaining the differences across the ensemble of GCMs. We now attempt to find why most CMIP5 models do not reproduce the observed 1979-2014 SO cooling and instead predict much weaker trends or warming (Figure

4-14. We seek to identify the main source of bias responsible for this discrepancy.

We compare the 1979-2014 trend of the SAM index (SLP_{index} [Pa]) in the CMIP5 simulations, in the ERA Interim reanalysis, and in the HadSLP2r observational dataset (*Allan and Ansell*, 2006). We point out that there is large disagreement among the SAM trends simulated by models. There are also large differences between the CMIP5 models and the observationally constrained products. However, it is noteworthy that the HadSLP2r gridded observations and the ERA Interim reanalysis do not agree with each other on the magnitude of the SLP_{index} anomalies. The HadSLP2r dataset suggests a SAM trend which is 3 times larger than the trend in the ERA Interim output.

The HadSLP2r dataset is considered a more reliable record of historical changes in Southern Hemisphere extratropical sea-level pressure than reanalysis products [Swart et al., 2015]. Hence we use the gridded observations to evaluate how biased the CMIP5 historical SAM anomalies are. We note that relative to HadSLP2r almost all GCM simulations underestimate the 1979-2014 positive SAM trend.

We then evaluate the impact of this SAM bias on the ability of CMIP5 models to reproduce the SO SST trends. We convolve each $CRF_{SLPindex}$ with the SAM trend based on the HadSLP2r observations to obtain a range of estimates for the component of the SO SST trend induced by the observed SAM anomalies, $SST_{TrendObsSAM}$ [°C/decade]. We then perform a calculation similar to Eq. 4.8:

$$\widehat{SST}_{TrendSO} = \widehat{SST}_{TrendObsSAM} + \widehat{SST}_{TrendRAD} - \widehat{SST}_{TrendInter}, \tag{4.9}$$

where $\widehat{SST}_{TrendSO}$ [°C/decade] is now an estimate of how the CMIP5 SO SSTs would evolve if the models simulated a more realistic SAM between 1979 and 2014. We compare $\widehat{SST}_{TrendSO}$ against the SO SST trends in the CMIP5 experiments and against our reconstructions $\widehat{SST}_{TrendCombined}$ (Figure 4-15). We estimate that more than half of the models in our ensemble would exhibit stronger SO cooling under a realistic evolution of the SAM. Using SLP_{index} based on the HadSLP2r dataset produces an ensemble mean response much closer to the observed SO SST trend than the ensemble mean of the original historical simulations. However, several models, such as CanESM2 and CCSM4, are expected to show stronger SO warming under realistic SAM. The different behavior of these GCMs is discussed in Chapter 3 and may have to do with biases in their climatology of the mean SO thermal stratification. Notwithstanding these notable exceptions, our results demonstrate that the SAM in the historical simulations may explain a large fraction of the SO warming bias seen in most CMIP5 models.

4.5 Interpreting the observed Southern Ocean SST trends using ozone and GHG CRFs

We have demonstrated that convolving a plausible combination of SAM and GHG CRFs with the observed SAM and GHG trends allows us to better reproduce the Southern Ocean cooling observed since 1979. The historical timeseries of the SAM index includes both unforced variability and an anthropogenically forced signal due to ozone depletion. Changes in stratospheric ozone concentration trigger an atmospheric response which projects on the SAM pattern. However, the Antarctic ozone hole exhibits strong seasonality with maximum depletion in the early austral spring. This seasonality has not been taken into account in our CRFs based on the annual-mean SAM. We seek to estimate the contribution of two anthropogenic factors: seasonally variable stratospheric ozone loss and GHG forcing, to the historical Southern Ocean SST trends. That is why in Marshall et al. [2014] we consider a Southern Ocean CRF to ozone depletion rather than a CRF to SAM.

Model-based CRFs to stratospheric ozone depletion are available from Ferreira et al. [2015] and are derived from an ensemble of numerical experiments in which an idealized abrupt depletion of ozone is applied to the coupled MITgcm and CCSM3.5 models. The MITgcm is used in an aquaplanet configuration with simplified bathymetry: two meridional land strips extend from the north pole to 35°S and delimitate a small Atlantic-Arctic-like basin and a large Indo-Pacific-like basin connected with each other via a circumpolar ocean in the Southern Hemisphere. The ozone forcing in the MITgcm is represented as a perturbation in the stratospheric shortwave absorption. In order to mimic the seasonality of the real ozone hole, the idealized ozone depletion in the MITgcm is introduced as a negative step function whose amplitude varies with a 12 month period. CCSM3.5, on the other hand, is a fully coupled model which computes stratospheric ozone and has realistic ocean bathymetry. The GCM shares a similar genealogy to the more recent CCSM4 model whose SAM CRF is analyzed in Chapter 3. The abrupt ozone depletion in CCSM3.5 is represented explicitly and its magnitude is comparable with historical ozone changes.

In Marshall et al. [2014] we have also considered an abrupt SAM perturbation experiment with an ocean-only version of the MITgcm which has realistic bathymetry. The forcing in this case is applied as a surface wind-stress anomaly. The perturbation has a SAM-like spatial pattern whose magnitude varies seasonally between zero and 1σ SAM mimicking the seasonality of the ozone-induced wind stress anomalies.

Since the idealized ozone depletion gives rise to a SAM-like atmospheric pattern, we expect that the corresponding Southern Ocean SST response will be similar to the SAM CRFs discussed in Chapter 3. Indeed we see a two-timescale response in both CCSM3.5 and the MITgcm (Figure 4-16). The models show initial cooling of the Southern Ocean followed by warming. However, both the magnitude of the fast cooling response and the slow warming rate differ between the two GCMs. These intermodel differences are analyzed in Ferreira et al. [2014] and can be attributed in part to the models' climatological stratification but also to air-sea heat fluxes.

We have constructed a range of plausible idealized ozone CRFs which span the curves based on the MITgcm and CCSM3.5. Each of these idealized constructed CRFs can be expressed as a sum of two exponential terms: a fast decaying negative term and a slowly decaying positive term reflecting the two-timescale nature of the response [Marshall et al., 2014].

The historical timeseries of ozone forcing itself also shows a nonmonotonic evolution over recent decades (Figure 4-17a)). Stratospheric ozone concentration [DU] declines rapidly after the 1970s due to CFC emissions and has been gradually recovering since the end of the 1990s as a result of international regulations designed to protect the ozone layer [Douglas et al., 2014]. Thus, when we convolve the Southern Ocean CRF to ozone with the historical forcing (analogously to Eq. 4.1), we obtain an estimate for the ozone-induced SST anomaly which evolves in a nontrivial fashion. The convolution is characterized by a cooling trend that spans the last few decades of the 20th century. This is followed by a gradual warming. The projected partial recovery of ozone is expected to give rise to a Southern Ocean cooling trend, once again, beyond the year 2060.

The estimated evolution of the ozone-induced Southern Ocean SST anomalies can be contrasted against the response to the top-of-the-atmosphere (TOA) radiative forcing. The historical timeseries of radiative forcing has been dominated by the continuous increase of anthropogenic greenhouse gas emissions (Figure 4-17b)). Only volcanic eruptions cause sporadic negative excursions in the TOA forcing signal. Thus the convolution of the regional CRFs to GHG (4-9) with the timeseries of TOA forcing yields estimated warming responses which grow persistently throughout the 20th and 21st centuries and beyond.

It is important to note that the estimated Southern Ocean response to TOA radiative forcing is much more gradual compared to the fast warming rate in the Northern Hemisphere high latitude oceans. On the other hand, the Northern Hemisphere response is marked by more rapid fluctuations due to major volcanic eruptions, while the Southern Ocean SST anomalies evolve more smoothly and integrate over such short-lived radiative perturbations.

We assume that the Northern Hemisphere high latitude region is subjected to the TOA radiative forcing, while the Southern Ocean is exposed to an additional source of forcing due to ozone depletion and recovery. Hence we combine the estimated ozone-induced SST anomalies with the SST anomalies due to TOA radiative forcing to obtain a more comprehensive timeseries of anthropogenic Southern Ocean climate change (Figure 4-17b)). Our combined estimates recover qualitatively both the historical warming trend in the Northern Hemisphere and the observed transient cooling trends around Antarctica.

Motivated by these convolution results, we suggest that a large part of the Southern Ocean cooling trends over the past few decades may be attributed to stratospheric ozone forcing which gives rise to a SAM-like atmospheric pattern. However, we project that this anomalous SST decrease is transient. According to our results, we expect to see stronger Southern Ocean warming trends in the 21st century.

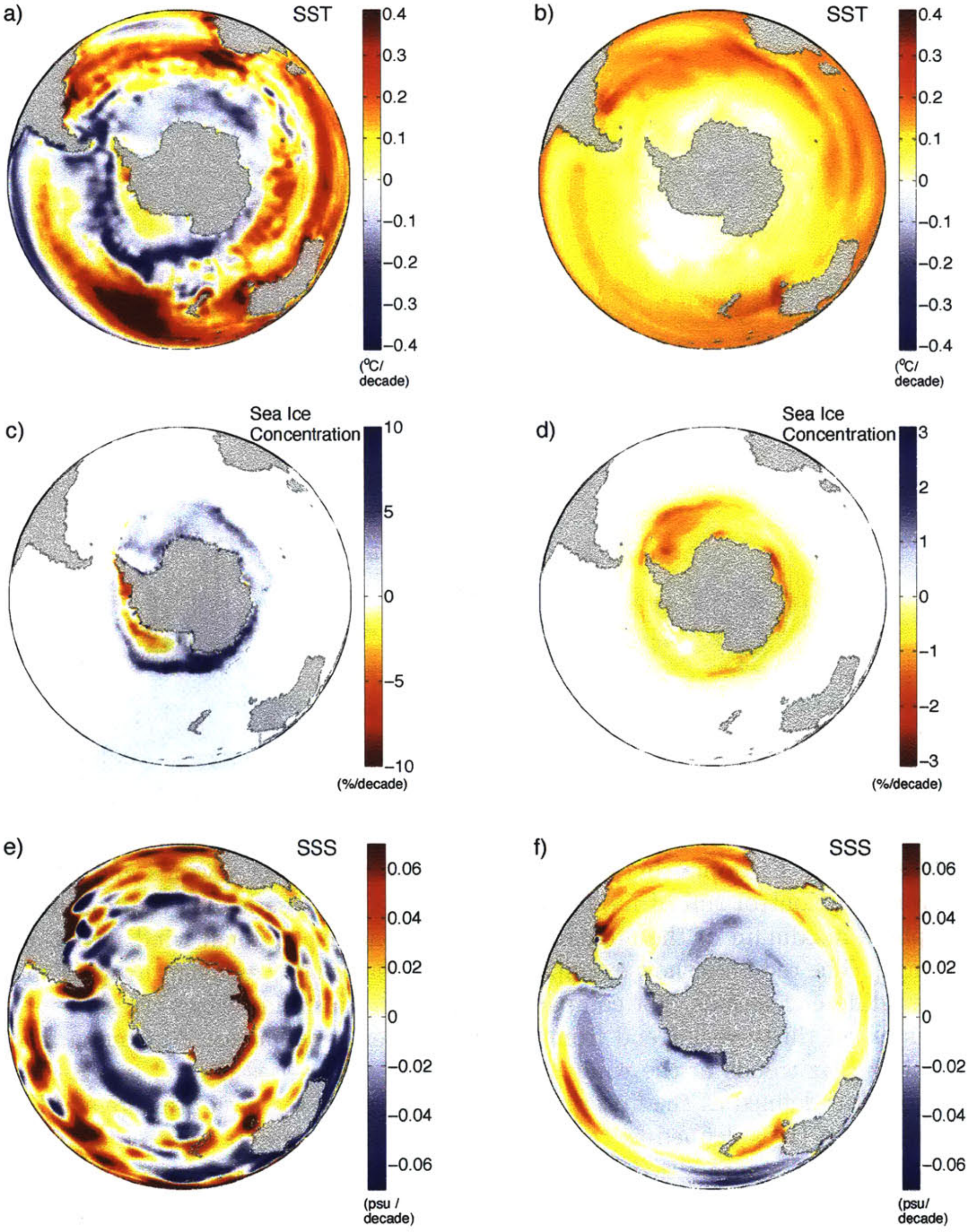
a)
SST
0.4
0.3
0.2
0.1
0
−0.1
−0.2
−0.3
−0.4
(°C/ decade)
b)
SST
0.4
0.3
0.2
0.1
0
−0.1
−0.2
−0.3
−0.4
(°C/ decade)
c)
Sea Ice Concentration
10
5
0
−5
−10
(%/decade)
d)
Sea Ice Concentration
3
2
1
0
−1
−2
−3
(%/decade)
e)
SSS
0.06
0.04
0.02
0
−0.02
−0.04
−0.06
(psu / decade)
f)
SSS
0.06
0.04
0.02
0
−0.02
−0.04
−0.06
(psu/ decade)

Figure 4-1: a) Observed SST trends [°C/decade] for the 1982-2014 period based on the NOAA Reynolds Optimum Interpolation Dataset [Reynolds et al., 2002], which begins in 1982; b) Numerical simulations of the SST trends [°C/decade] for the 1979-2014 period: an ensemble mean of CMIP5 historical experiments extended under the rcp8.5 scenario; c) Same as a) but for 1982-2014 trends in sea ice concentration [%/decade] from Reynolds et al. [2002]; d) Same as b) but showing sea ice trends [%/decade]; e) Observed trends in the sea surface salinity (SSS) [psu/decade] for the 1979-2013 period based on the HadEN4 Dataset [Good et al., 2013]; f) Same as b) and d) but showing sea surface salinity (SSS) trends [psu/decade].

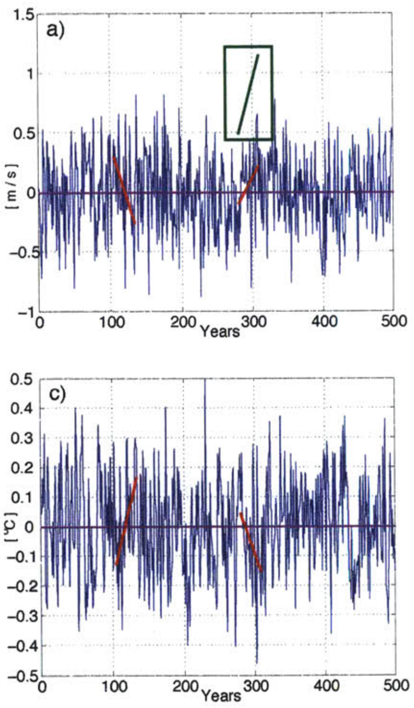

Figure 4-2: Example timeseries and trends in the westerly winds and SAM indices from the control run of model ACCESS1-0: a) Timeseries for the Southern Hemisphere maximum of the annually averaged zonal mean zonal wind near the surface [m/s]. The red lines show examples of thirty-year linear trends in the wind speed over two different periods. For comparison, the inset green line shows the slope of the last historical thirty-year trend from the ERA Interim reanalysis; b) Comparison of the thirty-year trends in the wind index from [a)] (timeseries II) and two SAM indices: index I is defined as the first principal component of sea level pressure south of 20°S, and index III is defined as the contrast in sea level pressure between 45°S and 60°S. Each index is normalized by its standard deviation; c) Timeseries for the annually averaged SST anomaly between 55° and 70°S. The red lines show the linear trends in SST over the same thirty-year periods as the ones highlighted with red lines in panel a) above; d) Distribution of all thirty-year westerly wind trends [m/s/year] based on the timeseries shown in [a)].

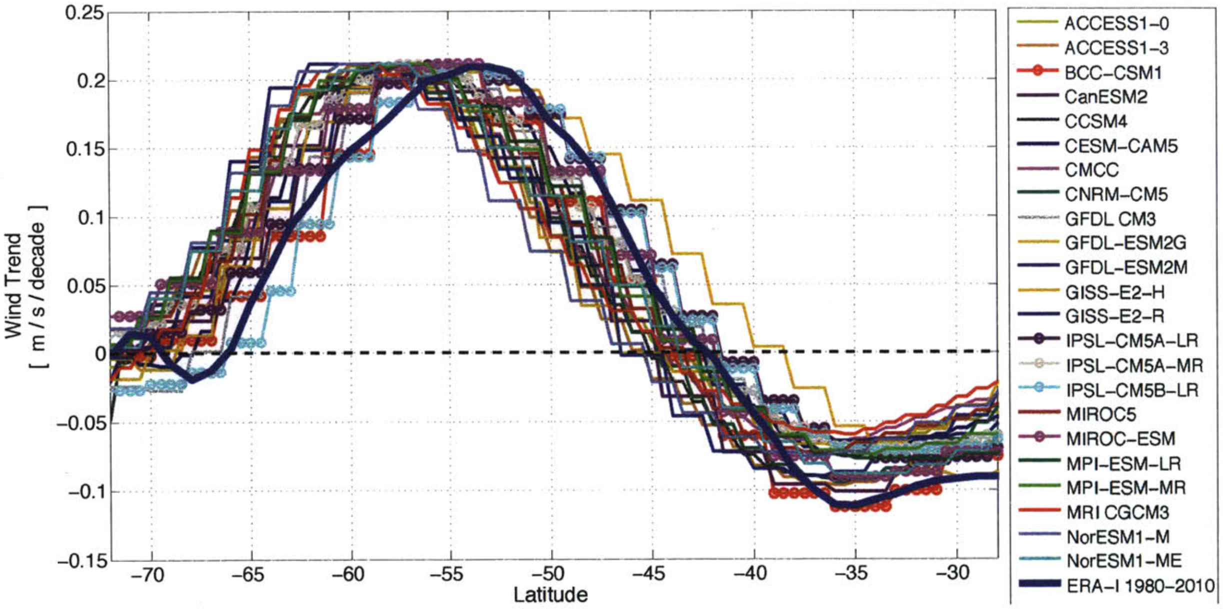

Figure 4-3: Composited 30-year trends in zonally-averaged zonal wind at the surface [m/s/decade] from periods of 2σ SAM trends in the CMIP5 control runs. The result for each ensemble member is rescaled by a ratio between the amplitude of the zonally averaged 1980-2010 westerly wind trend from ERA-Interim and the amplitude of the westerly wind trend in each CMIP5 model composite.

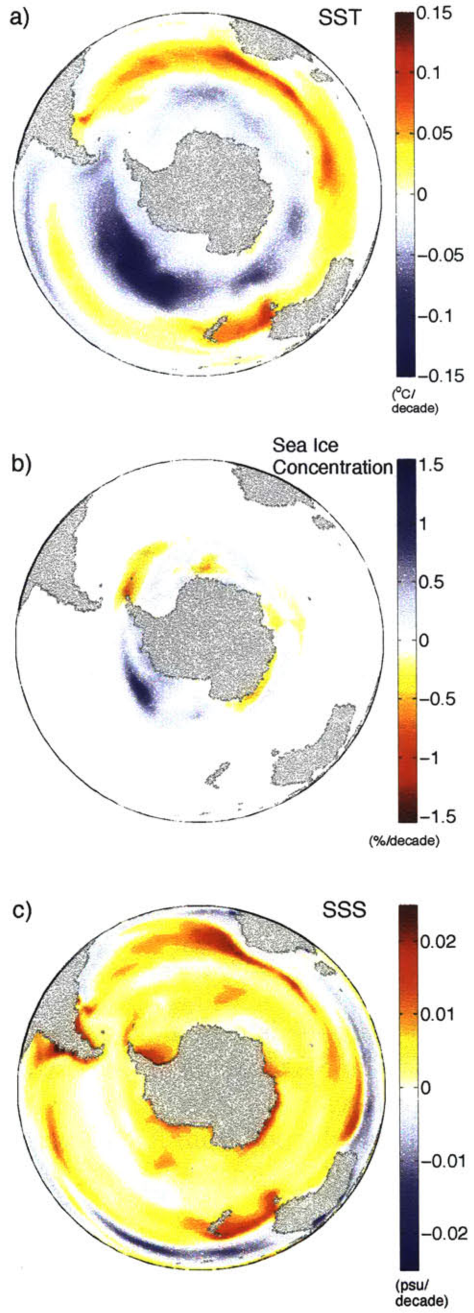
a)
SST
0.15
0.1
0.05
0
−0.05
−0.1
−0.15
(°C/ decade)
b)
Sea Ice Concentration
1.5
1
0.5
0
−0.5
−1
−1.5
(%/decade)
c)
SSS
0.02
0.01
0
−0.01
−0.02
(psu/ decade)

Figure 4-4: Ensemble mean of 23 models. The results for each ensemble member are rescaled by a ratio between the amplitude of the zonally averaged 1980-2010 westerly wind trend from ERA-Interim and the amplitude of the westerly wind trend in each CMIP5 model composite. a) Composited 30-year SST trends [°C/decade] from periods of 2σ SAM trends in the CMIP5 control runs; b) Same as in a) but for sea ice concentration trends [%/decade]; c) Same as in a) and b) but for surface salinity trends [psu/decade].

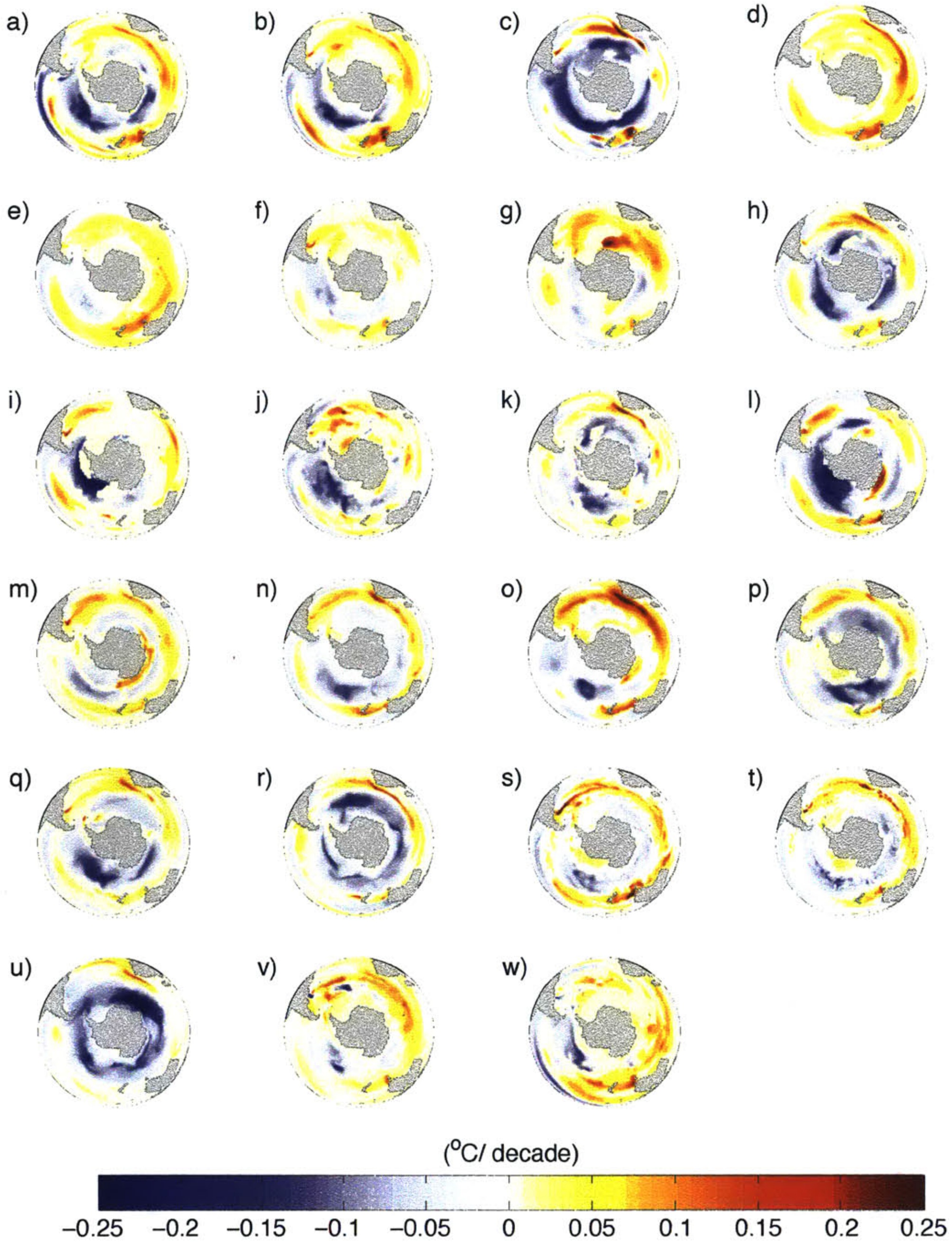

Figure 4-5: Composited 30-year SST trends [°C/decade] from periods of 2σ SAM trends in the CMIP5 control runs of models: a) ACCESS1-0; b) ACCESS1-3; c) BCC-CSM1; d) CanESM2; e) CCSM4; f) CESM-CAM5; g) CMCC-CM; h) CNRM-CM5; i) GFDL CM3; j) GFDL-ESM2G; k) GFDL-ESM2M; l) GISS-E2-H; m) GISS-E2-R; n) IPSL-CM5A-LR; o) IPSL-CM5A-MR; p) IPSL-CM5B-LR; q) MIROC5; r) MIROC-ESM; s) MPI-ESM-LR; t) MPI-ESM-MR; u) MRI-CGCM3; v) NorESM1-M; w) NorESM1-ME. The result for each ensemble member is rescaled by a ratio between the amplitude of the zonally averaged 1980-2010 westerly wind trend from ERA-Interim and the amplitude of the westerly wind trend in each CMIP5 model composite. We have shown only trends that are significant at the 95% confidence level.

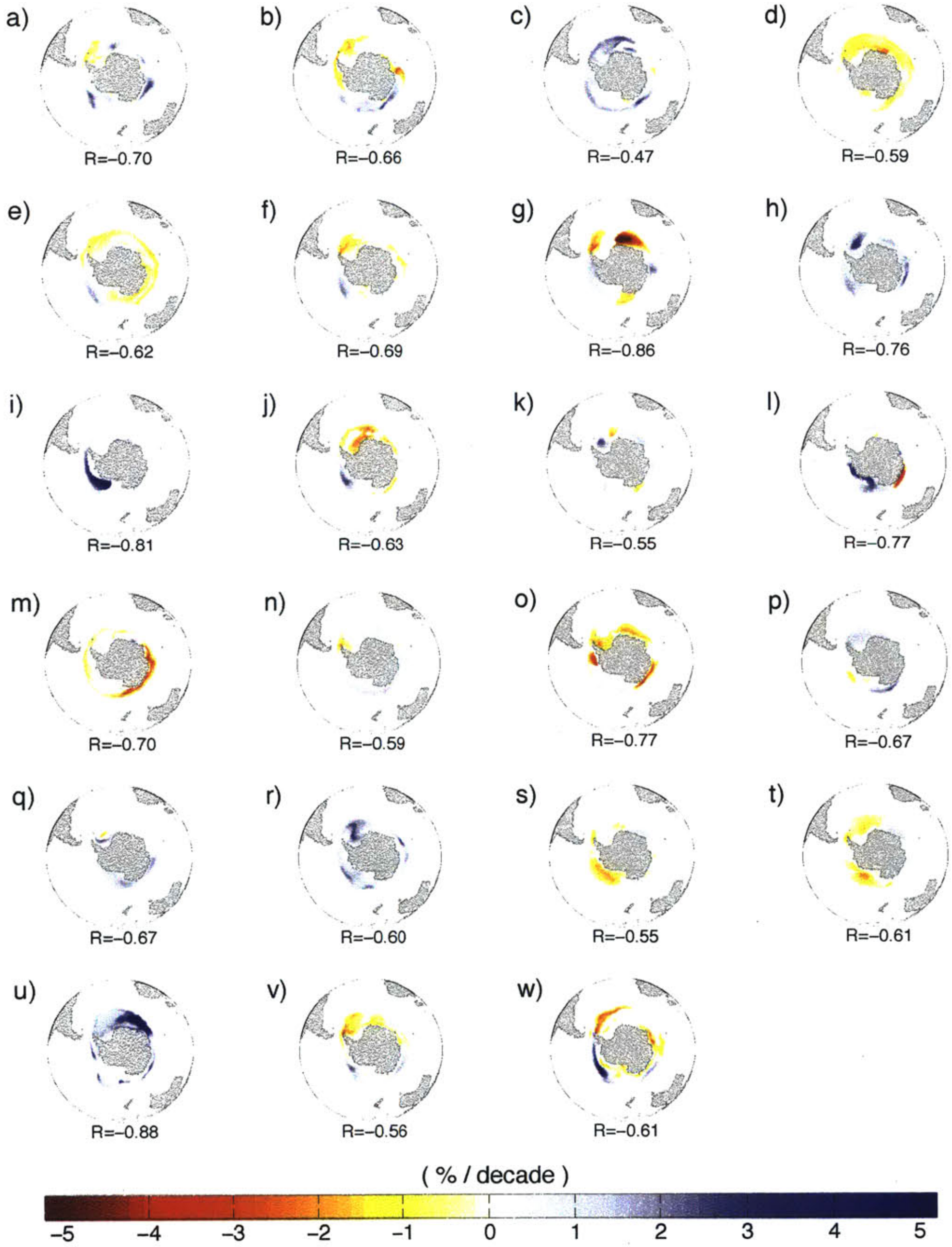
a)
R=−0.70
b)
R=−0.66
c)
R=−0.47
d)
R=−0.59
e)
R=−0.62
f)
R=−0.69
g)
R=−0.86
h)
R=−0.76
i)
R=−0.81
j)
R=−0.63
k)
R=−0.55
l)
R=−0.77
m)
R=−0.70
n)
R=−0.59
o)
R=−0.77
p)
R=−0.67
q)
R=−0.67
r)
R=−0.60
s)
R=−0.55
t)
R=−0.61
u)
R=−0.88
v)
R=−0.56
w)
R=−0.61
(% / decade)
−5
−4
−3
−2
−1
0
1
2
3
4
5

Figure 4-6: Composited 30-year trends in sea ice concentration [%/decade] from periods of 2σ SAM trends in the CMIP5 control runs of models: a) ACCESS1-0; b) ACCESS1-3; c) BCC-CSM1; d) CanESM2; e) CCSM4; f) CESM-CAM5; g) CMCC-CM; h) CNRM-CM5; i) GFDL CM3; j) GFDL-ESM2G; k) GFDL-ESM2M; l) GISS-E2-H; m) GISS-E2-R; n) IPSL-CM5A-LR; o) IPSL-CM5A-MR; p) IPSL-CM5B-LR; q) MIROC5; r) MIROC-ESM; s) MPI-ESM-LR; t) MPI-ESM-MR; u) MRI-CGCM3; v) NorESM1-M; w) NorESM1-ME. The result for each ensemble member is rescaled by a ratio between the amplitude of the zonally averaged 1980-2010 westerly wind trend from ERA-Interim and the amplitude of the westerly wind trend in each CMIP5 model composite. We have shown only trends that are significant at the 95% confidence level. For each model we have listed the correlation between the composited sea ice trends and the composited SST trends from Figure 4-5.

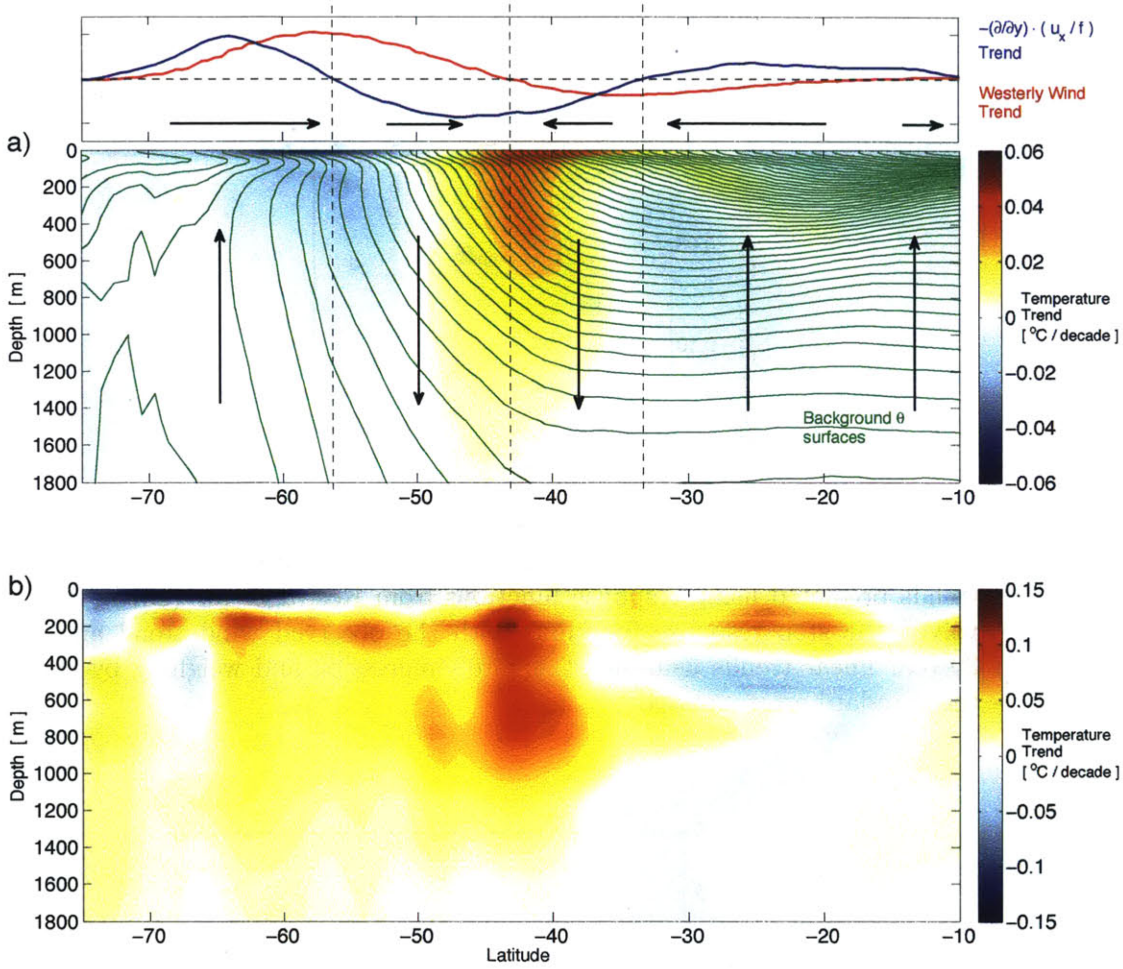

Figure 4-7: a) Ensemble-mean composites from periods of 2σ SAM trends in the CMIP5 control runs. Bottom panel: Composited 30-year trends in zonally-averaged ocean potential temperature at depth [°C/decade] from periods of 2σ SAM trends in the CMIP5 control runs. Ensemble mean of 23 models. The result for each ensemble member is rescaled by a ratio between the composited trends and the reanalyzed ERA-Interim trends in the zonally averaged surface westerlies. Green contours spaced 0.5°C apart indicate zonally averaged time-mean potential temperature in the ensemble mean. Schematic arrows and dashed lines mark the latitude ranges where we expect anomalous horizontal and vertical Ekman transport according to the sign of the wind trends and wind curl trends shown in red and blue in the top panel; b) Observed 30-year trends in zonally averaged ocean potential temperature [°C/decade] for the 1979-2013 period based on the HadEN4 Dataset [Good et al., 2013].

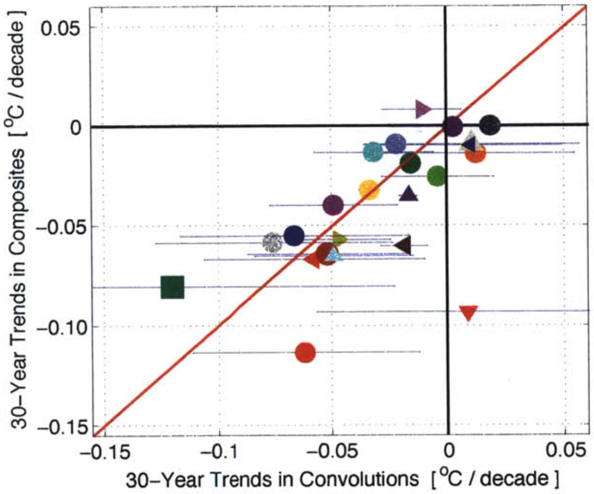

Figure 4-8: Composited SST trends 55-70°S from Figure 5, compared with the SST trends predicted using response functions from Kostov et al. (2015). We have convolved the step response functions with the observed wind trend and then fitted 30-year linear trends using least square's regression and weighing by the inverse of the standard error squared.

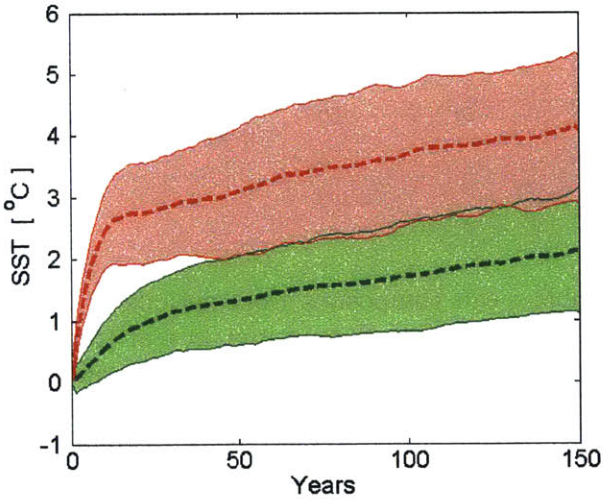

Figure 4-9: Regional CRFs [°C] to abrupt CO_2 quadrupling from Marshall et al. [2014]. Red curves show the SST response in the Northern Hemisphere north of 50°N, and the green curves show the response in the Southern Ocean south of 50°S. The thick line indicates the ensemble mean of CMIP5 models, and the shaded envelopes mark one standard deviation of the ensemble spread. Layout to be modified.

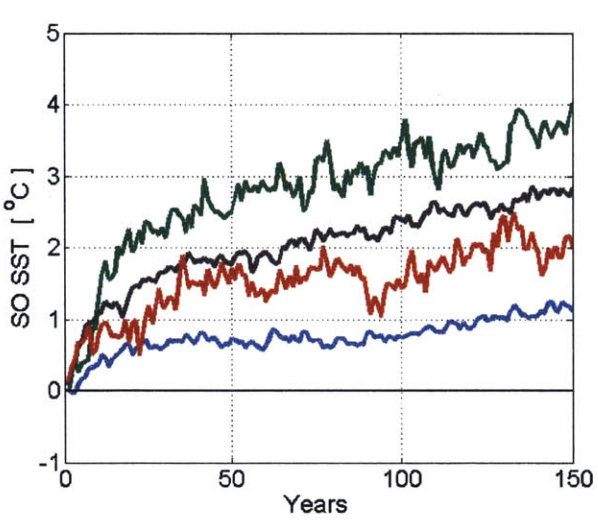

Figure 4-10: A sample of SST response functions [°C] for the Southern Ocean south of 55°S in 4 CMIP5 models forced with abrupt CO_2 quadrupling.

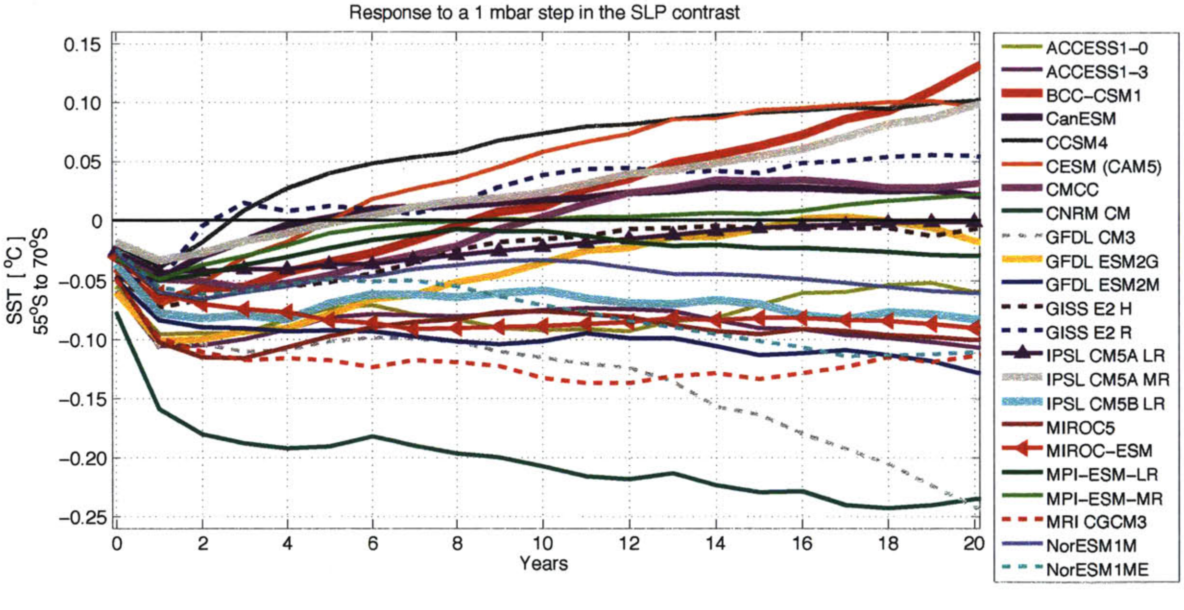

Figure 4-11: SO SST response functions [°C] based on the analysis in Chapter 3 but rescaled to represent the response to a 1 mbar step increase in the SLP_{index} SAM index. Different colors denote CMIP5 models.

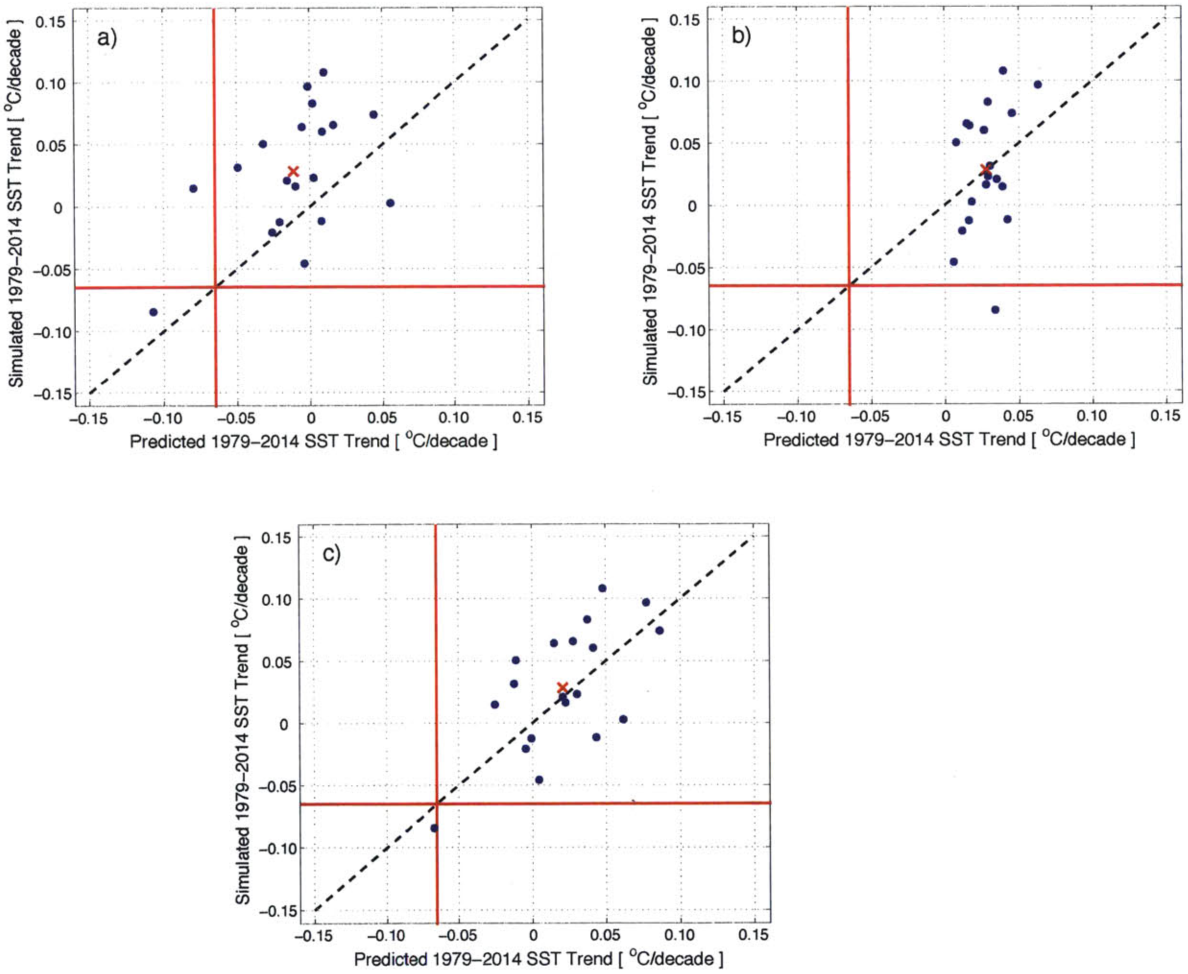

Figure 4-12: Comparison of the simulated 1979-2014 SO SST trends [°C/decade] in CMIP5 and our reconstructions using a) convolutions of the SAM CRFs from Figure 4-11, b) convolutions of GHG CRFs such as the examples in Figure 4-9, c) the combination of SAM CRF convolutions and GHG CRF convolutions minus impact of the estimated SAM trend due to GHG forcing. (The effect of GHGs on SAM is shown in Figure 4-13.) A red cross denotes the ensemble mean of the simulations and reconstructions.

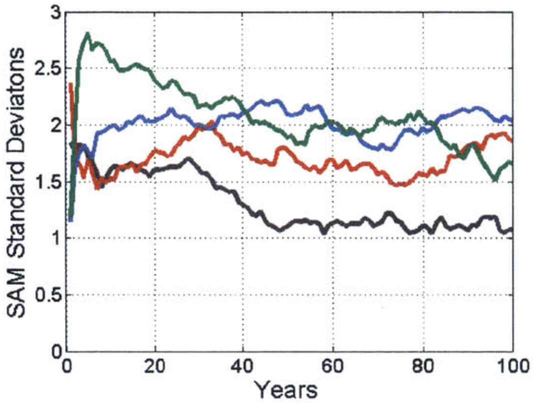

Figure 4-13: A sample of response functions of the SAM index (SLP_{index}) in 4 CMIP5 models forced with abrupt CO_2 quadrupling. The indices are smoothed with a 25-year running mean and are normalized by the index standard deviations estimated from the preindustrial control simulation of each model.

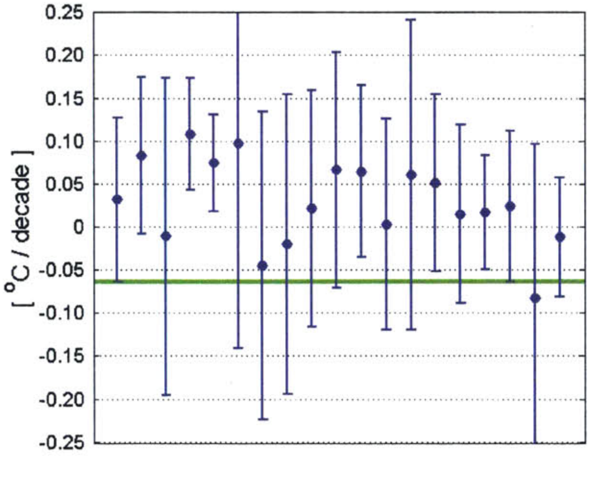

Figure 4-14: CMIP5 SO warming bias in the CMIP5 simulations: Circular markers denote the 1979-2014 SO SST trends [°C/decade] in CMIP5 historical simulations extended under the RCP8.5 scenario. Vertical lines indicate two standard deviations of the models' natural variability in the SO SST trends of the preindustrial control experiments. The green horizontal line shows the observed 1982-2014 SO SST trend [°C/decade] according to the NOAA Reynolds Optimum Interpolation dataset.

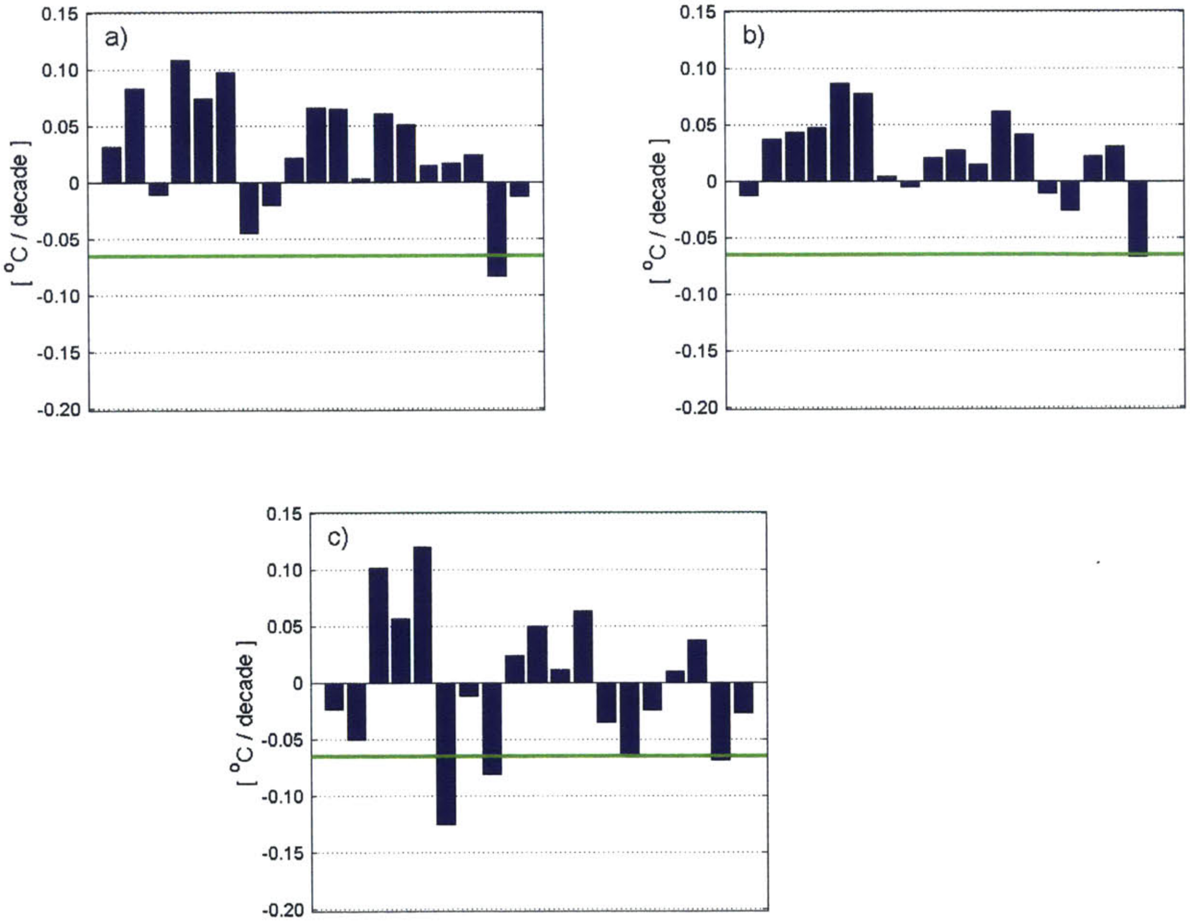

Figure 4-15: Understanding the CMIP5 SO warming bias: The green horizontal lines in each subfigure show the observed 1982-2014 SO SST trend [°C/decade] according to the NOAA Reynolds Optimum Interpolation dataset. a) Vertical bars denote the 1979-2014 SO SST trends [°C/decade] in CMIP5 historical simulations extended under the RCP8.5 scenario; b) Vertical bars denote the 1979-2014 SO SST trends [°C/decade] in our reconstructions of each CMIP5 simulation; c) Vertical bars denote the 1979-2014 SO SST trends [°C/decade] we obtain after we convolve the GHG and SAM CRFs with observationally-based forcing trends. The SAM forcing trend used for this reconstruction is based on the HadSLP2r dataset.

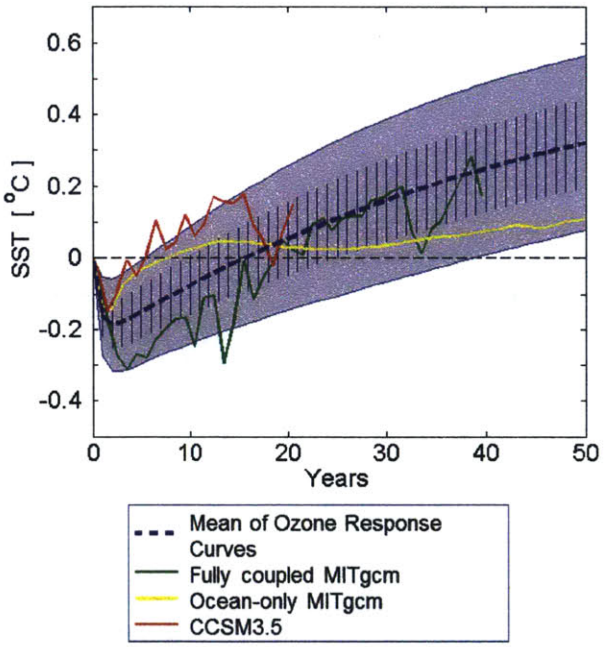

Figure 4-16: Regional CRFs to ozone from Marshall et al. [2014]. The green curve is the ensemble mean SO SST response (50S to 70S) from abrupt ozone depletion experiments with the coupled MITgcm. The red curve is the ensemble-mean evolution of the SO SST cooling forced by abrupt ozone depletion in the CCSM3.5 NCAR model. The yellow curve is the SO SST response (50S to 70S) from an abrupt SAM perturbation experiment with an ocean-only version of the MITgcm. We have considered a range of plausible idealized CRFs which span the model-based curves. The thick blue curve indicates the ensemble mean of our idealized CRFs. The shaded blue envelope indicates two standard deviations in the spread of our idealized CRFs, and the vertical hashed lines indicate one standard deviation in the spread. Layout to be modified.

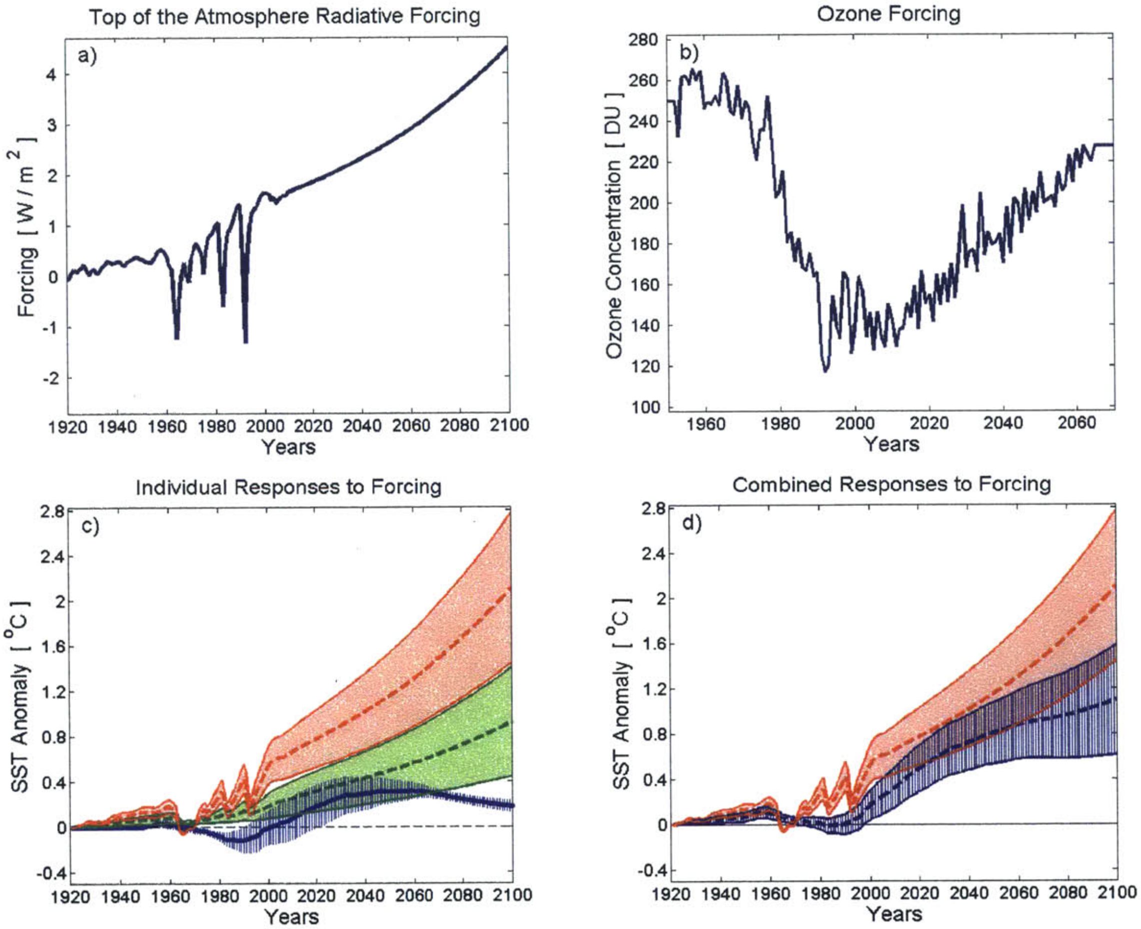

Figure 4-17: a) Historical net TOA radiative forcing [W/m^2] from Hansen et al. projected into the future assuming that the forcing increases smoothly to 4.5 [W/m^2] in 2100, consistent with the CMIP5 RCP4.5 scenario; b) Observed ozone concentration [DU] over the Antarctic region. The timeseries is extended using projections from the WACCM model; c) Individual convolutions of the GHG and the ozone-hole forcing shown in the top panels with the respective GHG and ozone-hole CRFs from Figure 4-16, yielding timeseries of the SST anomalies in the Arctic north of 50°N (red) and the Southern Ocean 50°S to 70°S (green due to GHGs and blue due to stratospheric ozone). Shaded envelopes span 1 standard deviation of the convolution ensemble; d) Combined SST responses to GHG and ozone forcing. The Arctic north of 50°N is shown in red. The Southern Ocean 50°S to 70°S is shown in blue. The SO SST evolution is the sum of the green and blue curves in c). From Marshall et al. [2014], layout to be modified.

Chapter 5

Conclusion

5.1 Summary

In this thesis we have explored the ocean's response to atmospheric forcing with a focus on two high-latitude regions: the North Atlantic and the Southern Ocean. We have estimated regional and global climate response functions (CRFs) and demonstrated their application to understanding the transient evolution of surface temperature. Analyzing the global and regional CRFs provides insights into the main oceanic processes which affect climate change.

In Chapter 2 we have examined model-based CRFs to GHG forcing obtained from CMIP5 experiments in which the atmospheric concentration of CO_2 is abruptly quadrupled relative to preindustrial control values. We show that most of the inter-model spread in these CRFs can be related to climate feedbacks. Nevertheless, we find that the ocean circulation, and the AMOC in particular, also play an important role for regulating the pace of global warming under GHG forcing. A notable fraction of the anomalous surface heat uptake takes place in the North Atlantic. This heat is then transported downward to intermediate depths and along the Deep Western Boundary Current, thereby slowing down the rate of surface temperature increase. Under GHG forcing, GCMs with a stronger or deeper AMOC store a larger fraction of the heat anomaly at depth, a physical mechanism which delays the rate of surface temperature increase. We thus find that differences in the strength and vertical extent of the time-mean AMOC constitute a notable source of intermodel spread in the CRFs among the coupled models included in CMIP5. Therefore, representing the North Atlantic and the AMOC in GCMs is important for simulating the global response to GHG forcing.

Analysis of the abrupt CO_2 quadrupling experiments reveals that the Southern Ocean is another high latitude region, which takes up a large amount of atmospheric heat under GHG forcing. We have shown that the rate of GHG-induced surface warming around Antarctica is much slower than in other parts of the World Ocean. The contrast among the regional CRFs to GHGs can be interpreted in terms of the background MOC transporting the anthropogenic heat anomaly. As discussed in Chapter 4, upwelling of unmodified deep waters to the surface of the Southern Ocean dampens the local warming rate. In comparison, the northern high latitudes warm at a more accelerated pace because the background MOC advects the heat anomaly northward similarly to a passive tracer.

However, GHGs are not the only source of historical forcing on the Southern Ocean. Over Antarctica, stratospheric ozone depletion induces an atmospheric pattern similar to the positive phase of the Southern Annular Mode (SAM) of natural variability. This pattern is characterized by a poleward intensification of the westerly winds: an increase in their magnitude and a southward shift relative to their climatological position. In turn, changes in surface wind stress modify the Southern Ocean overturning cell and give rise to an SST response.

That is why in Chapter 3 we have considered the SO CRF to a SAM atmospheric pattern. However, instead of using the output of forward perturbation experiments to deduce the relationship between SAM and SST, we have performed an analysis of the CMIP5 preindustrial control simulations under the assumption that linear response theory is a valid approximation. We estimate how the SO in each GCM is expected to respond to a hypothetical step-increase in the SAM index. We explain the SST evolution on different timescales in terms of the anomalous wind-driven circulation redistributing the background heat reservoir. Many CMIP5 models are expected to show a rapid cooling response to SAM followed by a gradual warming and a transition to a positive SST anomaly. We relate the fast surface cooling to anomalous horizontal Ekman transport advecting colder water northward. We have also shown that Ekman upwelling of warmer water in the salt-stratified SO affects the slow SST response to poleward intensification of the westerlies. We can thus propose that the nonmonotonic temporal evolution of the SO CRF to SAM in some GCMs is a consequence of these competing processes.

We furthermore relate the CMIP5 intermodel spread in the SO SST response to SAM to the models' climatological horizontal and vertical SO stratification. In Chapter 3 we show that differences in the climatological meridional SST gradients contribute to the diversity of fast responses across the ensemble. On the other hand, we find a correlation between the background potential temperature inversion in the SO and the SST response to SAM on longer timescales. We then use these relationships along with observational data for the SO horizontal and vertical thermal stratification to constrain a range of estimates for the response of the real ocean to SAM.

In Chapter 4 we have demonstrated that we can convolve our regional CRFs with timeseries of atmospheric forcing to successfully recover the SST trends in numerical simulations. We have considered the preindustrial control experiments of CMIP5 models and performed a high-minus-low composite of 30-year periods marked by extreme multidecadal SAM trends. We are able to recover the composited SST trends by using our SAM step response functions from Chapter 3. We can think of the 30-year SST trends as a superposition of multiple fast and slow responses to SAM. We furthermore put the composited SO SST trends in the context of a large-scale dipole pattern of SST anomalies induced by SAM: warming 30°S-50°S and cooling south of 50°S. We interpret this surface pattern in terms of the wind-driven circulation redistributing horizontally and vertically the background ocean heat reservoir. Moreover, we show that the composited SO SST trends are strongly negatively correlated with the contemporaneous trends in sea ice concentration around Antarctica.

We have applied a similar approach to reconstruct the regional SST anomalies in historical CMIP5 simulations. In this case we have considered a combination of different sources of forcing on the ocean. Since the Industrial Revolution, multidecadal climate change in the Northern Hemisphere has been dominated by TOA radiative forcing. On the other hand, the Southern Ocean is forced both by well-mixed GHGs and by ozone depletion – projecting onto a SAM atmospheric pattern. That is why, when reconstructing historical simulations of the SO in Chapter 4, we consider a combination of GHG and SAM forcing on the ocean convolved with the respective step response functions derived in this thesis. The step response functions to GHG forcing are based on the CMIP5 abrupt quadrupling experiments studied in Chapter 2, while the response functions to SAM are the statistical estimates computed in Chapter 3. When combining the SAM and GHG convolutions, we have to take into consideration the fact that part of the anomalous SAM trend can be attributed to historical GHG forcing. The latter complements the strong impact of stratospheric ozone depletion on the Southern Hemisphere westerly winds. Taking into account GHG forcing, SAM trends, as well as their interplay, allows us to reconstruct very well the CMIP5 historical simulations of the 1979-2014 SO SST trends.

The successful application of the CRF framework in Chapter 4 has also provided us the opportunity to identify major sources of SO warming bias in the CMIP5 historical simulations. When compared with the HadSLP2r observational dataset (*Allan and Ansell*, 2006), many GCMs underestimate the historical SAM trend (part of which can be attributed to stratospheric ozone depletion). Another subset of CMIP5 models have biases in their SO climatological temperature gradients, which affect the ocean's response to poleward intensification of the westerly winds.

In Chapter 4 we have also examined SO CRFs with respect to a stratospheric ozone depletion rather than natural variability in the SAM in order to showcase a similar two-timescale response of the SSTs around Antarctica: fast cooling, followed by gradual warming. An important aspect of this analysis is the advantage that the imposed perturbation in the models' stratosphere has a seasonal cycle analogous to the real ozone hole, which is associated with a maximum depletion in the early austral spring. We convolve our ozone and GHG CRFs with the respective forcing timeseries to simulate historical SO cooling trends. In addition, model-based estimates for the expected recovery of the ozone layer combined with scenarios of possible GHG concentration pathways allow us to make projections for the future evolution of the SO SST. Our results suggest that in the 21st century the SO cooling will transition into anomalous warming. However, similarly to the SO response to SAM, the CRFs to stratospheric ozone concentration are model-dependent. Differences in the crossover between the inherent fast cooling regime and the slow warming regime affect our range of projections for the future SO SST. It is therefore important to understand what contributes to these intermodel differences in the SO CRFs.

The results presented in this thesis suggest that both the time-mean meridional overturning circulation (MOC) and the background ocean stratification play a role in setting the inherent ocean CRFs to atmospheric forcing. A realistic representation of the high latitude ocean climatology in GCMs is therefore an important prerequisite for simulating historical climate change and for extending model projections into the future under different forcing scenarios.

5.2 Unresolved Questions and Outlook

Although this thesis has outlined several major features of the high-latitude oceans that govern the CRFs to atmospheric forcing, there are additional factors that have not been thoroughly explored here. Our analysis is based on GCMs that do not resolve ocean eddies and hence may misrepresent the bolus transport of heat. The eddy-induced circulation partially compensates the wind-driven component of the MOC and may play a very important role in modulating the regional and global SST response to GHG forcing, as well as the SO response to stratospheric ozone depletion. Thus numerical experiments with eddy-resolving models may provide more insights into the role of the residual MOC in setting the transient climate response.

In addition, both the climatological MOC and the background temperature gradients change seasonally. This important aspect of the high latitude oceans has not been fully explored in the thesis which focuses on annual-mean features. Seasonality may be particularly important for the SO response to the Antarctic ozone hole, whose impact on the surface westerlies is strongest in the austral summer, December through February (See for example *Purich et al.* (2016)). A future extension of this work should consider the response of the SO SST to changes in the DJF SAM and contrast them against the CRF to a June-July-August (JJA) SAM perturbation. A complementary study, *Holland et al.* (2016), uses the methodology developed in Chapter 3 to address a closely related problem: the seasonality of the SO sea ice response to SAM.

Another limitation of this thesis is that our analysis has focused on the North Atlantic and the Southern Ocean without discussing the interaction between these regions and the rest of the World Ocean through the MOC and via atmospheric teleconnections. Taking into account heat transport in the Tropical Atlantic, the Arctic, and the Indo-Pacific basins can provide a more comprehensive picture of the ocean's role in setting the transient climate response on a global scale.

Despite its limitations, this thesis has outlined a framework that can be used to predict how the ocean in GCMs would respond to atmospheric forcing without performing forward perturbation experiments. We have elucidated the role of the climatological mean ocean circulation and the background temperature gradients for the transient SST anomaly. Moreover, we have demonstrated that an analysis of a model's unperturbed control run may reveal how its forced response would evolve temporally. In a related study (*Holland et al.*, 2016), we use the same methodology to estimate the SO sea ice response to SAM on fast and slow timescales. Other potential applications of this framework include important problems in historical climate change such as sea level rise and carbon uptake by the ocean under anthropogenic forcing.

Bibliography

Allan R, Ansell T (2006) A new globally complete monthly historical gridded mean sea level pressure dataset (HadSLP2): 1850âĂŞ2004. J Clim 19:5816âĂŞ5842

Andrews, T., J. M. Gregory, M. J. Webb, and K. E. Taylor (2012), Forcing, Feedbacks and Climate Sensitivity in CMIP5 Coupled Atmosphere-Ocean Climate Models, *Geophys. Res. Lett.*, *39*(9), L09712, doi:10.1029/2012GL051607.

Armour, K. C., C. M. Bitz, and G. H. Roe (2013), Time-Varying Climate Sensitivity from Regional Feedbacks, *J. Clim.*, *26*(13), 4518-4534, doi:10.1175/JCLI-D-12-00544.1.

Armour K, J Marshall, A Donohoe, J Scott, E Newsom (2015) Southern Ocean warming delayed by circumpolar upwelling and equatorward transport. (submitted)

Bitz CM, Polvani LM (2012) Antarctic climate response to stratospheric ozone depletion in a fine resolution ocean climate model. Geophysical Research Letters 39. doi: 10.1029/2012GL053393

Boé, J., a. Hall, and X. Qu (2009), Deep ocean heat uptake as a major source of spread in transient climate change simulations, *Geophys. Res. Lett.*, *36*(22), L22701, doi:10.1029/2009GL040845.

Böning CW, A Dispert, M Visbeck, SR Rintoul, FU Schwarzkopf (2008) The response of the Antarctic Circumpolar Current to recent climate change. Nature Geoscience 1:864-869. doi: 10.1038/ngeo362

Ciasto LM, Thompson DWJ (2008) Observations of Large Scale Ocean Atmosphere Interaction in the Southern Hemisphere. J. Climate, 21, 1244-1259. doi: http://dx.doi.org/10.1175/2007JCLI1809.1

Rhein, M., S.R. Rintoul, S. Aoki, E. Campos, D. Chambers, R.A. Feely, S. Gulev, G.C. Johnson, S.A. Josey, A. Kostianoy, C. Mauritzen, D. Roemmich, L.D. Talley and F. Wang, 2013: Observations: Ocean. In: Climate Change 2013: The Physical Science Basis. Contribution of Working Group I to the Fifth Assessment Report of the Intergovernmental Panel on Climate Change [Stocker, T.F., D. Qin, G.-K. Plattner, M. Tignor, S.K. Allen, J. Boschung, A. Nauels, Y. Xia, V. Bex and P.M. Midgley (eds.)]. Cambridge University Press, Cambridge, United Kingdom and New York, NY, USA, pp. 260-264.

Compo, G.P., J.S. Whitaker, and P.D. Sardeshmukh (2006) Feasibility of a 100 year reanalysis using only surface pressure data. Bull. Amer. Met. Soc., 87, 175-190, doi: http://dx.doi.org/10.1175/BAMS-87-2-175

Cunningham, S. A., Kanzow, T., Rayner, D., Baringer, M. O., Johns, W. E., Marotzke, J., Longworth, H. R., Grand, E. M., Hirschi, J. J. M., Beal, L. M., Meinen, C. S., and Bryden, H. L. (2007), Temporal variability for the Atlantic Meridional Overturning Circulation at 26.5^o N, *Science, 317*, 935-937, doi:10.1126/science.1141304.

de Lavergne C, JB Palter, ED Galbraith, R Bernardello, I Marinov (2014) Cessation of deep convection in the open Southern Ocean under anthropogenic climate change. Nature Climate Change 4, 278-282, doi:10.1038/nclimate2132

DeAngelis, AM, X Qu, MD Zelinka, and A Hall (2015) An observational radiative constraint on hydrologic cycle intensification. Nature, 528, 249âĂŞ253, doi:10.1038/nature15770

Dee DP, Uppala SM, Simmons AJ, et al (2011) The ERA-Interim reanalysis: configuration and performance of the data assimilation system. Quarterly Journal of the Royal Meteorological Society 137:553-597. doi: 10.1002/qj.828

Dommenget, D. (2009), The Ocean's role in continental climate variability and change, *J. Climate*, *22*, 4939-4952, doi:10.1175/2009JCLI2778.1.

Fan, T., C. Deser, and D. P. Schneider (2014), Recent Antarctic sea ice trends in the context of Southern Ocean surface climate variations since 1950, Geophys. Res. Lett., 41, 2419-2426, doi:10.1002/2014GL059239.

Ferreira D, J Marshall, CM Bitz, S Solomon, and A Plumb (2015) Antarctic Ocean and Sea Ice Response to Ozone Depletion: A Two-Time-Scale Problem. Journal of Climate 28:1206-1226. doi: 10.1175/JCLI-D-14-00313.1

Fyfe JC, Saenko OA, Zickfeld K, et al (2007) The Role of Poleward-Intensifying Winds on Southern Ocean Warming. Journal of Climate 20:5391-5400. doi: 10.1175/2007JCLI1764.1

Ganachaud, A. (2003), Large-scale mass transports, water mass formation, and diffusivities estimated from World Ocean Circulation Experiment (WOCE) hydrographic data, *J. Geophys. Res., 108*(C7), 3213, doi:10.1029/2002JC001565.

Geoffroy, O., D. Saint-Martin, and A. Ribes (2012), Quantifying the sources of spread in climate change experiments, *Geophys. Res. Lett.*, *39*(24), doi:10.1029/2012GL054172.

Geoffroy, O., D. Saint-Martin, D. J. L. Olivié, A. Voldoire, G. Bellon, and S. Tytéca (2013a), Transient Climate Response in a Two-Layer Energy-Balance Model. Part I: Analytical Solution and Parameter Calibration Using CMIP5 GCM Experiments, *J. Clim.*, *26*(6), 1841-1857, doi:10.1175/JCLI-D-12-00195.1.

Geoffroy, O., D. Saint-Martin, G. Bellon, A. Voldoire, D. J. L. Olivié, and S. Tytéca (2013b), Transient Climate Response in a Two-Layer Energy-Balance Model. Part II: Representation of the Efficacy of Deep-Ocean Heat Uptake and Validation for CMIP5 GCMs, *J. Clim.*, *26*(6), 1859-1876, doi:10.1175/JCLI-D-12-00196.1.

Gillett NP, Thompson DWJ (2003) Simulation of recent southern hemisphere climate change. Science, *302*, pp. 273-2755. doi: 10.1126/science.1087440

Good SA, Martin MJ, Rayner NA (2013) EN4: Quality controlled ocean temperature and salinity profiles and monthly objective analyses with uncertainty estimates. Journal of Geophysical Research: Oceans 118:6704-6716. doi: 10.1002/2013JC009067

Gregory, J., and M. Webb (2008), Tropospheric Adjustment Induces a Cloud Component in CO 2 Forcing, *J. Clim.*, *21*(1), 58-71, doi:10.1175/2007JCLI1834.1.

Gregory, J. M. (2000), Vertical heat transports in the ocean and their effect on time-dependent climate change, *Clim. Dyn.*, 16(7), 501-515, doi:10.1007/s003820000059.

Gregory, J. M., K. W. Dixon, R. J. Stouffer, A. J. Weaver, E. Driesschaert, M. Eby, T. Fichefet, H. Hasumi, A. Hu, J. H. Jungclaus, I. V. Kamenkovich, A. Levermann, M. Montoya, S. Murakami, S. Nawrath, A. Oka, A. P. Sokolov, R. B. Thorpe. (2005), A model intercomparison of changes in the Atlantic thermohaline circulation in response to increasing atmospheric CO2 concentration, *Geophys. Res. Lett.*,*32*, L12703, doi:10.1029/2005GL023209.

Hall A, Visbeck M (2002) Synchronous variability in the Southern Hemisphere atmosphere, sea ice, and ocean resulting from the Annular Mode*. Journal of Climate, 15, 3043-3057. doi: http://dx.doi.org/10.1175/1520-0442(2002)015<3043:SVITSH>2.0.CO;2

Hansen, J., G. Russell, A. Lacis, I. Fung, D Rind, and P. Stone (1985), Climate response times: Dependence on climate sensitivity and ocean mixing. *Science*, *229*, 857-859, doi:10.1126/science.229.4716.857.

Hansen, J., M. Sato, R. Ruedy, L. Nazarenko, A. Lacis, G.A. Schmidt, G. Russell, I. Aleinov, M. Bauer, S. Bauer, N. Bell, B. Cairns, V. Canuto, M. Chandler, Y. Cheng, A. Del Genio, G. Faluvegi, E. Fleming, A. Friend, T. Hall, C. Jackman, M. Kelley, N.Y. Kiang, D. Koch, J. Lean, J. Lerner, K. Lo, S. Menon, R.L. Miller, P. Minnis, T. Novakov, V. Oinas, J.P. Perlwitz, J. Perlwitz, D. Rind, A. Romanou, D. Shindell, P. Stone, S. Sun, N. Tausnev, D. Thresher, B. Wielicki, T. Wong, M. Yao, and S. Zhang (2005) Efficacy of climate forcings. J. Geophys. Res., 110, D18104, doi:10.1029/2005JD005776.

Hansen, J., Mki. Sato, P. Kharecha, and K. von Schuckmann (2011), Earth's energy imbalance and implications. *Atmos. Chem. Phys.*, *11*, 13421-13449, doi:10.5194/acp-11-13421-2011.

Hasselmann, K., Sausen, R., Maier-Reimer, E. and Voss, R. (1993), On the cold start problem in transient simulations with coupled atmosphere-ocean models. Climate Dynamics, 9(2), 53-61. doi: 10.1007/BF00210008

Held, I. M., M. Winton, K. Takahashi, T. Delworth, F. Zeng, and G. K. Vallis (2010), Probing the Fast and Slow Components of Global Warming by Returning Abruptly to Preindustrial Forcing, *J. Clim.*, *23*(9), 2418-2427, doi:10.1175/2009JCLI3466.1.

Hoffert, M.I., A.J. Callegary, C-T. Hsieh (1980), The role of deep sea heat storage in the secular response to climatic forcing, *J. Geophys. Res.: Atmos.*, *85*(C11), 6667-6679, doi:10.1029/JC085iC11p06667.

Holland M, L Landrum, Y Kostov, and J Marshall (2016) Sensitivity of Antarctic sea ice to SAM-associated wind anomalies in coupled climate models (in prep.).

Hutchinson DK, England MH, Santoso A, Hogg AM (2013) Interhemispheric asymmetry in transient global warming: The role of Drake Passage. Geophysical Research Letters 40:1587-1593. doi: 10.1002/grl.50341

Hutchinson, DK, MH England, AMcC Hogg and K Snow (2015) Interhemispheric Asymmetry of Warming in an Eddy Permitting Coupled Sector Model, J. Climate, 28, 7385-7406. doi: 10.1175/JCLI-D-15-0014.1

Knutti, R, D Masson, and A Gettelman (2013), Climate model genealogy: Generation CMIP5 and how we got there, Geophys. Res. Lett., 40, 1194-1199, doi:10.1002/grl.50256.

Kostov, Y, KC Armour, and J Marshall (2014), Impact of the Atlantic meridional overturning circulation on ocean heat storage and transient climate change, Geophys. Res. Lett., 41, 2108âĂŞ2116, doi:10.1002/2013GL058998.

Kostov, Y, J Marshall, U Hausmann, KC Armour, D Ferreira, and M Holland (2016), Fast and slow responses of Southern Ocean sea surface temperature to SAM in coupled climate models, Climate Dynamics (under review).

Kostov Y, et al. (2016) Southern Ocean cooling in a warming world: reassessing the role of westerly winds. (in prep.)

Kostov Y, et al. (2016) Understanding the Southern Ocean warming bias in historical climate simulations. (in prep.)

Kuhlbrodt, T., and J. M. Gregory (2012), Ocean heat uptake and its consequences for the magnitude of sea level rise and climate change, *Geophys. Res. Lett.*, *39*, L18608, doi:10.1029/2012GL052952.

Li C., J-S von Storch and J. Marotzke (2012), Deep-ocean heat uptake and equilibrium climate response. *Climate Dynamics*, DOI 10.1007/s00382-012-1350-z.

Lumpkin, R. and Speer, K. (2003), Large-scale vertical and horizontal circulation in the North Atlantic Ocean, *J. Phys. Oceanogr.*, *33*, 1902âĂŞ1920.

Marshall, J. and K. Speer (2012) Closure of the meridional overturning circulation through Southern Ocean upwelling. Nature Geoscience 5, 171âĂŞ180. doi:10.1038/ngeo1391

Marshall J, KC Armour, JR Scott, Y Kostov, U Hausmann, D Ferreira, TG Shepherd, CM Bitz (2014) The ocean's role in polar climate change: asymmetric Arctic and Antarctic responses to greenhouse gas and ozone forcing. Phil. Trans. R. Soc. A 2014 372 20130040; DOI: 10.1098/rsta.2013.0040

Marshall J, JR Scott, KC Armour, J-M Campin, M Kelley, and A Romanou (2015) The ocean's role in the transient response of climate to abrupt greenhouse gas forcing. Climate Dynamics, Vol. 44, Issue 7, pp 2287-2299. doi: 10.1007/s00382-014-2308-0.

Medhaug I. and T. Furevik, North Atlantic 20th century multidecadal variability in coupled climate models: sea surface temperature and ocean overturning circulation. *Ocean Science*, *7*, 389-401, doi:10.5194/os-7-389-2011.

Meijers AJS (2014) The Southern Ocean in the Coupled Model Intercomparison Project phase 5. Phil.Trans.R. Soc. A372: 20130296. doi: http://dx.doi.org/10.1098/rsta.2013.0296

Oke P, England M (2004) Oceanic response to changes in the latitude of the Southern Hemisphere subpolar westerly winds. Journal of Climate, 17, 1040-1054. doi: http://dx.doi.org/10.1175/1520-0442(2004)017<1040:ORTCIT>2.0.CO;2

Pagani M, Z Liu, J LaRiviere, and AC Ravelo (2010) High Earth-system climate sensitivity determined from Pliocene carbon dioxide concentrations. Nature Geoscience, 3, 27-30 DOI: 10.1038/NGEO724.

Previdi, M., Liepert, B. G., Peteet, D., Hansen, J., Beerling, D. J., Broccoli, A. J., Frolking, S., Galloway, J. N., Heimann, M., Le QuÃľrÃľ, C., Levitus, S. and Ramaswamy, V. (2013), Climate sensitivity in the Anthropocene. Q.J.R. Meteorol. Soc., 139: 1121âĂŞ1131. doi:10.1002/qj.2165

Purich A, W Caj, MH England, and T Cowan (2016) Evidence for link between modelled trends in Antarctic sea ice and underestimated westerly wind changes. Nature Communications, in press.

Raper, S.C.B., and U. Cubasch (1996), Emulation of the results from a coupled general circulation model using a simple climate model. *Geophys. Res. Lett.*, *23*, 1107-1110, doi:10.1029/96GL01065.

Raper, S., J. Gregory, and R. Stouffer (2002), The role of climate sensitivity and ocean heat uptake on GCM transient temperature response, *J. Clim.*, *15*, 124-130.

Reynolds RW, NA. Rayner, TM Smith, DC Stokes, and W Wang (2002) An Improved In Situ and Satellite SST Analysis for Climate. J. Climate, 15, 1609-1625. doi: http://dx.doi.org/10.1175/1520-0442(2002)015<1609:AIISAS>2.0.CO;2

Rose, B.E.J., K.C. Armour, D.S. Battisti, N. Feldl and D.D.B Koll (2014), The dependence of transient climate sensitivity and radiative feedbacks on the spatial pattern of ocean heat uptake, *Geophys. Res. Lett.*, *41*, doi:10.1002/2013GL058955.

Rugenstein, M. A. A., M. Winton, R. J. Stouffer, S. M. Griffies, and R. Hallberg (2013), Northern High-Latitude Heat Budget Decomposition and Transient Warming, *J. Clim.*, *26*, 609-621, doi:10.1175/JCLI-D-11-00695.1.

Russell JL, KW Dixon, A Gnanadesikan, RJ Stouffer, and JR Toggweiler (2006) The Southern Hemisphere Westerlies in a Warming World: Propping Open the Door to the Deep Ocean. J. Climate, 19, 6382-6390. doi: http://dx.doi.org/10.1175/JCLI3984.1

Salleé, J-B, E Shuckburgh, N Bruneau, AJS Meijers, TJ Bracegirdle, and Z Wang (2013), Assessment of Southern Ocean mixed layer depths in CMIP5 models: Historical bias and forcing response, J. Geophys. Res. Oceans, 118, 1845-1862, doi:10.1002/jgrc.20157

Sen Gupta A, England M (2006) Coupled Ocean-Atmosphere-Ice Response to Variations in the Southern Annular Mode. J. Climate, 19, 4457-4486. doi: http://dx.doi.org/10.1175/JCLI3843.1

Sen Gupta A, England MH (2007) Coupled Ocean-Atmosphere Feedback in the Southern Annular Mode. Journal of Climate 20:3677-3692. doi: 10.1175/JCLI4200.1

Seviour, WJM., Waugh, DW and Gnanadesikan, A (2016) Challenges in determining the transient response of the Southern Ocean to ozone depletion (in prep.)

Sigmond M, Fyfe JC (2014) The Antarctic Sea Ice Response to the Ozone Hole in Climate Models. Journal of Climate, 27:1336-1342. doi: 10.1175/JCLI-D-13-00590.1

Sigmond M, Reader MC, Fyfe JC, Gillett NP (2011) Drivers of past and future Southern Ocean change: Stratospheric ozone versus greenhouse gas impacts. Geophysical Research Letters, 38. doi: 10.1029/2011GL047120

Solomon A, LM Polvani, KL Smith, and RP Abernathey (2015), The impact of ozone depleting substances on the circulation, temperature, and salinity of the Southern Ocean: An attribution study with CESM1(WACCM), Geophys. Res. Lett., 42, doi:10.1002/2015GL064744.

Stouffer, Ronald J. (2004) Time Scales of Climate Response. *J. Climate*, *17*, 209-217, doi:http://dx.doi.org/10.1175/1520-0442(2004)017<0209:TSOCR>2.0.CO;2.

Taylor, K. E., R. J. Stouffer, and G. A. Meehl (2012), An oveview of CMIP5 and the experiment design, *Bull. Am. Meteorol. Soc.*, *93*, 485-498, doi:10.1175/BAMS-D-11-00094.1.

Thomas J.L., D. W. Waugh, A Gnanadesikan, 2015 Southern Hemisphere extra-tropical circulation: Recent trends and natural variability. Geophys. Res. Lett., (sumbitted).

Thompson D, Solomon S (2002) Interpretation of recent Southern Hemisphere climate change. Science 296 (5569), 895-899. [DOI:10.1126/science.1069270]

Thompson DWJ, Solomon S, Kushner PJ, et al (2011) Signatures of the Antarctic ozone hole in Southern Hemisphere surface climate change. Nature Geoscience 4:741-749. doi: 10.1038/ngeo1296

Wang G, Cai W, Purich A (2014) Trends in Southern Hemisphere wind-driven circulation in CMIP5 models over the 21st century: Ozone recovery versus greenhouse forcing. J. Geophys. Res. Oceans, 119, 2974-2986, doi:10.1002/2013JC009589.

Waugh DW, F Primeau, T DeVries, and M Holzer. Recent Changes in the Ventilation of the Southern Oceans. Science, 339 (6119), 568-570. [DOI:10.1126/science.1225411]

Waugh DW (2014) Changes in the ventilation of the southern oceans. Phil. Trans. R. Soc. A 2014 372 20130269; DOI: 10.1098/rsta.2013.0269.

Wigley, T. M. L. and S. C. B. Raper, (1987), Thermal expansion of sea water associated with global warming. *Nature*, *330*, 127-131, doi:10.1038/330127a0.

Winton, M., K. Takahashi, and I. M. Held (2010), Importance of Ocean Heat Uptake Efficacy to Transient Climate Change, *J. Clim.*, *23*(9), 2333-2344, doi:10.1175/2009JCLI3139.1.

Winton, M., S. M. Griffies, B. L. Samuels, J. L. Sarmiento, and T. L. Frölicher (2013), Connecting Changing Ocean Circulation with Changing Climate, *J. Clim.*, *26*(7), 2268-2278, doi:10.1175/JCLI-D-12-00296.1.

Winton, M, WG Anderson, TL Delworth, SM Griffies, WJ Hurlin, and A Rosati (2014), Has coarse ocean resolution biased simulations of transient climate sensitivity?, Geophys. Res. Lett., 41, 8522-8529, doi:10.1002/2014GL061523

Xie, P., and G. K. Vallis (2011), The passive and active nature of ocean heat uptake in idealized climate change experiments, *Clim. Dyn.*, *38*, 1-18-18, doi:10.1007/s00382-011-1063-8.